Astrophysikalisches Institut Potsdam
Arbeitsgruppe Solare Radiophysik

Electron acceleration at localized wave structures in the solar corona

Dissertation
zur Erlangung des akademischen Grades
'doctor rerum naturalium'
(Dr. rer. nat.)
in der Wissenschaftsdisziplin 'Astrophysik'

eingereicht an der
Mathematisch–Naturwissenschaftlichen Fakultät
der Universität Potsdam

von
Rositsa Stoycheva Miteva

Potsdam, im März 2007

Elektronisch veröffentlicht auf dem
Publikationsserver der Universität Potsdam:
http://opus.kobv.de/ubp/volltexte/2007/1477/
urn:nbn:de:kobv:517-opus-14775
[http://nbn-resolving.de/urn:nbn:de:kobv:517-opus-14775]

Thesis advisor
Prof. Dr. Gottfried Mann

Author
Rositsa Stoycheva Miteva

Electron acceleration at localized wave structures in the solar corona

Abstract

The Sun is an active star that manifests its activity not only in the appearance of the well-known sunspots but also in flares. During a flare, a huge amount of the stored magnetic energy is suddenly released and transfered into: a local heating of the corona, mass motions (e.g., jets and coronal mass ejections), an enhanced emission of electromagnetic radiation (from the radio up to the γ-ray range), and a generation of energetic particles (e.g., electrons, protons, and heavy ions). A substantial part of the flare released energy is carried by the energetic electrons, which are the source of the nonthermal radio and X-ray radiation. They can be detected by different means: with radio (e.g., from the ground-based radio observatories of the Astrophysical Institute Potsdam, Germany and the Nançay radioheliograph, France, respectively), with X-ray (e.g., RHESSI satellite), and with in-situ (e.g., WIND spacecraft) measurements. One of the most important and still open questions in solar physics is how the electrons are accelerated up to high energies within a short time, as it is observed during flares. Understanding the basic physical mechanisms that take part in the acceleration process of electrons in the solar corona is also of general astrophysical interest (e.g., for flares at other stars, relativistic jets, active galactic nuclei).

From radio observations it is known that electrons can be accelerated up to velocities of the order of $0.3\,c$ for time scales of around 10 ms. This gives an estimate for the acceleration length of several hundred kilometers. Compared to the solar radius, the acceleration site is extremely small in spatial extent, and hence the electron acceleration can be regarded as a local process.

The aim of the dissertation is to search for localized wave structures that are able efficiently to accelerate electrons. Motivated by radio and X-ray observations, it is theoretically investigated how such structures can contribute to the processes leading to the effective electron acceleration in the solar corona.

There are two main mechanisms able to accelerate electrons: due to a process of magnetic reconnection and by shocks. These aspects are investigated with respect to the localized wave structures here. Accepting the general picture of magnetic reconnection as the basic process of the flare, it is focused on the ejection of plasma after the rearranging of the newly reconnected magnetic field lines. Such plasma jets, as extensively studied with the *Yohkoh* satellite mission, were spatially and temporally associated with the so-called type III metric radio bursts, regarded as the radio signatures of a beam of energetic electrons propagating through the solar corona. In order to study the link between the plasma jets and the generation of energetic electrons, the jet–plasma interaction (i.e., jet with the background coronal plasma) is investigated here, namely, how in this configuration an (ion-acoustic) instability could arise and provide an enhanced level of electrostatic fluctuations, at which electrons can be accelerated (and/or heated), as observed in the type III metric radio bursts in the solar radio radiation.

On the other hand, shocks are also able to accelerate electrons, as observed by so-called type II metric radio bursts (the radio signature of a shock wave in the solar corona). In space plasmas, shocks are best observed at Earth's bow shock, traveling interplanetary shocks and shocks related with co-rotating interaction regions. These observations show, that energetic electrons are associated with shocks attached by whistler waves. Here, we study the electron–whistler–shock interaction under coronal conditions as a possible configuration for the successful acceleration of electrons in the solar corona. Because there are no direct observations of shocks in the corona, it is assumed that the basic plasma processes responsible for the electron acceleration at all shocks should be the same.

In both approaches, the electron is regarded as a test particle moving in the electrostatic (ion-acoustic) wave field, in the case of a jet–plasma interaction, and/or in the electric and magnetic fields of the shock and the attached whistlers, in the case of an electron–whistler–shock interaction. Both provide us two new theoretical models for electron acceleration in the solar corona and are well in agreement with the radio and X-ray observations.

The dissertation is structured as follows:

A general overview on the Sun, the flare process and the flare-produced energetic electrons in the solar corona is given in **Chapter 1**. Thereafter, an overall description of the plasma waves is briefly presented in **Chapter 2**.

In **Chapter 3** a nonlinear analysis of the plasma waves is performed for a pure electron–proton plasma, in order to obtain fully nonlinear solutions of the employed two-fluid plasma equations. These nonlinear solutions are a complementary study for the considered later on (in Chapter 5) problem of electron movement in the attached whistler packets at a coronal shock wave.

Chapter 4 explores the new approach for electron acceleration due to an ejection of plasma jets when a magnetic reconnection takes place in the corona. The mechanism considers the process of the jet–coronal plasma interaction that is treated in a kinetic manner (via the Vlasov–Maxwell equations). Under special conditions this jet–plasma interaction gives rise to an (ion-acoustic) instability providing an enhanced level of electrostatic fluctuations at which electrons are accelerated and/or heated.

Chapter 5 presents the study of an electron interaction with attached whistler waves at shocks as a further successful mechanism for electron acceleration in the solar corona. The presented model in the dissertation has the advantage to account for a more realistic shock configuration in the solar corona, in contrast to the already existing theories for particle acceleration at coronal shocks.

A summary of all obtained results of the dissertation is presented in **Chapter 6**.

Contents

Chapter 1

Introduction

1.1 Structure of the Sun

Our Sun is an ordinary main-sequence star of absolute stellar magnitude 4.8. It is however the only star in our proximity that we are able to observe in such great details. In the last decades, a fleet of satellite missions (e.g., *Ulysses*, *Yohkoh*, SOHO, TRACE, RHESSI, *Hinode* (SOLAR-B), STEREO, see for example [19, 11]) essentially did and will continue to enhance our knowledge about the Sun (an overall view of the Sun is shown on Fig. 1.1). The quality enhancement of the satellite data is one necessary condition for the gradual improvement of our physical understanding: on the Sun (in particular), on the other stars (in general), and on the solar system, as an unique real-plasma laboratory (mostly impossible to reproduce in terrestrial conditions). Naturally, the discoveries on the physical properties of the Sun can be applied to other stars, that is usually called **solar–stellar connection**.

Overall physical properties of the Sun [83]:

Spectral type: G2 V

Age: 4.5×10^9 yr

Mass: $M_\odot = 1.99 \times 10^{33}$ g

Radius: $R_\odot = 6.96 \times 10^{10}$ cm (696 000 km)

Mean mass density: $\rho_\odot = 1.4\,\mathrm{g\,cm^{-3}}$

Surface gravity: $g_\odot = 2.74 \times 10^4\,\mathrm{cm\,s^{-2}}$

Luminosity (emitted radiation per second):
$L_\odot = 3.86 \times 10^{33}\,\mathrm{erg\,s^{-1}}$ (3.86×10^{26} W)

Mass loss rate: $10^{12}\,\mathrm{g\,s^{-1}}$

Equatorial rotation period: 26 days

Effective temperature: $T_{\mathrm{eff}} = 5785$ K

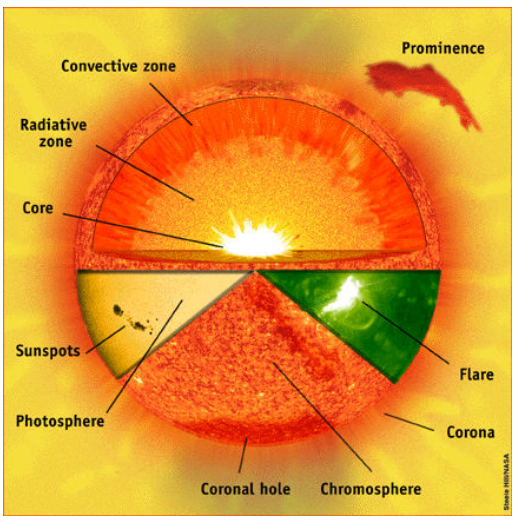

Figure 1.1: Cartoon on the solar interior, atmosphere and phenomena (NASA).

However, the Sun is mostly important for us because of its constant supply of light and heat that sustain life on Earth. It is as well the main driver for the geomagnetic and climate disturbances on our planet. Such solar–terrestrial connection is known as **space weather**.

Because the mean distance from the Sun to Earth is about 150×10^6 km (or 1 AU), an angle of 1 arcsecond corresponds to a length scale of 726 km on the solar surface. Presently, the achieved spatial resolution from ground-based optical telescopes goes down to resolving structures of about 100 km, as for example done with the Swedish Solar Telescope (SST)[1].

Though a detailed description of the Sun is not intended here, a general overview of the solar interior and atmosphere will follow, for the completeness of the introductory part.

Solar interior

The solar interior (as schematically given on Fig. 1.1) is visually hidden from us, i.e., there is no radiation coming directly from this inner part of the Sun that could give us a hint about the physical conditions inside the Sun (the neutrinos are the only exception). It was up to the theoretical models to determine how the physical quantities (like temperature, density, pressure, rotation, sound speed, and chemical composition) vary with depth. In the 1970s, the prediction of such solar models could be actually checked with observation, namely with the results given from the helioseismology. Helioseismology is a study of the interior of the Sun by analyzing magnetosound and magnetogravity waves that propagate through the solar interior and manifest themselves as oscillations at the solar surface. Hence due to analysis of these pressure (or p-) modes, one can actually 'see' in the solar inner parts (by analogy with the earthquakes used for probing the terrestrial interior).

The Sun, as any other star, is a plasma sphere held together by the perfect balance of its gas pressure and its gravitational attraction. The **Standard Model** of the Sun (i.e., spherically symmetric, negligible effects of: internal rotation, internal magnetic fields, mass loss, and tidal forces) is based on the simplest possible assumptions, in contrast to the more recent models, taking into account the latest available physical inputs (e.g., opacity, hydrogen–helium abundance, neutrino deficit), see for example the model by [15]. Usually all models give chemical composition dominated by hydrogen ($X = 0.71$) and helium ($Y = 0.27$), with small fraction of heavy elements ($Z = 0.02$) [7].

The solar interior is schematically divided into three zones: core, radiative and convective zone (see Fig. 1.1). The solar models give a central temperature 15×10^6 K and mass density[2] $150\,\mathrm{g\,cm^{-3}}$. The core temperature and density are both high enough to initiate and sustain thermonuclear reactions. **The solar core** extends to about a quarter of the visible solar radius but contains half of the total solar mass. There, the hydrogen nuclei are fused into helium (most efficiently by the proton–proton cycle) and thus generate more than 99% of the whole energy needed for sustaining the solar luminosity. The thermonuclear burning

[1] The Swedish 1-meter Solar Telescope (SST) is operated on the island of La Palma by the Institute for Solar Physics of the Royal Swedish Academy of Sciences in the Spanish Observatorio del Roque de los Muchachos of the Instituto de Astrofsica de Canarias. http://www.solarphysics.kva.se/

[2] For the solar interior the mass density will be used, and its value is given here in cgs-units, from http://solarscience.msfc.nasa.gov/interior.shtml, but note that slight variations are possible in other references.

is almost completely shut off beyond the outer edge of the core (at a distance of about 175 000 km from the center of the Sun). At that point the temperature is only half its central value, i.e., 5.9–7.5 $\times 10^6$ K and the density drops to about 20 g cm^{-3}, which is regarded as the 'lower border' of the next zone.

The core is wrapped with the so-called **radiative zone** that extents up to nearly 0.7 of the solar radius and reaches temperature of 1.8–2 $\times 10^6$ K, whereas the density drops down to 0.2 g cm^{-3} at the top of the zone. Throughout this zone, the photons are transported by radiative diffusion. The generated photons in the core need some 10 million years to finally leave the solar interior (compare to about 2 seconds in the case of a free path), being constantly scattered, absorbed and re-emitted on their way. The effect of these collisions is that the initial wavelength of the photon generated in the core (in the γ-ray range) is increased to that of a visible light.

In the upper one-third of the visible solar radius, the so-called **convective zone** is established, since the temperature gradient becomes too steep for the plasma to remain in static equilibrium (the measured temperature and density on the surface are 5785 K and 0.2 $\times 10^{-6}$g cm^{-3}, correspondingly). As a result, this region is convectively unstable and the plasma is brought in up- and downward motions due to buoyancy forces. Restless convective sells of different sizes arise, and so the energy is transported dominantly by such convective motions.

A different kind of motions of large regions of the Sun are the vertical oscillations with speed of a thousand km per hour and period of about 5 minutes. In the early 1970s these 5-minute oscillations were correctly interpreted as surface vibrations arising from standing sound waves in the convection zone. Sound waves of narrow frequency range are trapped in the convection zone and they interfere with each other forming standing waves. Analyzing the complicated interference pattern that arise on the surface from all oscillating modes, it is possible to determine the depths at which the modes get refracted (usually at place where a sharp gradient in density is present, i.e., at the borders of two different zones of the solar interior). After the investigation of such solar oscillation data from MDI[3] instrument aboard SOHO[4] spacecraft, an important discovery was made, namely the distinct 'bump' in the sound speed profile at the base of the convection zone. Due to this sudden increase in the sound speed and hence a corresponding increase in temperature and density, a 'shear' region near 0.67 $R_\odot$ develops, which is known as '**tachocline**' [11]. This interface layer between the radiative and the convection zone, has an important consequence related to the dynamo theory for generation of the magnetic field in the Sun.

Solar atmosphere

The solar atmosphere can be roughly divided into three layers with no rigid boundaries between each of them: **photosphere**, **chromosphere**, (transition region) and **solar corona** (that extends outwards as the solar wind). Usually, they are considered as spherical shells, instead of regarding them as domains with different physical characteristics [10] (Fig. 1.1).

[3]Michelson Doppler Imager (MDI). http://soi.stanford.edu/

[4]SOlar and Heliospheric Observatory (SOHO) is a project of international collaboration between ESA and NASA to study the Sun from its deep core to the outer corona and the solar wind. http://sohowww.nascom.nasa.gov/

Figure 1.2: White light image of the Sun with sunspot group, from the finder telescope at the SST, credit Royal Swedish Academy of Sciences.

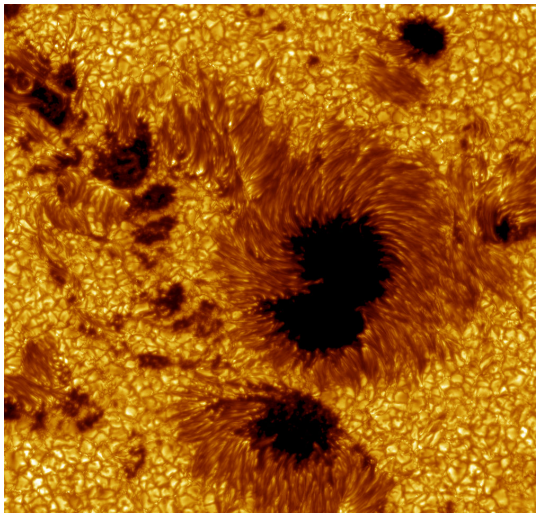

Figure 1.3: Granulation and group of sunspots on 15–Jul–2002 from the SST, credit Royal Swedish Academy of Sciences (zoomed area from Fig. 1.2).

In each of these layers, the main physical plasma properties: number density[5], temperature, pressure, and magnetic field strength, vary with the radial distance (due to the gravitationally stratification of the medium) and additionally different transient features/structures are present or become prominent.

Photosphere

The lowest atmospheric layer, called photosphere, is the 'optical surface' of the Sun because there the solar plasma becomes transparent to optical light (see Fig. 1.2). The emitted radiation is primarily in the form of thermal blackbody radiation. It has an effective temperature of 5785 K and overall density of $10^{17}\,\mathrm{cm}^{-3}$. It is only some hundred kilometers wide and the gas is only partially ionized (mostly neutral) with electron to neutral density ratio of about 10^{-4} [83]. Convective motions, as present just below the photosphere, are observed over the whole surface as a boiling structure, called **granulation**, see Fig. 1.3. The granules are usually very irregular, but in general with polygonal shapes and are surrounded with darker intergranular lanes. Each granulation cell ranges in width from 210 km up to 2300 km (0.3"–3") with mean diameter of 970 km (1.3") and characteristic lifetime of 10–16 min (observed with SST). The up-/downward motion as measured by Doppler shifts of Fraunhofer lines gives vertical rms (root mean squared) velocities of 1 $\mathrm{km\,s}^{-1}$ and horizontal rms velocities of 2 $\mathrm{km\,s}^{-1}$. In summary, in white light the granulation can be described as irregular mosaic of bright patterns (that are in fact rising hot material), separated by narrow dark lanes (cooler descending material, respectively). Another kind of large-scale horizontal motion on the Sun is the so-called **supergranulation** [47], with

[5]Here, for describing the density of the plasma in the solar atmosphere, the number density will be used.

velocities of about 0.3–0.5 $\mathrm{km\,s^{-1}}$. The supergranulation also manifests itself in the photosphere, although it is more difficult to distinguish than the granulation. Supergranulation cells range from 25000 km to 85000 km (mean size of about 35000 km across) and have lifetime of about 1–2 days. Another intermediate velocity pattern was also observed, with scale size of 5000–10000 km (7"–14") across, lifetime of around 2 hours and vertical rms speed of 0.06 $\mathrm{km\,s^{-1}}$. It was called **mesogranulation** [76] and the mesogranules could be interpreted as groups of individual granules displaying a common velocity pattern.

Chromosphere

The chromosphere is the 'coloured' sphere as revealed just before and after a total solar eclipse. Another definition, [83] for example, describes it as the layer between the temperature minimum (4200 K) and the level of $\approx 10^4$ K, with a width of about 2000 km. This layer is more transparent in comparison with the underlying photosphere, with a density of the order of $10^{11}\,\mathrm{cm^{-3}}$. The gas in the chromosphere is almost transparent to visible (continuum) radiation but is optically thick in certain atomic transition lines. For example, very fine observations in the strong chromospheric Hα and CaII H&K lines display a variety of interesting phenomena, such as: spicules (small jets seen in projection as 'fur/hair'-like structure, extending up to 6500–9500 km out of the limb); bright and dark mottles (that are in fact spicules projected on the bright background); chromospheric network structure (bright network pattern with cells of 30 000–35 000 km); plages (bright patches), filaments (elongated dark structures that are in fact protuberances seen on the disc); fibrils (fine dark lines), etc. This very complex morphology confirms the non-uniform and the non-homogeneous structure of the chromosphere.

Transition region

This is an intermediate region between the relatively cool chromosphere (10^4 K) and the hot corona (10^6 K) and it is more appropriate to regard it as a temperature regime than a concentric geometric layer of few hundred kilometers [10]. In this region there is a sharp spatial discontinuity in temperature and density, as shown on Fig. 1.4, i.e., the temperature rises 100 times, while the density drops at least 1000 times. The transition region (TR) is best visible in certain strong EUV resonance lines of heavy ions of FeXV, MgIX, NeVII, OVI/IV. Observations made at HeII line (304 Å) from SOHO arise at 6×10^4 K, which corresponds to the lower part of the TR, while images taken in Fe IX line (171 Å) formed at 1 MK refer to the upper TR. Observations made in different lines allow to actually see various layers from the TR (and the solar atmosphere in general), thus different structures become more prominent and could be seen in greater details.

Corona

The **corona** is the uppermost region of the solar atmosphere and it extends gradually outwards into the interplanetary medium as the solar wind. This is the hottest (surprisingly reaching values of $1\text{–}2\times10^6$ K) and the most tenuous layer (with density fall from $10^9\,\mathrm{cm^{-3}}$ to $10^6\,\mathrm{cm^{-3}}$) of the atmosphere. It can be observed in visible (white) light only during the total phase of a solar eclipse from Earth (as for example on Fig. 1.5) or with coronographs (artificially blocking the bright photosphere) from satellites (e.g., with LASCO[6] abord SOHO). The coronal gas is fully ionized and emits radiation mostly in the form of

[6]Large Angle and Spectrometric Coronagraph Experiment (LASCO) is a set of three coronagraphs that image the solar corona from 1.1 to 32 solar radii. http://lasco-www.nrl.navy.mil/

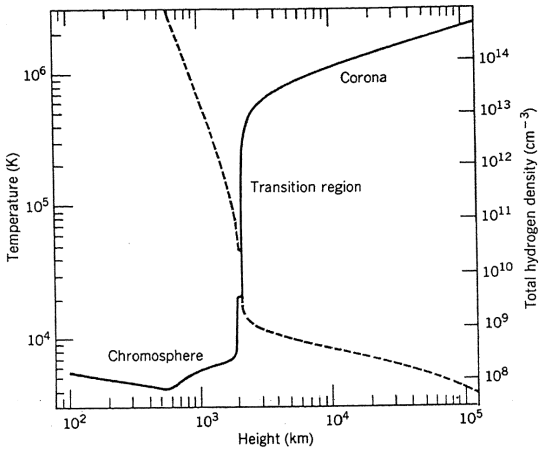

Figure 1.4: Temperature (solid line) and density (dashed line) dependence with the height over the solar surface, from A. Gabriel (1976) [24].

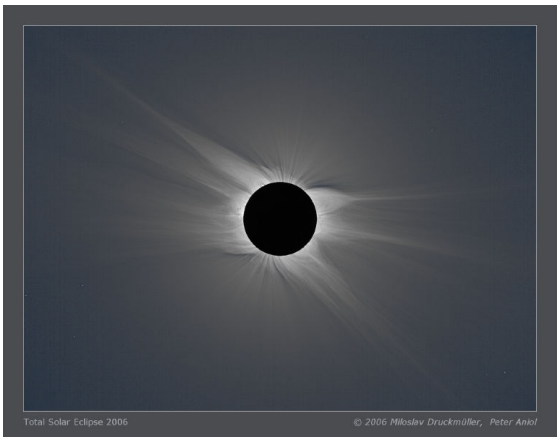

Figure 1.5: Solar corona during the total eclipse on 29–03–2006, credit M. Druckmüller and P. Aniol (2006).

line emission from highly ionized species (e.g., FeXVI, SIX, HeII).

In general, there are several different types of observations that are used to determine the coronal properties, namely in white light, EUV emission lines, soft and hard X-ray (e.g., from SOHO, TRACE[7], *Yohkoh*[8] and RHESSI[9], respectively, as well as with *Hinode*[10]). Such images reveal that the corona is highly structured consisting of complex fine filamentary loops, outwardly directed streamers, helmet-shaped structures/streamers, extending far out from the Sun. Around the poles, short streamers bending toward lower latitudes are detected. These polar jets are called polar plumes, that apparently follow the magnetic field lines of a global bar magnet with strength of 5–10 G, rooted in the center of the Sun [11].

One of the still open problems of the modern astrophysics is the source and the physical regime for the **heating of the solar corona**. Several different mechanisms were proposed, namely, heating by sound, magnetosound or Alfvén waves and later another idea for heating by micro- or/and nano-flares emerged. None of these mechanisms however was able to reproduce the expected value of the coronal temperature. Recent observation from MDI and EIT[11] aboard SOHO revealed the constant appearance and disappearance of magnetic bipoles at the feet of the magnetic loops. Due to ceaseless reconnection of these magnetic

[7] Transition Region and Coronal Explorer (TRACE) is a NASA Small Explorer (SMEX) mission to image the solar corona and transition region at high angular and temporal resolution. http://trace.lmsal.com/

[8] *Yohkoh* solar observatory satellite is a cooperative mission of Japan, the USA, and the UK. http://www.lmsal.com/SXT/homepage.html

[9] Reuven Ramaty High Energy Solar Spectroscopic Imager (RHESSI) is a NASA Small Explorer (SMEX) mission with primary mission to explore the basic physics of particle acceleration and explosive energy release in solar flares. http://hesperia.gsfc.nasa.gov/hessi/index.html

[10] *Hinode* (Solar B) is a Japanese satellite with three advanced solar telescopes aboard: solar optical telescope, X-ray telescope and EUV imaging spectrometer. http://solar-b.nao.ac.jp/

[11] Extreme ultraviolet Imaging Telescope (EIT). http://umbra.nascom.nasa.gov/eit/

loops all over the Sun (creating the so-called 'magnetic carpet' [109]), strong magnetic currents are generated in such magnetic short circuits that can heat the corona up to several million degrees.

Solar wind

It is well known that the solar corona is the source of the solar wind. The solar wind is not a uniform medium, but consists of two distinct types of streamers: slow and fast (see Fig. 1.6). The fast solar wind (400–800 km s^{-1}) originates from the coronal (polar) holes (see Fig. 1.8 in Sect. 1.2), where the magnetic field configuration is predominantly open. The slow solar wind (250–400 km s^{-1}) comes from open field lines above active regions and/or extention of coronal helmet streamers, that is from the nearly equatorial region (seen on Figs. 1.5 and 1.6). The overall temperature and density near 1 AU are 0.3–1$\times 10^5$ K and 10 cm^{-3}, respectively [93].

It was Parker (1958) who was able to present a model of the solar corona which cannot be in static equilibrium, but instead extending outwards as 'solar wind' [77]. The classical way is considering a steady, spherically symmetric expansion of isothermal plasma. The solar wind solution of such approach was observationally confirmed by one of the first satellite missions (Venus probe Mariner II in 1962) that measured the speed of the solar wind at Earth (of several hundred kilometers per second). Recently the *Ulysses*[12] mission substantially improved the overall knowledge about the 3D-structure of the heliosphere and the solar wind [121, 122].

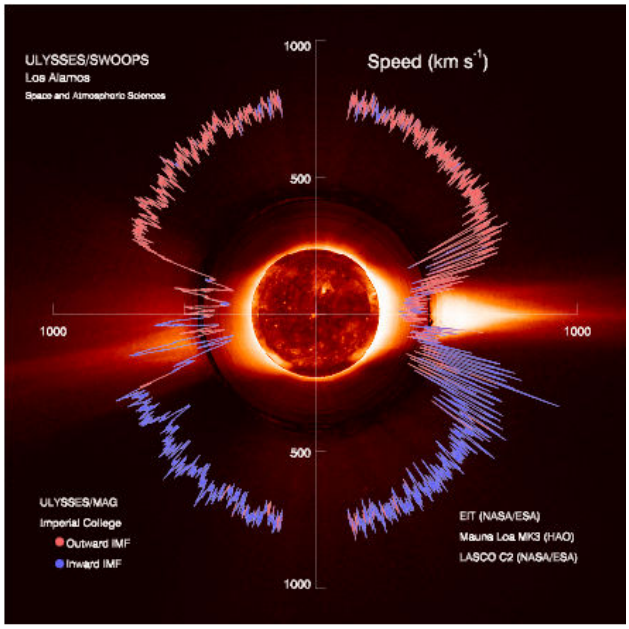

Figure 1.6: Plot of the solar speed as detected from *Ulysses* satellite (from NASA/ESA).

[12]The main scientific goal of the joint ESA-NASA *Ulysses* deep-space mission is to make the first-ever measurements of the unexplored region of space above the Sun's poles. http://helio.estec.esa.nl/ulysses/ http://ulysses.jpl.nasa.gov/index.html

1.2 The active Sun

The Sun is an active star. The solar atmosphere manifests this activity in various spatial (horizontal and vertical) and temporal (periodic and sporadic) scales. When observed in white light, the photosphere show one of the earliest discovered and most famous phenomena of the solar activity: the **sunspots** (see Fig. 1.3). Sunspots have horizontal extent comparable to the supergranulation cell, i.e., 20 000 km for the umbra and 40 000 km for the penumbra. The magnetic field in sunspots is 1000–3000 G (0.1–0.3 T), whereas the average surface field strength is about 1 Gauss (10^{-4} T). They appear dark (i.e., cooler) on the solar surface. The temperature of the umbra is about 3800 K, i.e., nearly 2000 K less than the surrounding photospheric gas. The sunspots are regarded as the manifestation of a magnetic field tube that emerges over the surface – and hence at least a pair of magnetic spots with opposite polarities is seen.

A plasma tube of enhanced magnetic field becomes buoyant in the convection zone because is less dense than the surrounding (field-free) plasma. The (plasma plus magnetic) pressure balance condition requires that such fluid should rise and during its upward motion it cools adiabatically (because the magnetic field prohibit convection). Thus it will appear colder on the surface in comparison with the surrounding plasma. Sunspots usually appear in groups and the field in the group can be unipolar, bipolar or very complex (see e.g., the Zurich classification system [39] and its modification by [63]). Sunspots mainly appear in two zones of heliospheric latitude in the northern and southern hemisphere (at around $\pm 35°$) and the leading sunspot in the group (in direction of the solar rotation) has the same polarity as the hemisphere where it is created. The total number of sunspots varies with a period of about 11 years – known as the **solar cycle**. The average latitude of the sunspot appearance migrates from mid-latitudes down to the equator region during the solar cycle, forming the famous **butterfly-diagram** (i.e., number of sunspots vs. time, see Fig. 1.7). The average solar magnetic field is roughly bipolar and the dipole switches its polarity every solar cycle as the reversal occurs during the solar maximum (maximum of sunspots). Thus the true period of the magnetic field is 22, instead of 11 years.

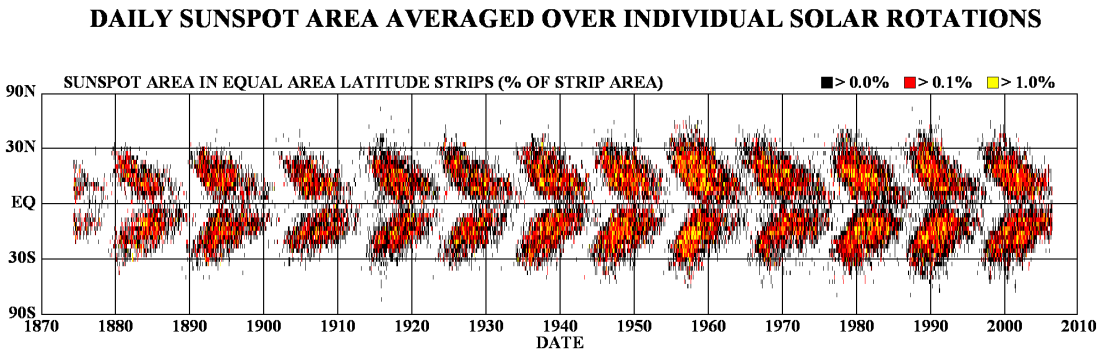

Figure 1.7: Butterfly diagram of the sunspots, from NASA/NSSTC/Hathaway 2006/07.

Active regions (ARs) appear as bright areas on the images in X-ray emission (see Fig. 1.8) at the equatorial belt (i.e., $\pm 30^\circ$ around the solar equator), and represent concentrations of magnetic flux with field strength greater than 100 G and temperature (in the corona) of about 2.5×10^6 K. Usually the active regions overlie sunspot groups in the photosphere. The distribution of the active regions changes during the solar cycle, for example during the solar minimum the few active regions are confined around the solar equator, whereas near the solar maximum they can be seen at higher heliospheric latitudes, which has the corresponding influence on the appearance of the solar corona as well.

A **coronal hole**, as for example is nicely seen at the pole of the Sun on Fig. 1.8, is an area of dilute plasma and predominantly open magnetic field lines, hence it appears dark in soft X-ray images. The coronal holes are the source of the fast solar wind. In contrast, regions of closed magnetic lines contain dense plasma and thus appear as bright coronal loops in soft X-ray. Morphologically the **coronal loops** (see Fig. 1.9) can be ordered, with increasing temperature and density levels but decreasing typical length, in the following way: interconnecting loops (joining different active regions, sometimes further apart), quiet-region loops, active region loops, post-flare loops and simple flare loops.

These coronal structures vary with the solar cycle, i.e., with the change of local and global

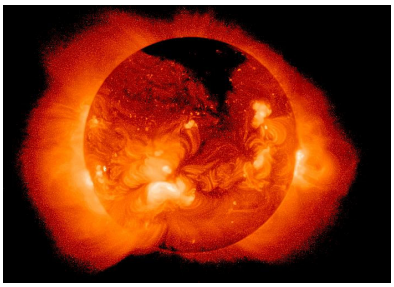

Figure 1.8: Polar coronal hole on the Sun, on 08–May–1992 in soft X-rays from *Yohkoh*.

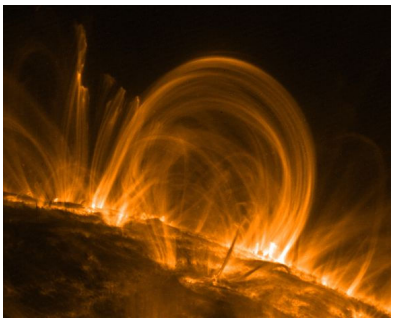

Figure 1.9: Coronal loop on 28–Sept–2000 from TRACE, credit M. Aschwanden.

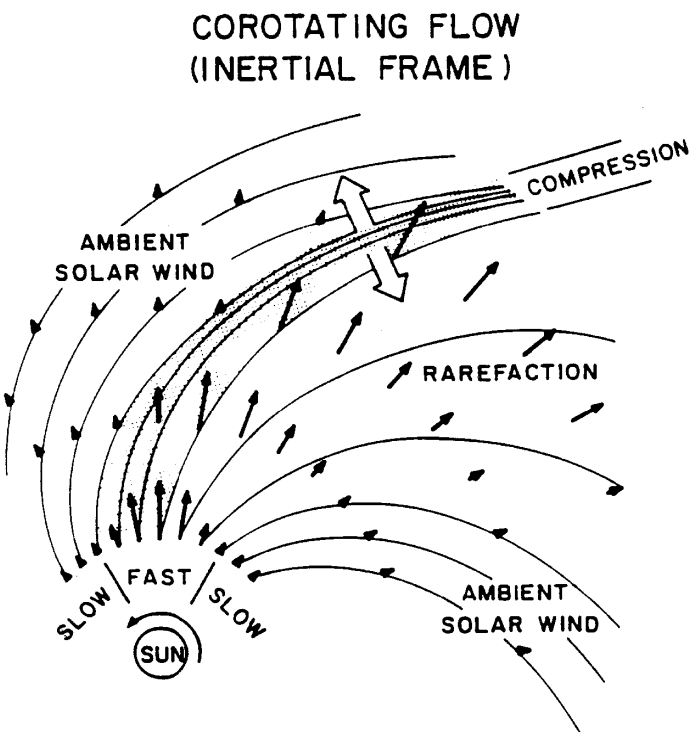

Figure 1.10: Sketch on 2D CIR in the solar equatorial plane in the inner heliosphere, from Pizzo (1978) [82].

magnetic field, which leads to the overall different shape of the solar corona (symmetric during solar maximum or with distinctive polar holes and extensive (helmet) streamers at the equatorial region during solar minimum, the latter case could be seen for example on Fig. 1.5).

The spatial inhomogeneity of the expanding solar corona and the rotation of the Sun, which cause fast and slow solar wind streamers to align radially, have an important consequence in the interplanetary region. Namely, compressive interaction regions are formed where the high-speed solar wind reaches and subsequently overcomes the slowly moving one. These regions spiral out from the rotating Sun in the equatorial plane that co-rotate with the Sun. Hence, they are named **co-rotating interaction regions**, or CIRs [82], see Fig. 1.10. They represent a contact discontinuity between the fast and slow solar wind streams, where the leading edge represents a forward pressure wave propagating ahead into the slower plasma, while the trailing edge is a reverse pressure wave, propagating back into the high-speed flow. Usually at distances beyond 1 AU, these areas of compression steepen and thus shock waves are formed (in many cases a pair of forward shock and reversed shock, correspondingly, [28]).

1.3 The flare

Solar flares represent the most powerful explosions in the solar system. Enormous amount of emitted radiation of the order of 10^{29} erg s^{-1} (10^{22} W) is released in a very short time scales of several seconds to few hours. This is less than 1/10 of the total energy emitted by the Sun every second, but even one small flare produces energy that is enough to supply Earth's consummation for million years [11].

The first solar flare published in astronomical literature was observed independently by Richard C. Carrington and Richard Hodgson on 1st September 1859. Both were doing sunspot observation in an active region, when a large flare in white light occurred. Presently, the solar flares are viewed with different instruments, from radio to hard X-ray wavelengths. The so-called 'Halloween' storm in 2003 has produced the most powerful flares detected so far, one of them is seen in an image from EIT on Fig. 1.11.

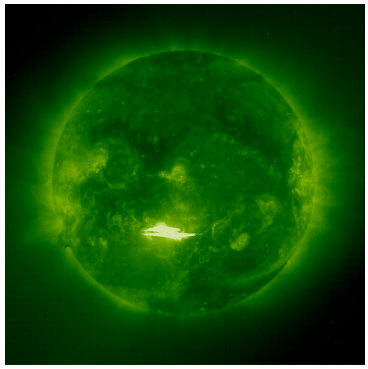

Figure 1.11: Flare event on 28–Oct–2003, from SOHO/EIT.

One can recognize three main stages for the flare energy, the so-called energy build-up, energy release and energy transport.

Because all flares occur in active regions, i.e., in regions of strong magnetic field, it should be the magnetic energy that supplies the flare. The basic idea is that the magnetic field configuration becomes stressed or sheared, a process that leads to a **build-up** of magnetic energy, previously stored in the solar corona. How this magnetic energy converts into flare energy, however, is still an open study.

One possible scenario of the **energy release** can be explained with the process of magnetic reconnection. When two magnetic field lines with opposite directions (see for example

Fig. 1.12) approach each other (e.g., due to their photospheric footpoint motion), a current sheet is established between them. If the electrons, carrying the current in this current sheet, have a velocity exceeding a certain critical value, plasma waves can be excited due to different plasma instabilities. The occurrence of these plasma waves leads to an enhancement of the resistivity, so-called anomalous resistivity [9]. The plasma and magnetic field decouple in a neutral X-point due to anomalous resistivity that arises in this very small, so-called diffusion region (DR). Thus, the magnetic field lines can disconnect and eventually rearrange. A new magnetic field configuration is established after reconnecting of the 'diffused' magnetic field lines. Because the stressed magnetic fields tend to be restored, the magnetic free energy is released by the process of magnetic reconnection, powering the solar flare (note that sheared magnetic field lines have more magnetic energy than potential field configurations). This energy release manifests itself as a sudden, rapid and intense brightening of the active region on the Sun. The overall time profile of the flare energy release, seen at various types of radiation (from radio to hard X-rays and γ-rays), can be divided to: *pre-cursor/pre-heating phase* (lasting 2–5 minutes, seen at some flares), *impulsive phase* (a sudden increase in brightness in the radio, microwave, EUV and hard X-ray emission, lasting from few seconds up to a minute), and *gradual phase* (sometimes with a flat plateau before the gradual decline, lasting from several minutes to hours) [11].

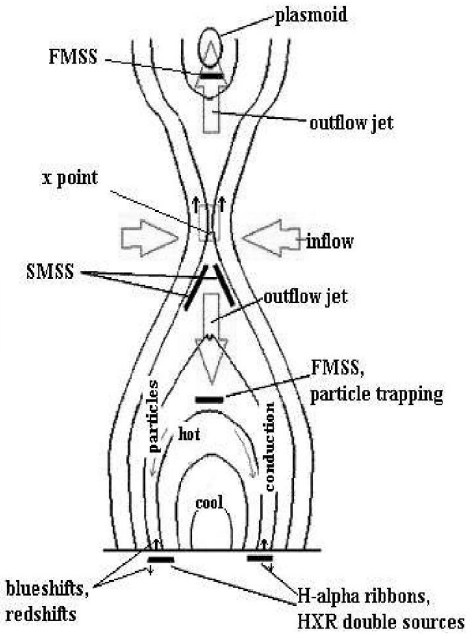

Figure 1.12: Vertical cut through the length axis of a two-ribbon flare (see in the text for abbreviations and further explanations), from [64].

The final stage for the flare energy is the **energy transport**, that covers a wealth of phenomena related to the transfer of the released energy. In general, the stored magnetic field energy is transformed into:
• plasma heating;
• accelerated particles (electrons, protons and heavy nuclei);
• plasma motions, e.g., plasma jets and/or coronal mass ejections (CMEs);
• shock waves;
• radiation across the entire electromagnetic spectrum, i.e., from radio waves, through the optical up to X-ray and γ-ray range.

From the presently available **flare models**, only the reconnection models of flares will be considered here, following a review by [96]. Various types of magnetic reconnection were already observed in the solar corona, as revealed by the soft X-ray images from *Yohkoh* satellite. A flare configuration [64] is shown on Fig. 1.12.

The general scenario starts when a filament (or plasmoid) becomes unstable and starts rising up. The underlying magnetic field lines are stretched and a current sheet is established under the erupting plasmoid. If the velocity of the electrons carrying this current

is exceeding a critical value, a local enhancement of the resistivity [9] occurs in the diffusion region (the X-point on Fig. 1.12). There, the magnetic field lines can reconnect and form a new magnetic field topology. Due to the strong curvature of the newly reconnected magnetic field lines in the vicinity of the diffusion region, the inflowing plasma is pushed away from the reconnection site, i.e., a plasma jet appears as really observed by the *Yohkoh* satellite [97, 106, 101]. The slow magnetosonic shocks (SMSS) (Fig. 1.12) divide the inflowing plasma from the outflowing one, or the pre-reconnection magnetic field from the post-reconnection one. At these slow shocks the plasma is strongly heated, so that the jet represents a hot plasma flow. The outflow jets go in two opposite directions. If the jet has a super-magnetosonic speed and accounts an obstacle on its way (e.g., the erupting plasmoid in the upwards motion and/or the dense post-flare loops in the downward motion), a standing fast magnetosonic shock (FMSS) is established there. Signatures of such a shock were really observed in terms of stationary type II radio burst pattern in the solar radio radiation [6]. These shocks could be the source of the energetic electrons needed for the nonthermal radio and X-ray radiation [111]. Thus, due to the magnetic reconnection energetic electrons are generated that travel along the magnetic field lines either towards the dense chromosphere, where they emit the X-ray radiation via Bremsstrahlung [12, 13] or in the higher corona and, subsequently, into the interplanetary space, where they can be observed in terms of the induced solar type III radio bursts. The chromospheric emission can be seen in the Hα ribbons and the double hard X-ray sources (Fig. 1.12).

1.4 Radio emission

The solar and interplanetary (IP) radio emission is considered to be generated mainly by plasma emission, occurring predominantly at frequencies below 1 GHz. When the solar plasma gets externally disturbed (e.g., by an electron beam or a shock wave), the electrons are excited to oscillate (as in the case of harmonic oscillator). The frequency of these oscillations is the electron plasma frequency, $\omega_{\rm pe} = (4\pi e^2 N_{\rm e}/m_{\rm e})^{1/2}$ (with e, electric charge, $N_{\rm e}$, the electron number density and $m_{\rm e}$, the electron mass). In plasma, a large variety of waves modes are present. Initially, the suprathermal electrons in the plasma excite high frequency electrostatic waves (e.g., Langmuir waves, with frequency near $\omega_{\rm pe}$ and/or upper hybrid waves). Subsequently, these waves convert into escaping electromagnetic (radio) waves by nonlinear interaction with low frequency plasma waves and/or scattering at ion density fluctuations [66]. This mechanism generates the fundamental emission near $f_{\rm pe} = \omega_{\rm pe}/(2\,\pi)$, whereas the coalescence of two high-frequency electrostatic waves leads to the harmonic emission. Thus, the radio waves are emitted near the local electron plasma frequency and/or its harmonics. Another important issue is that the electrons collectively emit radio waves in contrast to the gyrosynchrotron emission, where the electrons individually generate radio waves. Since the electron plasma frequency depends only on the electron number density (and natural constants), measuring the frequency of the radio emission gives us the density of the plasma that is responsible for this radiation. All that is needed to localize the radio emitter is an appropriate density model, giving the distribution of the density (and hence frequency) with height in the corona. This can be accomplish when one constructs a suitable coronal density model as a function of the height above the solar surface.

Such density model can be derived from the spherical solutions of magnetohydrostatic equations including the thermal pressure and the gravitational force of the Sun, see [57]. The analytical solution from these equations gives the barometric height formula,

$$N(r) = N_{\odot} \exp\left[A\left(R_{\odot}/r - 1\right)\right] \tag{1.1}$$

$$\text{with} \qquad A = \frac{m_{\mathrm{p}}\,\widetilde{\mu}\,G\,M_{\odot}}{k_{\mathrm{B}}\,T\,R_{\odot}} \qquad N_{\odot} = N(r = R_{\odot})$$

where m_{p} is the proton mass; $\widetilde{\mu}$ is the mean molecular mass (for solar corona and wind $\widetilde{\mu} \approx 0.6$ [83]); G is the gravitational constant; k_{B} is the Boltzmann constant; T is the temperature of the plasma and r is the distance from the solar surface. In contrast to such theoretical approach, a density model, deduced empirically from white light observation, was proposed by Newkirk [75]:

$$N(r) = \alpha N_0 10^{4.32\,R_{\odot}/r} \tag{1.2}$$

with $N_0 = 4.2 \times 10^4\,\mathrm{cm}^{-3}$ and the enhancement factor α is in the range 1–10. Note that $\alpha = 1$ is well appropriate for describing the density behaviour in the corona above quiet equatorial regions [41], $\alpha = 4$ is more suitable for the active regions, whereas $\alpha = 10$ should be used for very dense loops. For coronal temperature $T = 1.4 \times 10^6\,\mathrm{K}$ and $N_{\odot} = 8.775 \times 10^8\,\mathrm{cm}^{-3}$ at the base of the corona (and $A = 9.879$), the general barometric height model, Eq. (1.1), agrees with the one-fold Newkirk model (i.e., Eq. (1.2) with $\alpha = 1$) [57].

Additionally, a global magnetic field model is given in terms of the empiric model proposed by [21], namely

$$B(r) = 0.5\,\left(r/R_{\odot} - 1\right)^{-1.5}\ \text{Gauss}, \qquad 1.02\,R_{\odot} \lesssim r < 10\,R_{\odot}. \tag{1.3}$$

With such coronal density model (or/and magnetic field model), the measured (electron plasma) frequency and hence electron density (or/and magnetic field strength), can be assigned to certain coronal heights. Because the electron density monotonically decreases with height (Fig. 1.4), each layer of the solar atmosphere has its characteristic f_{pe} (and hence N_{e}), so higher/lower frequency (density) is emitted from at lower/higher distance above the photosphere, correspondingly.

Of course, the solar corona is strongly structured with respect to the density and the magnetic field, as already mentioned. Therefore, the presented formulas should be considered as a rough estimate, but they are very useful in order to deduce important physical parameters from the radio observation, as going to be demonstrated in the next Subsection.

1.4.1 Dynamic radio spectrum

A diagnostic tool for deriving important information from the parameters of the plasma processes, related with nonthermal electrons during solar flares, is the dynamic radio spectrum. The latter represents a plot of the intensity, I, of the nonthermal solar radio radiation, integrated over the whole disk, as a function of time t and frequency, f, i.e., as *frequency–time plot*, $f(t)$, where the intensity is color-coded (see for example Figs. 1.13–1.16). Usually, the

frequency (vertical axis) is chosen to increase downwards and the time (horizontal axis) runs to the right. The colour-coded intensity represents the third dimension of such a plot. With the so-chosen coordinate system, one can achieve a graphic representation that accounts for a gravitationally stratified atmosphere, i.e., with higher densities (because of the higher frequency) at the bottom and with lower densities at the top of the spectrum. Thus, such *frequency–time* diagram is in fact a *height–time plot*. Sometimes, the detected emission shows a drift toward lower/higher frequencies (so-called negative/positive drift). This feature is denoted as drift rate, D_f, and represents the frequency range/bandwidth (Δf) over the time spam/duration (Δt) of the emitting structure. The following important relationship between the D_f (deduced from observation) and the radial velocity of the source of emission is derived as

$$D_f \left(= \frac{\Delta f}{\Delta t} \right) := \frac{f}{2} \frac{1}{N_\mathrm{e}} \frac{\mathrm{d}N_\mathrm{e}}{\mathrm{d}r} V_\mathrm{source}, \tag{1.4}$$

where f is the observed frequency, and $\mathrm{d}N_\mathrm{e}/\mathrm{d}r$ denotes the radial density gradient along the propagation path of the radio source. Hence a global density model is needed to determine the source velocity. Finally, a negatively drifting feature represents a moving radio source upward in the solar corona, whereas a positively drift denotes a descending source toward the solar surface.

Plasma parameters	units	notation	55 MHz	300 MHz
electron number density$^{(*)}$	cm^{-3}	N_e	3.74×10^7	1.1×10^9
height$^{(**)}$	$R_\odot$	r	1.63	1.13
magnetic field strength$^{(***)}$	Gauss	B	1	10.7
plasma beta	—	β	0.36	0.1
electron plasma frequency	s^{-1}	ω_pe	0.345×10^9	1.885×10^9
proton plasma frequency	s^{-1}	ω_pi	0.8×10^7	4.39×10^7
electron cyclotron frequency	s^{-1}	ω_ce	1.758×10^7	1.758×10^8
proton cyclotron frequency	s^{-1}	ω_ci	0.958×10^4	9.58×10^4
frequency ratio S	—	$\omega_\mathrm{pe}/\omega_\mathrm{ce}$	19.6	10.7
Alfvén velocity	$\mathrm{km\,s}^{-1}$	v_A	360	700
electron thermal velocity	$\mathrm{km\,s}^{-1}$	$v_\mathrm{th,e}$	4608	4608
proton thermal velocity	$\mathrm{km\,s}^{-1}$	$v_\mathrm{th,i}$	107.5	107.5
Debye length	cm	λ_De	1.336	0.24
electron Larmor radius	cm	r_Le	26.21	2.6
proton Larmor radius	cm	r_Li	1123	112
electron inertial length	cm	d_e	86.96	15.9
proton inertial length	cm	d_i	3750	683

Table 1.1: Plasma parameters for 55 and 300 MHz. The coronal temperature is 1.4 MK, corresponding to $k_\mathrm{B}\,T = 120\,\mathrm{keV}$. $^{(*)}$ N_e is deduced from the electron plasma frequency, ω_pe; $^{(**)}$ r is deduced from the Newkirk model [75], Eq. (1.2), with $\alpha = 4$ (for 300 MHz) and $\alpha = 2$ (for 55 MHz); $^{(***)}$ B is deduced from the Dulk & McLean model [21], Eq. (1.3).

Two important examples of radio emission are of special interest for the present thesis and will be presented in more details, namely the type II and type III metric radio bursts. Because their emission is typically observed at 55 MHz and 300 MHz, respectively, the main plasma parameters (see Table 1.1), corresponding to these frequencies, are calculated according to the expressions summarized below:

$$\beta = \frac{16\pi\, N_\mathrm{e}\, k_\mathrm{B}\, T}{B^2}, \quad \omega_{\mathrm{p}j} = \left(\frac{4\pi e^2 N_\mathrm{e}}{m_j}\right)^{1/2}, \quad \omega_{\mathrm{c}j} = \frac{e\,B}{c\,m_j}, \quad v_\mathrm{A} = \frac{B}{(4\pi m_\mathrm{i}\, N_\mathrm{e})^{1/2}},$$

$$v_{\mathrm{th},j} = \left(\frac{k_\mathrm{B}\, T_j}{m_j}\right)^{1/2}, \quad \lambda_\mathrm{De} = \left(\frac{k_\mathrm{B}\, T_\mathrm{e}}{4\pi e^2 N_\mathrm{e}}\right)^{1/2} = \frac{v_\mathrm{th,e}}{\omega_\mathrm{pe}}, \quad r_{\mathrm{L}j} = \frac{v_{\mathrm{th},j}}{\omega_{\mathrm{c}j}}, \quad d_j = \frac{c}{\omega_{\mathrm{p}j}},$$

where the lower index 'j' substitutes 'e' for an electron or 'i' for a proton, respectively and for the temperature of the corona is assumed to be 1.4 MK.

Type II

Type II radio bursts (see Fig. 1.13) are narrow band emission stripes with slow drift towards lower frequencies, $D_f \simeq -(0.1\text{–}1)\,\mathrm{MHz\,s^{-1}}$. Both fundamental and harmonic band can be present, and sometimes each band is split into a higher and lower frequency lane (with relative separation of $\Delta f/f \simeq 0.1$) [74, 51]. It is mostly observed in the metric range, but IP type II bursts are also observed in the decametric/kilometric regimes.

A type II burst is generated by a shock wave propagating outward through the corona [74]. In the solar corona and the IP medium, a type II-generating shock is formed when the exciting disturbance exceeds the local Alfvén speed. The typical type II velocities are of the order of $1000\,\mathrm{km\,s^{-1}}$ [58]. At the shock front, the electrons are accelerated to suprathermal and/or higher energies. The type II bursts can be associated both with flares [117] and coronal mass ejections (CMEs) [26], though there could be also no correspondence [86, 95]. The present view is that there are in general two ways for shock formation (that later

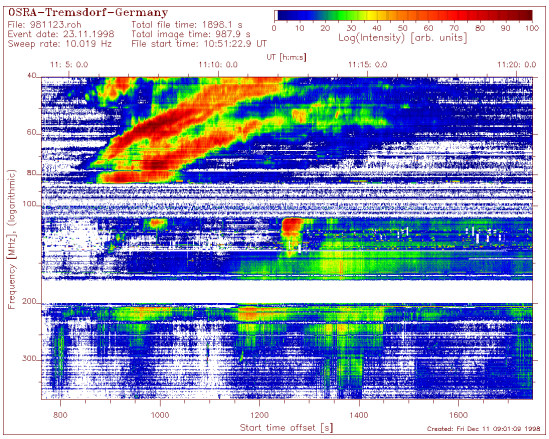

Figure 1.13: Dynamic spectrum of type II burst from OSRA Tremsdorf, Germany.

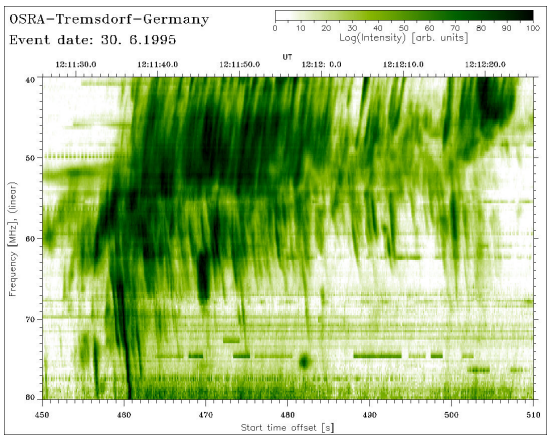

Figure 1.14: Dynamic spectrum of herringbones from OSRA Tremsdorf, Germany.

on produces the burst itself), namely: flare-associated pressure pulse/blast wave [117] and piston-driven shock wave, created by CMEs [2, 46]. Usually the flare-generated disturbances cannot penetrate into the IP space, since most of the bursts in the higher corona cease around the 20 MHz level. Therefore, most hectometric/kilometric type II bursts seem to be generated by CME-driven shocks.

Type II bursts usually consist of two components [74]. The so-called 'backbone' (Fig. 1.13) is an emission lane slowly drifting from high to low frequencies with $D_f \simeq -0.1375\,\mathrm{MHz\,s^{-1}}$ which corresponds to a mean source velocity of $\bar{V}_{\mathrm{BB}} \simeq 950$–$1000\,\mathrm{km\,s^{-1}}$, by means of a two-fold Newkirk model [75]. A two-fold Newkirk model is appropriate since type II burst sources appear not radially above the active regions but more oriented to the motion of the plasma blob, that was theoretically treated in [60]. Furthermore, rapidly drifting stripes of enhanced radiation are shooting up and down from the **'backbone'** toward lower and higher frequencies, respectively. These are called **'herringbones'** [14] with typical positive and negative drifts $D_f \simeq \pm 7\mathrm{MHz\,s^{-1}}$, see Fig. 1.14, and mean source velocity $\bar{V}_{\mathrm{HB}} \simeq 50\,000\,\mathrm{km\,s^{-1}} \simeq 0.17\,c$, using again the two-fold Newkirk model. Because of their rapid drift they resemble to type III bursts, but in general the drift rate of the herringbones is approximately a half of the type III-drift rate for the same frequency range, as was calculated by [58]. In summary, the 'backbone' emission is a signature of a moving shock wave through the corona, whereas the 'herringbones' are signatures of electron beams accelerated by the shock wave [59].

Type III

Type III radio bursts (Fig. 1.15) are the most common flare associated radio bursts. They occur on a wide frequency range $10\,\mathrm{kHz} \leq \Delta f \leq 1\,\mathrm{GHz}$, corresponding to height range from the low corona to beyond 1 AU [107]. The typical type III burst values are: broad bandwidth $\Delta f \simeq 100\,\mathrm{MHz}$, short duration ($\Delta t$ is just few seconds), and hence, fast drift rate $D_f \simeq -100\,\mathrm{MHz\,s^{-1}}$ [120]. Many bursts at metric and decametric wavelengths display harmonic structure and often appear in groups.

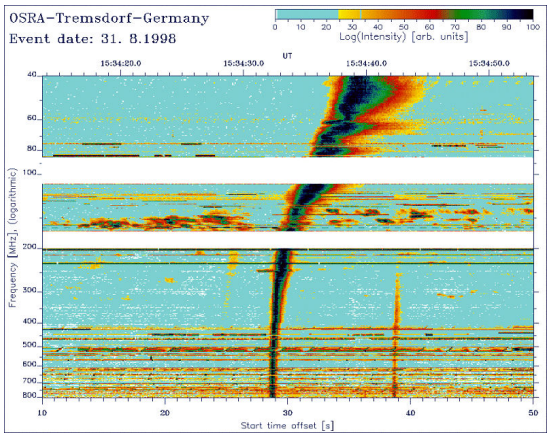

Figure 1.15: Dynamic spectrum of type III burst from OSRA Tremsdorf, Germany.

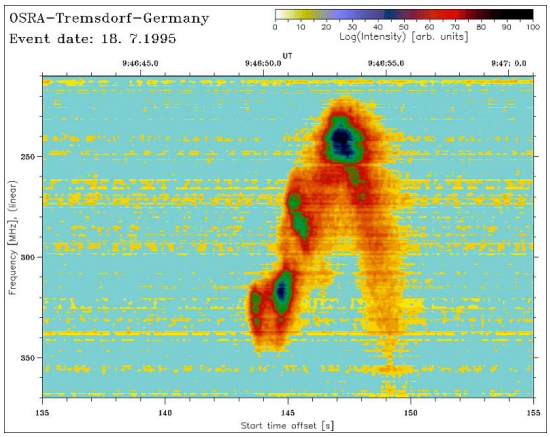

Figure 1.16: Dynamic spectrum of type U bursts from OSRA Tremsdorf, Germany.

Type III radio bursts are characteristic of the impulsive phase of the solar flare (see Sect. 1.3). The electron beams associated with type III burst are believed to be immediately accelerated in the reconnection site [31]. It is widely accepted that the exciting agent of the type III burst is a beam of mildly relativistic electrons (with velocity $\simeq 0.3\,c$), propagating along the magnetic field lines. If they meet open field lines, they can travel along them through the corona (and sometimes even out up to the IP space) where they generate type III radio bursts, [107] (see Fig. 1.15). When the beam propagates along a closed magnetic loop, a so-called (inverted) U radio burst results in the radio spectrum (see Fig. 1.16) [3, 4]. When the type III associated electron beam propagates through the IP space up to Earth, the electrons that generate it can be directly observed as impulsive electron events (see Subsect. 1.5.3). Type III bursts, therefore, give vital clues on the acceleration of electrons in flares, as well as on the propagation of these electrons (the energy transport) through the IP space.

1.5 Other solar phenomena

Our Sun manifests a spectrum of mass motions, from the relatively small (as compared to the solar radius) scale motion seen in granulation, supergranulation, sunspots to large scale motion like solar jets, CMEs, and solar wind. Another important phenomenon is the acceleration of charges particle populations up to high energies at flare sites or/and shock waves in the corona and in IP space (the so-called solar energetic particles, SEPs). Taking into account the topic of this thesis, a brief introduction to solar jets, CMEs and SEP events is required and will be given below.

1.5.1 Solar jets

A solar jet is defined as transitory X-ray enhancement with apparent collimated motion by [97], as (re-)discovered from SXT[13] / *Yohkoh* satellite. Presently, TRACE mission keeps providing images of solar jets in EUV, see Fig. 1.17.

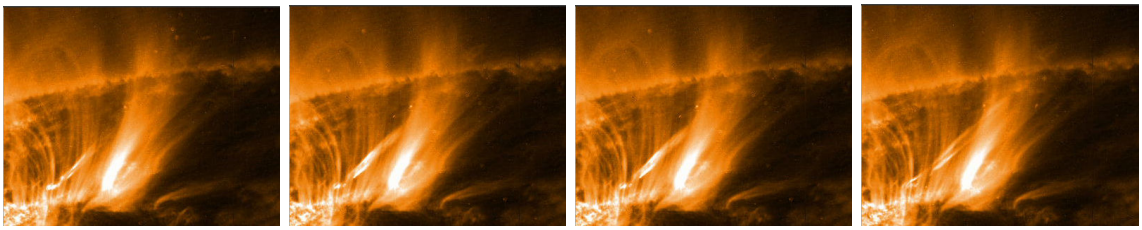

Figure 1.17: Solar jet from TRACE, on 19–Jul–2000 at 171Å.

The magnetic field configuration possibly leading to the formation of solar jets in the solar corona is sketched on Fig. 1.18. It is considered that the process of magnetic reconnection can lead to the formation of plasma jets due to the relaxation of the stressed magnetic field lines (see Sect. 1.3).

[13]SXT stands for the Soft X-ray Telescope aboard the *Yohkoh* satellite.

There exists generally two types of solar jets: **anemone** and **two-sided loop jet** (see Fig. 1.19). When the emerging flux is ascending near a coronal hole (i.e., quiet coronal region), the magnetic reconnection between the emerging flux region (EFR) and the overlying coronal field leads to the formation of anemone-type jet, that is expelled in nearly vertical direction, see Fig. 1.19 (a) and (c). When, however, the emerging flux appear inside an active region with closed magnetic field lines, as a result from the reconnection process, two jets occur in nearly horizontal direction at both sides of the emerging flux. This is the so-called two-sided loop jet, see Fig. 1.19 (b) and (d). Magnetic reconnection should be regarded as just one of the possible mechanisms, explaining the jet formation, but simulations based on it, as performed by [124, 125], confirm most of the observed jet characteristics.

Finally, a summary of the typical physical parameters of the soft X-ray jets is given [100]:

- **Temperature**: 3–8 $\times 10^6$ K, average 5.6 $\times 10^6$ K
- **Density**: 0.7–4 $\times 10^9 \mathrm{cm}^{-3}$, average 1.7 $\times 10^9 \mathrm{cm}^{-3}$
- **Apparent speed**: 10–$10^3 \mathrm{km\,s}^{-1}$, average 200 $\mathrm{km\,s}^{-1}$
- **Lifetime**: 100 seconds to some hours

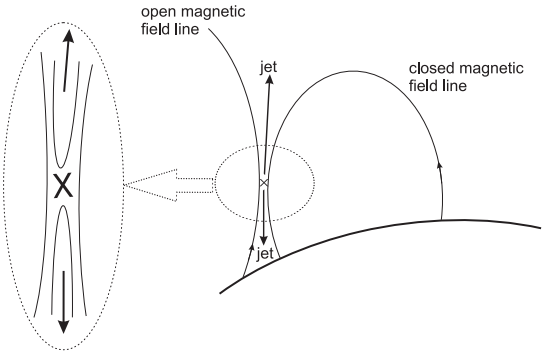

Figure 1.18: Sketch of a magnetic reconnection possibly leading to the formation of solar jets.

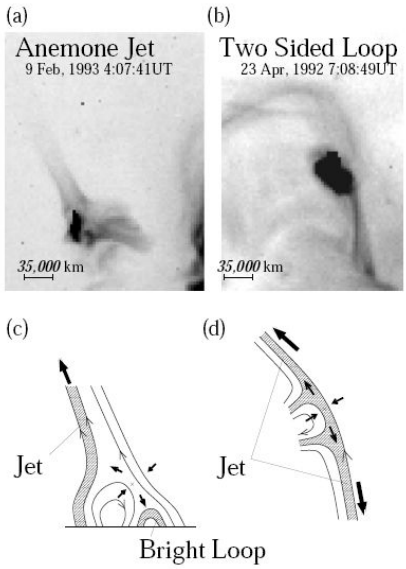

Figure 1.19: Two main configurations for a solar jet, from [125].

1.5.2 Coronal mass ejections (CMEs)

The coronal mass ejection (or CME for short) is a large magnetized volume of solar plasma moving outward from the Sun (Fig. 1.20). They could be seen as rapidly expanding in size filament- or loop-like huge bubbles or irregular-shaped amount of gas, but much of the variety of shapes is due to projection effects. If a so-called 'light bulb' CME, usually seen at mid-latitudes when projected on the sky, occurs close to the solar disk center, the resulting image will resemble to a bright 'splash' surrounding (completely or not) the disk of the coronograph. Thus, the so-called 'halo' or 'partial halo' CME is observed, respectively. The general CME's properties, as summarized by [94], are:

- Measured **speed** ranges from few kilometers per second to 3000 km s^{-1};
- Apparent **angular width** ranges from a few degrees to more than 120°;
- Total **ejected mass** ranges from some 10^3 g to few 10^{16} g (average 1.4×10^5 g);
- Total (kinetic and potential) **energy** ranges from 10^{27} to 10^{33}erg (average 2.6×10^{30}erg).

In the case of a 'light-bulb' CME there is an apparent three-part structure: a bright outer loop as the leading edge of the CME followed by a darker region – void or cavity which represent a depletion in the plasma density and finally a bright kernel or knot, that could be a remnant of a prominence.

Generally, CMEs arise from large-scale closed magnetic structures. The temporal and latitudinal distribution of CMEs show similarities to the distribution of coronal streamers, prominences and filaments. At solar minimum the source regions of the CMEs clearly peak at the solar equator, whether at solar maximum CMEs are seen at broader regions of the Sun. The frequency of their occurrence follows the 11-year solar cycle. Presently, it is thought that there are flare- and non-flare-associated CMEs [119]. Although in the majority of the cases both CME and flare are detected, there are also number of instances wherein a flare was seen but no CME followed. Hence, it is possible CMEs to occur before, during and after a flare, therefore a localized flare event in general does not seem to be necessary connected with such global phenomenon as CME, according to [11]. An example for flare-related CME is shown on Fig. 1.20. Presently, the STEREO[14] mission is expected to give further insights on the causes, mechanisms and propagation of the CMEs, observing the Sun in 3D by the two nearly identical satellites.

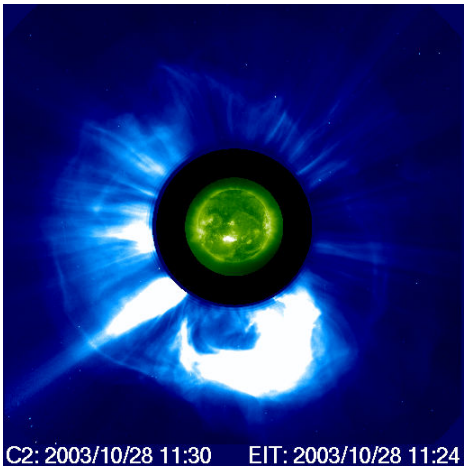

Figure 1.20: CME from LASCO C2-coronograph on SOHO and an EIT image, from 28–Oct–2003 flare.

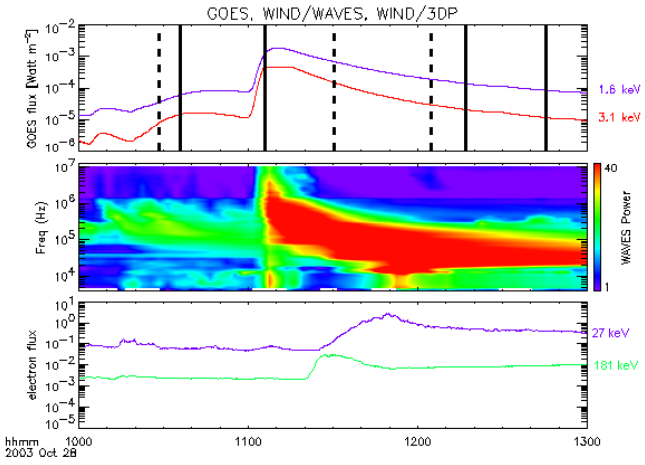

Figure 1.21: Impulsive electron event: GOES soft X-ray curves, WIND/WAVES dynamic spectra, and WIND/3DP electron flux (top–to–bottom panels).

[14]STEREO (Solar TErrestrial RElations Observatory) is a NASA's Solar Terrestrial Probes Program mission for stereoscopically observation of the Sun in order to study the nature of coronal mass ejections. http://stereo.jhuapl.edu/

1.5.3 Solar energetic particle events (SEPs)

Various highly dynamic processes in the magnetized coronal and IP plasma can cause major acceleration of the charged particles. The main locations for the electron and ion acceleration are flare sites and shock waves in the corona and IP space. The energy of these SEPs ranges from few keV for the suprathermal particles up to some GeV (e.g., the protons at flares). The fastest particles obtain velocities $> 0.5\,c$ and arrive at Earth shortly after the observed light flash. When they happen to hit the CCD-cameras of the orbiting satellite, such particles produce the well-known 'snow-storms' that usually follow a detection of a strong flare or a CME. Also they are of particular interest for the space weather concept. The SEPs contain electrons, protons, ions, and neutrons.
It is now largely agreed that SEPs come from two different sources with different acceleration mechanisms, namely *impulsive SEP events*, released from flares (Fig. 1.21) and *gradual SEP events*, caused by CME-related shocks. Generally, the peak proton intensity in the case of gradual SEPs was found to correlate best with the shock passage from moving CME. As presented on Fig. 1.21, energetic electrons traveling toward us can be detected by the instruments aboard the orbiting satellites (for example by the WAVES and 3D Plasma instruments aboard the WIND[15] mission). The electron flux curves on the bottom panel clearly show that the more energetic populations travel faster and reach Earth first and thus are important for the space weather concept. The most intensive SEP events are produced by CME-driven shocks, but only the fastest (about 1%) of all CMEs can produce significant SEP events [94]. There are variety of processes that produce the fluxes of non-thermal electrons, being of main interest in the present dissertation, namely: (i) events with energy spectra that extend to the suprathermal range (down to 2 keV), originating high in the corona; (ii) electrons accelerated at flare sites, having very wide energy spectrum that cause the type III radio bursts; (iii) electrons accelerated at propagating coronal shock waves (both up- and downward), leading to the characteristic herringbone pattern in the radio spectra.

In the present Chapter, a general overview of the solar interior, atmosphere and some of the most famous solar phenomena, was presented, without the aim of completeness. A special attention is drawn toward those features, that later are going to be used for the theoretical modeling in the dissertation. For the theoretical research done in Chapter 4, for example, the physical properties of the solar jets and type III radio bursts are needed. In Chapter 5, however, the characteristics of a coronal shock wave in terms of a type II burst, together with some additional information provided from CIR-related shocks, is used. Both configurations could be initiated by a flare event or/and CME. Hence, the aim of this Introduction, is to present those phenomena and their properties, that are necessary as input parameters for constructing the new theoretical models. To propose new theoretical models on electron acceleration in the solar corona, more specifically considering localized wave structures due to solar jets and shock waves, is the subject of this dissertation.

[15] WIND is NASA spacecraft in the Global Geospace Science initiative, in order to investigate basic plasma processes occurring in the near-Earth solar wind. http://pwg.gsfc.nasa.gov/wind.shtml

Chapter 2

The multi-fluid equations

2.1 Introduction

Because of its million degree temperature, the solar corona is in a fully ionized plasma state, containing electrons, protons and heavy ions. Such a plasma medium can be appropriately described by the multi-fluid equations. The multi-fluid approach regards each particle species as an individual fluid and thus each fluid is described by its equation of continuity, momentum and equation of state. In the general case, the equations for each fluid can be summarized in the system below, where the subscript 'j' denotes the different particle species, i.e., 'e' for electrons or 'i' for protons, correspondingly.

Equation of continuity

$$\frac{\partial N_j}{\partial t} + \nabla \cdot (N_j \mathbf{v}_j) = 0 \tag{2.1}$$

Momentum equation

$$m_j\, N_j \left[\frac{\partial}{\partial t} + \mathbf{v}_j \cdot \nabla\right] \mathbf{v}_j = -\nabla p_j + q_j\, N_j \left[\mathbf{E} + \frac{1}{c}(\mathbf{v}_j \times \mathbf{B})\right] \tag{2.2}$$

The different particle fluids interact with each other by the external and self-induced electric and magnetic fields, which are governed by the Maxwell's equations.

Maxwell equations

$$\nabla \cdot \mathbf{E} = 4\pi \sum_j q_j N_j \tag{2.3}$$

$$\nabla \cdot \mathbf{B} = 0 \tag{2.4}$$

$$\nabla \times \mathbf{E} = -\frac{1}{c}\frac{\partial \mathbf{B}}{\partial t} \tag{2.5}$$

$$\nabla \times \mathbf{B} = \frac{4\pi}{c} \sum_j q_j N_j \mathbf{v}_j + \frac{1}{c}\frac{\partial \mathbf{E}}{\partial t} \tag{2.6}$$

The multi-fluid equations can be closed with the so-called equation of state[1] for the pressure of each individual fluid,

$$p_j = p_{j0} \left(\frac{N_j}{N_{j0}} \right)^{\gamma}. \tag{2.7}$$

The index $\gamma = c_p/c_v$, the ratio of the specific heat at constant pressure and constant volume, is constant for the case of collisionless ideal isotropic plasma. It can be regarded in the general case as the *polytropic index*, comprising different cases in it, e.g., isothermal case, with $\gamma = 1$, and adiabatic case, with $\gamma = 5/3$. The expression for the gradient of the pressure is:

$$\frac{1}{m_j\, N_j} \nabla p_j = \frac{\gamma}{m_j\, N_j} \frac{p_{j0}}{N_{j0}} \left(\frac{N_j}{N_{j0}} \right)^{(\gamma-1)} \nabla N_j = \gamma \frac{V_{\mathrm{T}_j}^2}{N_j} \left(\frac{N_j}{N_{j0}} \right)^{(\gamma-1)} \nabla N_j, \tag{2.8}$$

where the thermal velocity, defined as $V_{\mathrm{T}j}^2 = k_{\mathrm{B}}\, T_j/m_j$, is used and k_{B} is the Boltzmann's constant. Combining Eqs. (2.5) and (2.6), a wave equation naturally arises and its general form is given below:

$$\nabla(\nabla \cdot \mathbf{E}) - \Delta \mathbf{E} + \frac{1}{c} \frac{\partial^2 \mathbf{E}}{\partial t^2} = -\frac{4\pi}{c^2} \sum_j q_j N_j \frac{\partial}{\partial t} \mathbf{v}_j. \tag{2.9}$$

These are the basic equations for the linear wave analysis (see Subsect. 2.3).

2.2 Normalization of the multi-fluid equations

The multi-fluid equations must be normalized in order to obtain a dimensionless system of equations, that later on is going to be solved numerically. All physical quantities (i.e., number density, temperature, magnetic field) are normalized with respect to their undisturbed (or background) values. In addition, the spatial and temporal coordinates are normalized to the characteristic length scale L_0 and the inverse of a characteristic frequency ω_0, respectively. Consequently, the velocities need to be normalized with respect to the quantity $V_0 = L_0\, \omega_0$. Denoting the dimensionless quantities with primes and the characteristic ones with subscript 0, the general form for the normalization used further on is:

$$\begin{aligned} \mathbf{B}' &= \frac{\mathbf{B}}{B_0}; \quad \mathbf{E}' = \frac{\mathbf{E}}{E_0}; \quad N_j' = \frac{N_j}{N_{j0}}; \quad \mathbf{v}'_j = \frac{\mathbf{v}_j}{V_{j0}}; \quad T' = \frac{T}{T_0}; \\ \omega' &= \frac{\omega}{\omega_0}; \quad t' = \omega_0\, t; \quad \mathbf{r}' = \frac{\mathbf{r}}{L_0}; \quad \nabla' = L_0 \nabla; \quad \mathbf{k}' = L_0 \mathbf{k}. \end{aligned} \tag{2.10}$$

Here, ω and $\mathbf{k}$ represents the frequency and the wave number vector of a plane wave. According to the induction equation (2.5), the general form of the dimensionless electric field needs to obey the relation,

$$E_0 = \frac{\omega_0\, B_0\, L_0}{c}. \tag{2.11}$$

[1] The actual form of the equation of state depends on the assumption for the pressure tensor (e.g., isotropic or anisotropic) and also on the multi-fluidity of the plasma (i.e., the number of all particle species). In the case of isotropic pressure, the general pressure tensor reduces to a diagonal one with equal non-zero elements.

The choice for the characteristic values is arbitrary but is usually intrinsically justified for each particular plasma configuration. A summary of all different normalizations used in the dissertation is given below:

- Nonlinear solution of the Sakai–Sonnerup system (Chapter 3)

$$\begin{aligned} E_0 &= \omega_{\rm ci}\, B_0/\omega_{\rm pi}; \qquad N_{j0} = N_{\rm e0}; \qquad V_{j0} = v_{\rm A}; \\ \omega_0 &= \omega_{\rm ci}; \qquad L_0 = c/\omega_{\rm pi}. \end{aligned} \tag{2.12}$$

- Electrostatic wave excitation due to solar jet in the solar corona (Chapter 4)

$$\begin{aligned} E_0 &= \frac{k_{\rm B}T_{\rm e}}{e\lambda_{\rm De}}; \qquad N_{j0} = \nu_j N_0; \qquad V_{j0} = V_{\rm th,e}; \qquad T_{j0} = \theta_j T_0; \\ \omega_0 &= \omega_{\rm pe}; \qquad L_0 = \lambda_{\rm De}. \end{aligned} \tag{2.13}$$

- Attached whistler wave packages at coronal shock (Chapter 5)

$$\begin{aligned} E_0 &= \omega_{\rm ce}\, B_0/\omega_{\rm pe}; \qquad N_{j0} = N_0; \qquad V_{j0} = V_{\rm th,e}; \qquad T_{j0} = T_0; \\ \omega_0 &= \omega_{\rm ce}; \qquad L_0 = c/\omega_{\rm pe}. \end{aligned} \tag{2.14}$$

The parameters ν_j and θ_j in (2.13), denote how the particles are distributed in density and temperature over the whole plasma, respectively, in the assumed in Chapter 4 multi-component plasma. A pure electron–proton plasma is considered in the other two cases (i.e., Chapter 3 and 5). Further on, one can rearrange the general relations (2.10) in expressions for the physical quantities, namely:

$$\mathbf{B} = \mathbf{B}'B_0; \quad \mathbf{E} = \mathbf{E}'E_0; \quad N_j = N_j'N_0; \quad \mathbf{v}_j = \mathbf{v}'_j V_{j0}; \quad T_j = T_j'T_0;$$

$$\omega = \omega'\omega_0; \quad t = t'\omega_0^{-1}; \quad \mathbf{r} = L_0\,\mathbf{r}'; \quad \nabla = \frac{\nabla'}{L_0}; \quad \mathbf{k} = \frac{\mathbf{k}'}{L_0}; \quad \frac{\partial}{\partial\, t} = \omega_0 \frac{\partial}{\partial\, t'},$$

that need to be substituted in the corresponding system of equations, in order the latter one to be normalized.

2.3 Linear wave analysis

The easiest way to solve the multi-fluid equations is to perform the linear wave analysis, i.e., assuming that all dependent variables can be presented as a sum of 'equilibrium' (i.e., background, given with subscript '0') and 'perturbed' (i.e., oscillating, given with 'δ') parts, namely,

$$\alpha = \alpha_0 + \delta\alpha \qquad \text{with} \qquad \delta\alpha \ll \alpha_0,$$

where α stands as abbreviation for the density N_j, the velocity v_j, the electric $\mathbf{E}$ and the magnetic $\mathbf{B}$ fields, correspondingly. The equilibrium quantities express the plasma state in the absence of motions (so, $v_0 = E_0 = 0$ is assumed henceforth). Usually one

considers a small perturbation that is introduced to the uniform neutral plasma (where $\nabla\alpha_0 = \partial\alpha_0/\partial\, t = 0$ is valid for the initial plasma state) or finally:

$$\begin{aligned} N_j &= N_{j0} + \delta N_j \\ \mathbf{v}_j &= \delta\mathbf{v}_j \\ \mathbf{E} &= \delta\mathbf{E} \\ \mathbf{B} &= \mathbf{B}_0 + \delta\mathbf{B} \end{aligned}$$

The above expressions are substituted in the multi-fluid equations, (2.1), (2.2), (2.8) and (2.9), and after keeping only the linear terms, the final linearized multi-fluid equations are:

$$\frac{\partial}{\partial t}\delta N_j + N_{j0}\nabla\cdot\delta\mathbf{v}_j = 0 \tag{2.15}$$

$$\frac{\partial}{\partial t}\delta\mathbf{v}_j = -\frac{\gamma V_{\mathrm{T}j}^2}{N_{j0}}\nabla\delta N_j + \frac{q_j}{m_j}\delta\mathbf{E} + \frac{q_j}{c\, m_j}(\delta\mathbf{v}_j\times\mathbf{B}_0) \tag{2.16}$$

$$\nabla(\nabla\cdot\delta\mathbf{E}) - \Delta\delta\mathbf{E} + \frac{1}{c}\frac{\partial^2\delta\mathbf{E}}{\partial t^2} = -\frac{4\pi}{c^2}\sum_j q_j N_{j0}\frac{\partial}{\partial t}\delta\mathbf{v}_j \tag{2.17}$$

Additionally the background magnetic field is chosen to be aligned to the $\hat{z}$-axis, i.e., $\mathbf{B}_0 = B_0(0,0,1)$ and the wave vector takes and angle θ to the $\hat{z}$-axis, i.e., $\mathbf{k} = k(\sin\theta, 0, \cos\theta)$, see Fig. 2.1. The harmonic wave analysis implies that all perturbed quantities can be presented in the following way,

$$\delta\alpha_j = \alpha_j^{\mathrm{A}}\, e^{i(\mathbf{k}\cdot\mathbf{r}-\omega\, t)},$$

where the notation for the amplitudes (superscript A) will be dropped henceforth.

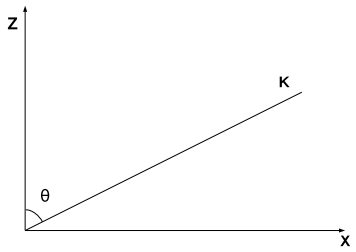

Figure 2.1: Sketch of the configuration.

Following the plane wave analysis, one can express $\nabla \to ik$ and $\partial/\partial t \to -i\omega$. Then the linearized system of equations (2.15)–(2.17) provides:

$$\omega\, N_j = N_{j0}(\mathbf{k}\cdot\mathbf{v}_j) \tag{2.18}$$

$$-i\omega\mathbf{v}_j = -i\frac{\gamma V_{\mathrm{T}j}^2}{\omega}\mathbf{k}(\mathbf{k}\cdot\mathbf{v}_j) + \frac{q_j}{m_j}\mathbf{E} + \frac{\omega_{\mathrm{c}j}}{B_0}(\mathbf{v}_j\times\mathbf{B}_0) \tag{2.19}$$

$$-\mathbf{k}(\mathbf{k}\cdot\mathbf{E}) + k^2\mathbf{E} - \frac{\omega^2}{c^2}\mathbf{E} = i\frac{4\pi\omega}{c^2}\sum_j q_j N_{j0}\mathbf{v}_j \tag{2.20}$$

Then, Eq. (2.19) is written by components:

$$\begin{pmatrix} \omega - a_j\sin^2\theta & -i\omega_{\mathrm{c}j} & a_j\sin\theta\cos\theta \\ i\omega_{\mathrm{c}j} & \omega & 0 \\ -a_j\sin\theta\cos\theta & 0 & \omega - a_j\cos^2\theta \end{pmatrix}\begin{pmatrix} v_{jx} \\ v_{jy} \\ v_{jz} \end{pmatrix} = i\frac{q_j}{m_j}\begin{pmatrix} E_x \\ E_y \\ E_z \end{pmatrix}, \tag{2.21}$$

where $a_j = \gamma V_{\mathrm{T}j}^2 k^2/\omega$. The solution of Eq. (2.21) can be given in terms of

$$v_{jx} = \frac{\Delta_{jx}}{\Delta_j}, \qquad v_{jy} = \frac{\Delta_{jy}}{\Delta_j}, \qquad v_{jz} = \frac{\Delta_{jz}}{\Delta_j}, \tag{2.22}$$

where the coefficient determinant of the matrix in Eq. (2.21) is

$$\Delta_j = \omega^3 - \omega^2 a_j - \omega_{\mathrm{c}j}^2(\omega - a_j \cos^2\theta), \tag{2.23}$$

and Δ_{jx}, Δ_{jy} and Δ_{jz} are the corresponding sub-determinants,

$$\begin{aligned}
\Delta_{jx} &= i\frac{q_j}{m_j}[\omega(\omega - a_j^2\cos^2\theta)E_x + i\omega_{\mathrm{c}j}(\omega - a_j\cos^2\theta)E_y \\
&\qquad + a_j\,\omega\sin\theta\cos\theta E_z] \qquad (2.24)\\
\Delta_{jy} &= i\frac{q_j}{m_j}[-i\omega_{\mathrm{c}j}(\omega - a_j\cos^2\theta)E_x + \omega(\omega - a_j)E_y \\
&\qquad - i\,a_j\,\omega_{\mathrm{c}j}\sin\theta\cos\theta E_z] \qquad (2.25)\\
\Delta_{jz} &= i\frac{q_j}{m_j}[a_j\sin\theta\cos\theta(\omega E_x + i\omega_{\mathrm{c}j}E_y) \\
&\qquad + (\omega(\omega - a_j\sin^2\theta) - \omega_{\mathrm{c}j}^2)E_z] \qquad (2.26)
\end{aligned}$$

Equivalently, written by components Eq. (2.20) becomes

$$\begin{pmatrix} n^2\cos^2\theta - 1 & 0 & -n^2\sin\theta\cos\theta \\ 0 & n^2 - 1 & 0 \\ -n^2\sin\theta\cos\theta & 0 & n^2\sin^2\theta - 1 \end{pmatrix} \begin{pmatrix} E_x \\ E_y \\ E_z \end{pmatrix} = i\frac{4\pi}{\omega}\sum_j q_j N_{j0} \begin{pmatrix} v_{jx} \\ v_{jy} \\ v_{jz} \end{pmatrix} \tag{2.27}$$

where $n = k\,c/\omega$ is the **index of refraction**. In order to derive the dielectric tensor, one needs first to express the velocity components via the electric field components (using the relations (2.22)) and to substitute them in the Eq. (2.27). Thus, the following tensor relation is obtained:

$$\underline{\underline{t}} \cdot \mathbf{E} = 0, \tag{2.28}$$

where the tensor $\underline{\underline{t}}$ has the form

$$\underline{\underline{t}} = \begin{pmatrix} n^2\,\cos^2\theta - \varepsilon_1 & i\,\varepsilon_4 & -(n^2 - \varepsilon_5)\,\sin\theta\cos\theta \\ -i\,\varepsilon_4 & n^2 - \varepsilon_2 & -i\,\varepsilon_6\,\sin\theta\cos\theta \\ -(n^2 - \varepsilon_5)\,\sin\theta\cos\theta & i\,\varepsilon_6\,\sin\theta\cos\theta & n^2\,\sin^2\theta - \varepsilon_3 \end{pmatrix} \tag{2.29}$$

and

$$\varepsilon_1 = 1 - \sum_j \frac{\omega_{\mathrm{p}j}^2}{\Delta_j} (\omega - a_j \cos^2\theta) \tag{2.30}$$

$$\varepsilon_2 = 1 - \sum_j \frac{\omega_{\mathrm{p}j}^2}{\Delta_j} (\omega - a_j) \tag{2.31}$$

$$\varepsilon_3 = 1 - \sum_j \frac{\omega_{\mathrm{p}j}^2}{\Delta_j} \left[(\omega - a_j \sin^2\theta) - \frac{\omega_{\mathrm{c}j}^2}{\omega} \right] \tag{2.32}$$

$$\varepsilon_4 = \sum_j \frac{\omega_{\mathrm{p}j}^2}{\Delta_j} \frac{\omega_{\mathrm{c}j}}{\omega} (\omega - a_j \cos^2\theta) \tag{2.33}$$

$$\varepsilon_5 = \sum_j \frac{\omega_{\mathrm{p}j}^2}{\Delta_j} a_j \tag{2.34}$$

$$\varepsilon_6 = \sum_j \frac{\omega_{\mathrm{p}j}^2}{\Delta_j} a_j \frac{\omega_{\mathrm{c}j}}{\omega} \tag{2.35}$$

The zeros of the determinant of the tensor (2.29) gives the dispersion relation for the wave modes propagating in this plasma configuration,

$$D(\omega, \mathbf{k}) = \mathrm{Det}\, \underline{\underline{t}} = 0. \tag{2.36}$$

The finite number of discrete solutions of Eq. (2.36) describes the propagation of linear waves with frequency $\omega = \omega(\mathbf{k})$. The full treatment of the linear wave analysis (i.e., dispersion relation and polarization) in a multi-ion plasma is given in the work by [56]. Because the general case is not easy to handle, it is focused only on the cases that are needed in this thesis.

2.3.1 Cold plasma approximation

In this case $a_j = 0$, and $\Delta_j = \omega(\omega^2 - \omega_{\mathrm{c}j}^2)$, so the system (2.30)–(2.35) reduces to

$$\varepsilon_1 = \varepsilon_2 = 1 - \sum_j \frac{\omega_{\mathrm{p}j}^2}{\omega^2 - \omega_{\mathrm{c}j}^2} \tag{2.37}$$

$$\varepsilon_3 = 1 - \sum_j \frac{\omega_{\mathrm{p}j}^2}{\omega^2} \tag{2.38}$$

$$\varepsilon_4 = \sum_j \frac{\omega_{\mathrm{p}j}^2}{\omega^2 - \omega_{\mathrm{c}j}^2} \frac{\omega_{\mathrm{c}j}}{\omega} \tag{2.39}$$

$$\varepsilon_5 = \varepsilon_6 = 0 \tag{2.40}$$

In the case of a pure electron–proton plasma (because the corona consists predominantly from electrons and protons), from the above components of the plasma dielectric tensor one

can recover the expressions in [9], namely,

$$\varepsilon_1 = 1 - \frac{\omega_{\rm pe}^2}{\omega^2 - \omega_{\rm ce}^2} - \frac{\omega_{\rm pi}^2}{\omega^2 - \omega_{\rm ci}^2} \tag{2.41}$$

$$\varepsilon_4 = -\frac{\omega_{\rm ce}}{\omega}\frac{\omega_{\rm pe}^2}{\omega^2 - \omega_{\rm ce}^2} + \frac{\omega_{\rm ci}}{\omega}\frac{\omega_{\rm pi}^2}{\omega^2 - \omega_{\rm ci}^2} \tag{2.42}$$

$$\varepsilon_3 = 1 - \frac{\omega_{\rm pe}^2}{\omega^2} - \frac{\omega_{\rm pi}^2}{\omega^2} \tag{2.43}$$

In order to obtain the dispersion relation for cold plasma waves, one needs to substitute the corresponding components of the cold dielectric tensor into Eq. (2.29) and to calculate the coefficient determinant. The result recovers the well-known *Appleton–Hartree equation*:

$$A\,n^4 - Bn^2 + C = 0, \tag{2.44}$$

where

$$\begin{aligned} A &= \varepsilon_3 \cos^2\theta + \varepsilon_1 \sin^2\theta \\ B &= \varepsilon_1\varepsilon_3\,(1 + \cos^2\theta) + (\varepsilon_1^2 - \varepsilon_4^2)\,\sin^2\theta \\ C &= \varepsilon_3\,(\varepsilon_1^2 - \varepsilon_4^2) \end{aligned}$$

The solution of Eq. (2.44) gives the dispersion relation for the cold plasma waves. From this general formula one can obtain the dispersion relations in the case of parallel, oblique, and perpendicular propagation, with respect to the ambient magnetic field. Here, the wave frequency and the wave number are normalized to $\omega_{\rm ce}$ and $\omega_{\rm pe}/c$, respectively, i.e., $\omega_0 = \omega_{\rm ce}$ and $L_0 = c/\omega_{\rm pe}$ (see Subsect. 2.2). Then the normalized quantities are:

$$n^2 = \frac{k'^2}{\omega'^2}\frac{\omega_{\rm pe}^2}{\omega_{\rm ce}^2} \tag{2.45}$$

$$\varepsilon_1' = 1 - \frac{\omega_{\rm pe}^2}{\omega_{\rm ce}^2}\left[\frac{1}{\omega'^2 - 1} + \frac{\mu_{\rm e}}{\omega'^2 - \mu_{\rm e}^2}\right] \tag{2.46}$$

$$\varepsilon_3' = 1 - \frac{\omega_{\rm pe}^2}{\omega_{\rm ce}^2}\frac{1 + \mu_{\rm e}}{\omega'^2} \tag{2.47}$$

$$\varepsilon_4' = -\frac{\omega_{\rm pe}^2}{\omega_{\rm ce}^2}\left[\frac{1}{\omega'(\omega'^2 - 1)} - \frac{\mu_{\rm e}^2}{\omega'(\omega'^2 - \mu_{\rm e}^2)}\right] \tag{2.48}$$

Because for the most space plasma it is appropriate to assume $\omega_{\rm pe}^2/\omega_{\rm ce}^2 \gg 1$ (see Chapter 1, Table 1.1), one can neglect the unity in the expressions for ε_1' and ε_3'. Additionally, for the numerical solution of the dispersion relation (2.44), the frequency ratio is taken to be $\omega_{\rm pe}/\omega_{\rm ce} = 20$, that is the value for the 55-MHz level of the solar corona (see again Table 1.1).

Now, some important issues that affect the mode propagation need to be considered here, namely the so-called *cutoff* and *resonance* frequencies. A *cutoff* frequency occurs in plasma when the index of refraction goes to zero, $n \to 0$ (i.e., $k \to 0$) and equivalently the wavelength becomes infinite, $\lambda \to \infty$. The opposite is valid in the case of a *resonance*, namely

$k \to \infty$ and $\lambda \to 0$. From the available literature on plasma waves, here [9] is followed, so the following definitions are adopted:

$$\omega_{\mathrm{R,co}} = \frac{1}{2}\left[(\omega_{\mathrm{ce}}^2 + 4\,\omega_{\mathrm{pe}}^2)^{1/2} + \omega_{\mathrm{ce}}\right] \tag{2.49}$$

$$\omega_{\mathrm{L,co}} = \frac{1}{2}\left[(\omega_{\mathrm{ce}}^2 + 4\,\omega_{\mathrm{pe}}^2)^{1/2} - \omega_{\mathrm{ce}}\right] \tag{2.50}$$

for the right- and heft-hand cutoff frequencies, respectively, and also

$$\omega_{\mathrm{UH,res}} = \sqrt{\omega_{\mathrm{ce}}^2 + \omega_{\mathrm{pe}}^2} \tag{2.51}$$

$$\omega_{\mathrm{LH,res}} = \omega_{\mathrm{ce}}\,\omega_{\mathrm{ci}} \tag{2.52}$$

for the upper and lower hybrid resonance frequencies, respectively. Because the computed plots[2] use normalized parameters, all frequencies are normalized to ω_{ce}, e.g., $\omega' = \omega/\omega_{\mathrm{ce}}$, and the wave number is normalized in such a manner that $k' = k\,c/\omega_{\mathrm{pe}}$, where the primed values are dimensionless. Hence, Eqs. (2.49)–(2.52) become correspondingly,

$$\omega'_{\mathrm{R,co}} = \frac{1}{2}\left[(1 + 4\,S^2)^{1/2} + 1\right] = 20.506 \tag{2.53}$$

$$\omega'_{\mathrm{L,co}} = \frac{1}{2}\left[(1 + 4\,S^2)^{1/2} - 1\right] = 19.506 \tag{2.54}$$

$$\omega'_{\mathrm{UH}} = (1 + S^2)^{1/2} = 20.025 \tag{2.55}$$

$$\omega'_{\mathrm{LH}} = \mu_{\mathrm{e}}^{1/2} = 0.0233 \tag{2.56}$$

where their numerical values are also given and $S = \omega_{\mathrm{pe}}/\omega_{\mathrm{ce}} = 20$. Each of them determines a so-called 'asymptotic', that is depicted with a dashed line on the corresponding plots, Figs. 2.2–2.9, and for completeness also

$$\omega' = 1 \quad \Longrightarrow \quad \omega = \omega_{\mathrm{ce}} \tag{2.57}$$

$$\omega' = \mu_{\mathrm{e}} = 0.00054 \quad \Longrightarrow \quad \omega = \omega_{\mathrm{ci}} \tag{2.58}$$

$$\omega' = S = 20 \quad \Longrightarrow \quad \omega = \omega_{\mathrm{pe}} \tag{2.59}$$

are explicitely given in these figures. Henceforth, the dispersion of the plasma waves, in the case for parallel and perpendicular propagation with respect to the ambient magnetic field, is discussed. In particular, it is focused on those modes, that are needed in the forthcoming Chapters.

Parallel wave propagation

Initially $\theta = 0°$ is discussed, so in this case the waves propagate along the ambient magnetic field. Then, $A = \varepsilon_3$, $B = 2\,\varepsilon_1\,\varepsilon_3$, and $C = \varepsilon_3(\varepsilon_1^2 - \varepsilon_4^2)$ and the solution of the dispersion relation (2.44) reduces to:

$$n_{\mathrm{R,L}}^2 = \varepsilon'_1 \pm \varepsilon'_4, \tag{2.60}$$

[2] All plots in the present Chapter were computed with the *Mathematica* software package.

where the subscripts R and L denote the right- and left-hand side polarized wave, obtained when one consider the positive or the negative sign, respectively. After substituting the normalized components of the cold dielectric tensor, one obtains for $S \gg 1$

$$\frac{k'^2}{\omega'^2_{\mathrm{R,L}}} = \frac{\pm 1}{\omega'(1 \mp \omega')} - \frac{\mu_{\mathrm{e}}}{\omega'(\omega' \pm \mu_{\mathrm{e}})}. \tag{2.61}$$

These modes correspond to the right-hand circularly polarized whistler wave and the left-hand circularly polarized Alfvén wave. The resonance frequencies are at the electron ($\omega' = 1$) and proton ($\omega' = \mu_{\mathrm{e}}$) cyclotron frequencies. In the case of electron dominated component, the second term can be neglected, resulting for the upper branch of the right-hand polarized wave in the *whistler dispersion relation*,

$$k'_{\mathrm{wh}} = \sqrt{\frac{\omega'_{\mathrm{R}}}{1 - \omega'_{\mathrm{R}}}}, \tag{2.62}$$

as completely plotted on Fig. 2.2. In the short wavelength limit (large k) the mode tends to ω_{ce}. Introducing back the dimensions into the formula above, one recovers the well-known relation for whistler waves,

$$k_{\mathrm{wh}} = \frac{\omega_{\mathrm{pe}}}{c}\sqrt{\frac{\omega}{\omega_{\mathrm{ce}} - \omega}}. \tag{2.63}$$

In the long wavelength limit, i.e., $k \to 0$, Eq. (2.61) provides

$$\omega = \sqrt{\mu_{\mathrm{e}}}\, k \left(1 \pm \frac{k}{2\sqrt{\mu_{\mathrm{e}}}}\right), \tag{2.64}$$

where the upper and lower sign stands for the right- and left-hand circularly polarized mode, respectively. Thus, in the long wavelength limit, the phase velocity of the whistler wave is the Alfvén speed. Another solution of the dispersion relation (2.60) appears in the very long wavelength limit. This is the well-known *Alfvén wave*, plotted on Fig. 2.3, that tends to ω_{ci} with increasing of the wave number. The other two solutions are the *left* and the

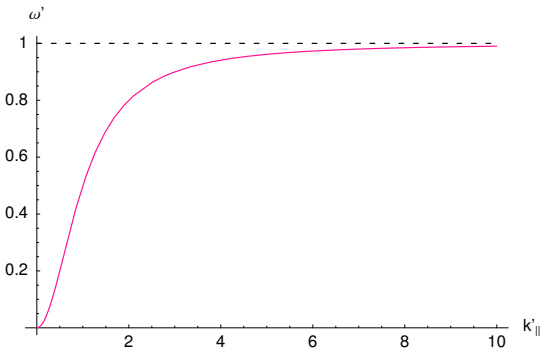

Figure 2.2: Whistler dispersion relation.

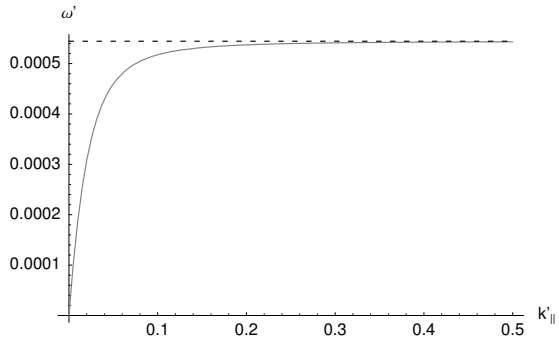

Figure 2.3: Dispersion of the Alfvén wave.

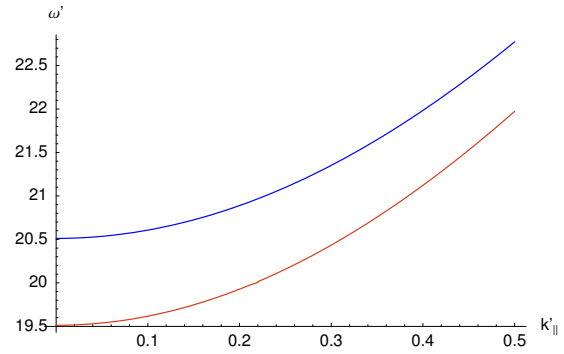

Figure 2.4: Left (red) and right (blue) hand polarized waves for $\theta = 0°$.

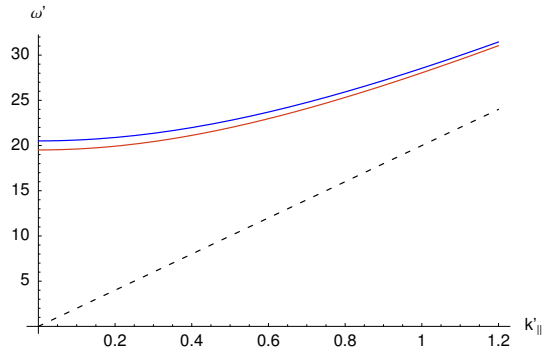

Figure 2.5: L and R modes from Fig 2.4. The dashed line is the light wave, $\omega' = S\,k'$.

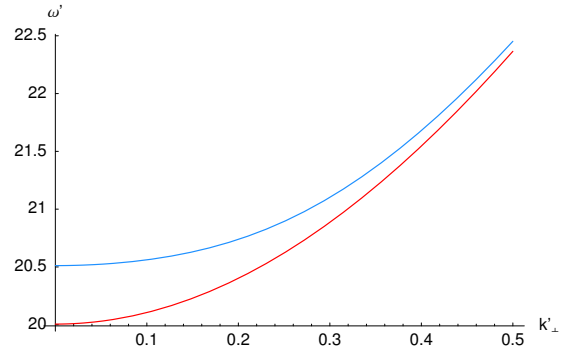

Figure 2.6: Ordinary (red) and extraordinary (blue) waves for $\theta = 90°$.

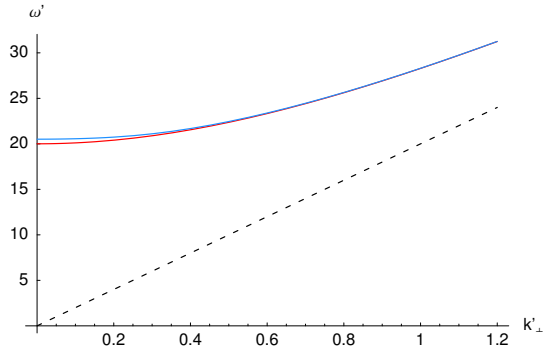

Figure 2.7: O and X modes from Fig. 2.6. The dashed line is the light wave, $\omega' = S\,k'$.

(upper branch of the) *right-hand polarized, high frequency electromagnetic waves*, plotted together on Fig. 2.4. At large k, both modes approach the light wave mode, $\omega = c\,k$, see Fig. 2.5.
In order to recover the dimensions for the frequency and the wave number, one needs to multiply the normalized quantities, as given on the plots, by $\omega_{ce} = 1.76 \times 10^7\,\mathrm{s}^{-1}$ and the inverse of $c/\omega_{pe} = 87\,\mathrm{cm}$, respectively (see Table 1.1 for the 55 MHz plasma).

Perpendicular wave propagation

In the perpendicular case, $\theta = 90°$, $A = \varepsilon_1$, $B = \varepsilon_1\,\varepsilon_3 + (\varepsilon_1^2 - \varepsilon_4^2)$, and $C = \varepsilon_3(\varepsilon_1^2 - \varepsilon_4^2)$ that are set in the relation (2.44), so one obtains,

$$n_{\mathrm{O}}^2 = \varepsilon_3' \qquad \text{and} \qquad n_{\mathrm{X}}^2 = \frac{\varepsilon_1'^2 - \varepsilon_3'^2}{\varepsilon_1'}$$

taking the positive or the negative sign while solving the Appleton–Hartree equation, respectively. In this case, the positive and the negative sign are usually named *ordinary* (O) and *extraordinary* (X) mode, correspondingly, and are plotted both on Fig. 2.6. The

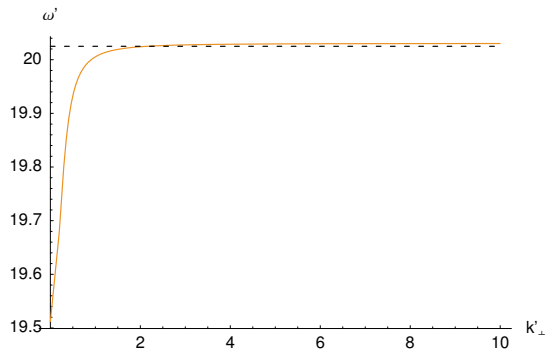

Figure 2.8: Upper hybrid mode.

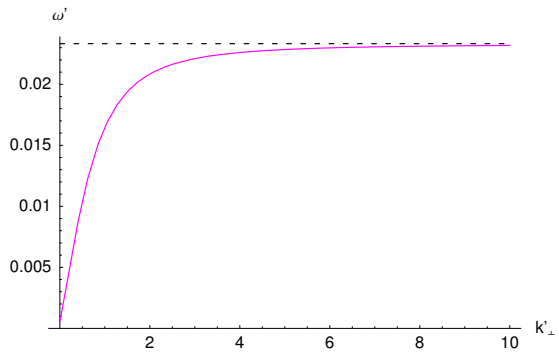

Figure 2.9: Lower hybrid mode.

O-mode has a cut-off frequency at $\omega_{\rm pe}$, whereas the cut-off frequency of the X-mode is at $\omega_{\rm R,co}$, or in normalized quantities, $\omega' = 20$ and 20.506, respectively. At shorter wavelengths both modes approach the asymptotic, defined by the light waves (i.e., $\omega = c\,k$), as shown on Fig. 2.7, similarly to the R- and L-modes in the parallel case, see Fig. 2.5.
The other two roots of the dispersion relation in the perpendicular case, are the so-called *upper* and *lower hybrid mode*, plotted on Fig. 2.8 and Fig. 2.9, respectively. As denoted by their name, the mode has an asymptotic at $\omega_{\rm UH}$ (the horizontal dashed line at 20.025 on Fig. 2.8) or at $\omega_{\rm LH}$ (the 0.0233-level line on Fig. 2.9), correspondingly. Their cut-off frequencies are at $\omega'_{\rm L,co} = 19.506$ and 0, respectively, as seen on Figs. 2.8 and 2.9.

2.3.2 Waves in an unmagnetized plasma

In this case $\omega_{\rm ci} = 0$, $\Delta_j = \omega^2(\omega - a_j)$ and the angle $\theta = \angle(\mathbf{k}, \mathbf{B}_0)$ looses its sense. Additionally, here it is assumed cold protons (i.e. $a_{\rm p} = 0$) and warm electrons (i.e. $a_{\rm e} = \gamma v_{\rm th,e}^2 k^2/\omega$). Hence, one obtains,

$$\varepsilon_3 = 1 - \frac{\omega_{\rm pi}^2}{\omega^2} - \frac{\omega_{\rm pe}^2}{\omega^2 - \gamma v_{\rm th,e}^2 k^2}.$$

When it is normalized to $\omega_0 = \omega_{\rm pe}$ and $L_0 = v_{\rm th,e}/\omega_{\rm pe}$, it leads to

$$\varepsilon'_3 = 1 - \frac{\mu_{\rm e}}{\omega'^2} - \frac{1}{\omega'^2 - \gamma k'^2}.$$

In the case of pure electrostatic waves, the dispersion relation reduces to $\varepsilon'_3 = 0$, see Eq. (2.28) and (2.29), or finally:

$$\omega'^4 - (\gamma k'^2 + \mu_{\rm e} + 1)\omega'^2 + \gamma k'^2 \mu_{\rm e} = 0. \tag{2.65}$$

In the high frequency limit one gets the dispersion relation for *Langmuir waves*,

$$\omega' = \sqrt{1 + \gamma k'^2}, \tag{2.66}$$

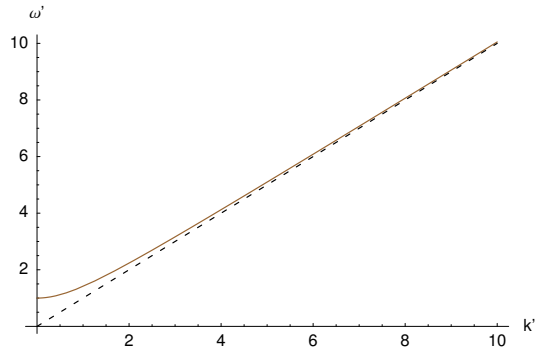

Figure 2.10: Langmuir wave dispersion relation.

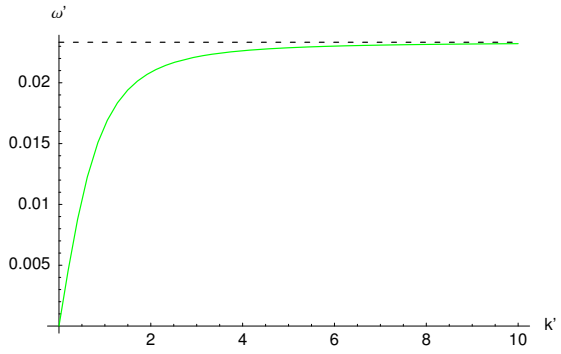

Figure 2.11: Sound (ion-acoustic) wave dispersion relation.

or

$$\omega = \sqrt{\omega_{\rm pe}^2 + \gamma v_{\rm th,e}^2 \, k^2}, \tag{2.67}$$

see Fig. 2.10. The low frequency limit of Eq. (2.65) provides the *ion-acoustic waves*, plotted on Fig. 2.11,

$$\omega' = \sqrt{\mu_{\rm e}} \frac{k'}{\sqrt{1 + k'^2}}, \tag{2.68}$$

or in the limit $k'^2 \ll 1$ one gets

$$\omega' = k' \sqrt{\mu_{\rm e}} \qquad \text{or} \qquad \frac{\omega}{k} = \sqrt{\frac{k_{\rm B} T_{\rm e}}{m_{\rm i}}} = c_{\rm se}, \tag{2.69}$$

where $c_{\rm se}$ is the ion-acoustic speed. This mode approach the $\omega_{\rm pi}$ level at short wavelengths, as shown by the dashed line on Fig. 2.11. Due to the different normalization, in this Subsection, $\omega' = 1$ corresponds to the electron plasma frequency, $\omega_{\rm pe}$, and $\omega' = 0.0233$ (because $\omega_{\rm pi}/\omega_{\rm pe} = \mu_{\rm e}^{1/2} = 0.0233$), corresponds the ion plasma frequency, $\omega_{\rm pi}$.

This Chapter represents an overview on the multi-fluid theory, together with the used normalization (different in each of the subsequent three Chapters), the general procedure of the linearization analysis and a summary of the existing wave modes in the case of a cold plasma approximation. The multi-fluid equations are the staring point for the theoretical and numerical results, presented in Chapter 3 and 5. In the case of Chapter 4, however, only the more appropriate for this particular case kinetic approach is presented in the dissertation (for the multi-fluid treatment see [67, 68]).

Chapter 3

Nonlinear solution of the Sakai–Sonnerup system

3.1 Introduction

Large-amplitude magnetic field fluctuations are often observed by in-situ measurements in space, e.g., at the Earth's bow shock [79, 35, 61, 62], other planetary bow shocks [23, 33, 25], in the vicinity of comets [87, 114, 112], and at co-rotating interaction regions (CIRs) [113]. In general, all these wave phenomena are thought to be generated by energetic particles produced at the related shocks [79]. That is also confirmed by numerical simulations [1, 91].

For illustration, three examples of such magnetic field fluctuations are presented here, namely:

- The so-called low frequency upstream waves (Fig. 3.1) appear in the upstream region of Earth's bow shock, for instance. Dual spacecraft measurements [34] reveal that they have typical frequencies of 0.1 of the proton cyclotron frequency and amplitudes in the magnetic field fluctuations of 0.3 of the undisturbed magnetic field [61]. They are correlated with density fluctuations [79] and are predominantly right-hand circularly polarized in the plasma rest frame, i.e., they have been classified as fast magnetosonic waves.

- Since the above mentioned waves are compressive ones, they steepen into so-called shocklets, which are attached by magnetic field fluctuations with a higher frequency of about 10 times the frequency of the upstream waves [61] (Fig. 3.2). The dual spacecraft observations reveal that these are large amplitude whistler waves with frequencies well above the proton cyclotron frequency [34].

- These upstream waves can steepen into very large-amplitude wave phenomena, the so-called SLAMS (short large-amplitude magnetic field structures), if they approach to the shock (Fig. 3.3) [92, 62]. They show magnetic field compression by a typical factor of about three and are also accompanied with density compression.

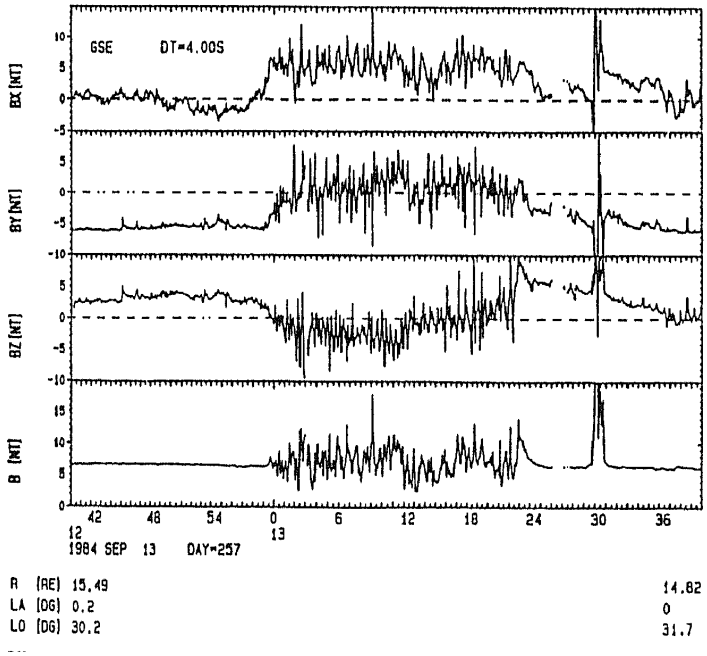

Figure 3.1: Magnetic field fluctuations during an upstream wave event, from [61].

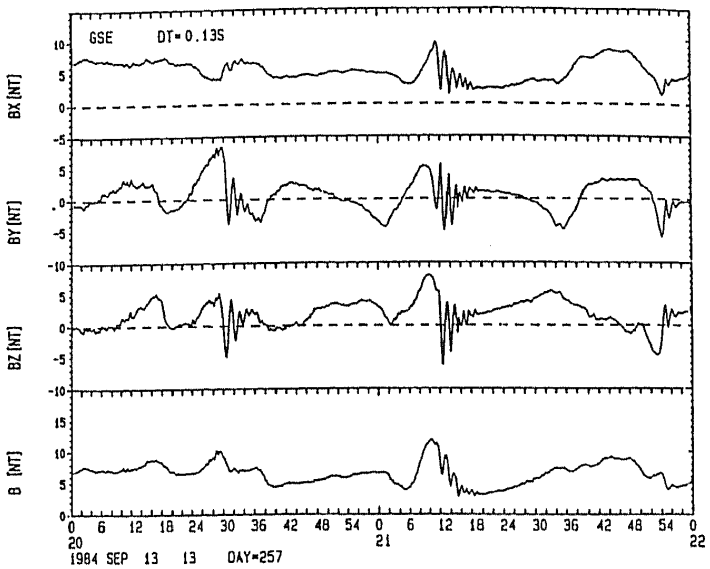

Figure 3.2: Discrete whistler wave packets embedded in steepened upstream waves, see Fig. 3.1, from [61].

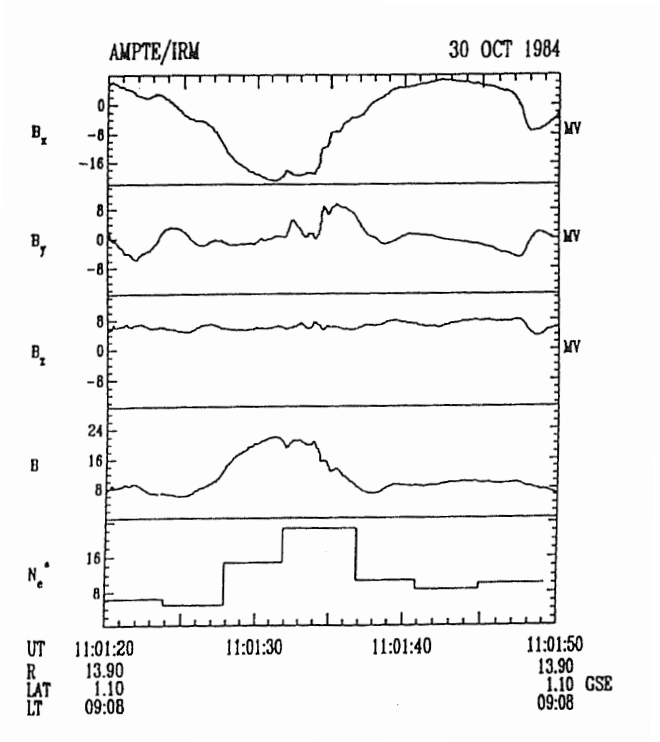

Figure 3.3: Magnetic field components, total B-field and electron number density (from top to bottom) in SLAMS, from [62].

All these phenomena seem to be closely related to each other and play an important role of the dynamic of the associated shock [92, 89].

These observations motivated us to study the nonlinear behaviour of low frequency plasma waves. But, it is basically not intended to present an explanation of these wave phenomena in this dissertation. Since the frequency scale of these fluctuations is very much smaller than the electron plasma and electron cyclotron frequency, these phenomena are predominantly carried by the ions, whereas the electrons act as a neutralizing fluid. That allows to simplify the multi-fluid equations by assuming a pure electron–proton plasma (i.e., two-fluid equations) with neglecting the displacement current and the electron mass. Since the amplitude of the observed magnetic field fluctuations may be large (sometimes up to few times the magnitude of the undisturbed ambient magnetic field), a fully nonlinear description of the two-fluid equations is necessary, i.e., nonlinear terms cannot be neglected.

3.2 Derivation of the Sakai–Sonnerup system

The system of equations used here for describing the plasma state, was initially presented in the work by Sakai and Sonnerup, see [88]. The procedure for obtaining the so-called **Sakai–Sonnerup system**, that follows naturally from the system of multi-fluid equations

(as introduced in Chapter 2), is explained in the present Section. The displacement currents are neglected, an isotropic and diagonal pressure tensors for the electrons ($j = \mathrm{e}$) and the protons ($j = \mathrm{i}$) are assumed, and finally a quasi-neutral plasma state is considered, i.e.,

$$N_\mathrm{e} = N_\mathrm{i} = N. \tag{3.1}$$

Additionally, quasi-neutrality means the following assumptions [37]:

$$\lambda_\mathrm{D} \ll L; \quad \omega \ll \omega_\mathrm{ce}; \quad \omega \ll \omega_\mathrm{pe}; \quad \omega \ll \omega_\mathrm{pi}: \quad \frac{\omega}{\omega_\mathrm{ci}} \ll \frac{c}{v_\mathrm{A}}, \quad \frac{\omega^2}{\omega_\mathrm{pe}^2}\frac{m_\mathrm{i}+m_\mathrm{e}}{m_\mathrm{e}} \ll 1,$$

where L is some characteristic length for the system, i.e., the wavelength. Thus, the general set of multi-fluid equations, i.e., Eqs. (2.1)–(2.6), reduces to:

$$\frac{\partial N}{\partial t} + \nabla \cdot (N\mathbf{v}_\mathrm{e}) = 0 \tag{3.2}$$

$$\frac{\partial N}{\partial t} + \nabla \cdot (N\mathbf{v}_\mathrm{i}) = 0 \tag{3.3}$$

$$\frac{\mathrm{d}^{(\mathrm{e})}}{\mathrm{d}t}\mathbf{v}_\mathrm{e} = -\Gamma \frac{V_\mathrm{Te}^2}{N}\nabla N - \frac{e}{m_\mathrm{e}}\left[\mathbf{E} + \frac{1}{c}(\mathbf{v}_\mathrm{e} \times \mathbf{B})\right] \tag{3.4}$$

$$\frac{\mathrm{d}^{(\mathrm{i})}}{\mathrm{d}t}\mathbf{v}_\mathrm{i} = -\Gamma \frac{V_\mathrm{Ti}^2}{N}\nabla N + \frac{e}{m_\mathrm{i}}\left[\mathbf{E} + \frac{1}{c}(\mathbf{v}_\mathrm{i} \times \mathbf{B})\right] \tag{3.5}$$

$$\nabla \times \mathbf{B} = \frac{4\pi e}{c} N(\mathbf{v}_\mathrm{i} - \mathbf{v}_\mathrm{e}) \tag{3.6}$$

with the convective derivative for electrons and protons defined correspondingly as,

$$\frac{\mathrm{d}^{(\mathrm{e,i})}}{\mathrm{d}t} = \frac{\partial}{\partial t} + \mathbf{v}_\mathrm{e,i} \cdot \nabla \tag{3.7}$$

and $\Gamma = \gamma\,(N/N_0)^{(\gamma-1)}$, with γ as the ratio of specific heats (see Eq. (2.8) in Chapter 2). As next, the electron fluid velocity $\mathbf{v}_\mathrm{e}$ and the electric field have to be removed. Starting from Eq. (3.6), one gets the $\mathbf{v}_\mathrm{e}$ as:

$$\mathbf{v}_\mathrm{e} = \mathbf{v}_\mathrm{i} - \frac{c}{4\pi e N}\nabla \times \mathbf{B}. \tag{3.8}$$

The electric field $\mathbf{E}$ can be expressed from Eq. (3.4), as

$$\mathbf{E} = -\frac{m_\mathrm{e}}{e}\frac{\mathrm{d}^{(\mathrm{e})}}{\mathrm{d}t}\mathbf{v}_\mathrm{e} - \Gamma \frac{m_\mathrm{e}}{e}\frac{V_\mathrm{Te}^2}{N}\nabla N - \frac{1}{c}(\mathbf{v}_\mathrm{e} \times \mathbf{B}), \tag{3.9}$$

which, together with the expression for the electron velocity (3.8), can be substituted in the Faraday law, Eq. (2.5), in order to get a relation between the ion velocity and the magnetic field, that finally reads as,

$$\begin{aligned}\frac{\partial \mathbf{B}}{\partial t} = &- \frac{c^2 m_\mathrm{e}}{4\pi e^2}\nabla \times \left[\frac{1}{N}\frac{\mathrm{d}^{(\mathrm{e})}}{\mathrm{d}t}(\nabla \times \mathbf{B})\right] + \frac{m_\mathrm{e} c}{e}\nabla \times \left[\frac{\mathrm{d}^{(\mathrm{e})}}{\mathrm{d}t}\mathbf{v}_\mathrm{i}\right] \\ &- \frac{c}{4\pi e}\nabla \times \left[\frac{1}{N}(\nabla \times \mathbf{B}) \times \mathbf{B}\right] + \nabla \times (\mathbf{v}_\mathrm{i} \times \mathbf{B}).\end{aligned} \tag{3.10}$$

Next, one can multiply Eq. (3.4) with m_e and Eq. (3.5) with m_i and add these two equations, that finally, using Eq. (3.8) for the $\mathbf{v}_\mathrm{e}$, becomes,

$$\begin{aligned} m_\mathrm{i}\frac{\mathrm{d}^{(\mathrm{i})}}{\mathrm{d}t}\mathbf{v}_\mathrm{i} \quad &+ \quad m_\mathrm{e}\frac{\mathrm{d}^{(\mathrm{e})}}{\mathrm{d}t}\mathbf{v}_\mathrm{i} - m_\mathrm{e}\frac{c}{4\pi eN}\frac{\mathrm{d}^{(\mathrm{e})}}{\mathrm{d}t}\nabla\times\mathbf{B} = -\Gamma\left(m_\mathrm{e}V_\mathrm{Te}^2 + m_\mathrm{i}V_\mathrm{Ti}^2\right)\frac{\nabla N}{N} \\ &+ \quad \frac{1}{4\pi N}(\nabla\times\mathbf{B})\times\mathbf{B}. \end{aligned} \tag{3.11}$$

This intermediate step is justified if the center of mass velocity $\mathbf{v}$ is introduced, that is,

$$\mathbf{v} = \frac{m_\mathrm{i}\mathbf{v}_\mathrm{i} + m_\mathrm{e}\mathbf{v}_\mathrm{e}}{m_\mathrm{i}+m_\mathrm{e}} \tag{3.12}$$

and thus is possible to reduce Eq. (3.11) even further, until it obtains the following form,

$$\begin{aligned} \left[\frac{m_\mathrm{i}}{m_\mathrm{i}+m_\mathrm{e}}\frac{\mathrm{d}^{(\mathrm{i})}}{\mathrm{d}t} + \frac{m_\mathrm{e}}{m_\mathrm{i}+m_\mathrm{e}}\frac{\mathrm{d}^{(\mathrm{e})}}{\mathrm{d}t}\right]\mathbf{v} \quad &- \quad \frac{m_\mathrm{e}}{m_\mathrm{i}+m_\mathrm{e}}\frac{c}{4\pi e}\frac{\mathrm{d}^{(\mathrm{e})}}{\mathrm{d}t}\frac{\nabla\times\mathbf{B}}{N} = -\Gamma\frac{m_\mathrm{e}V_\mathrm{Te}^2 + m_\mathrm{i}V_\mathrm{Ti}^2}{m_\mathrm{i}+m_\mathrm{e}}\frac{\nabla N}{N} \\ &+ \quad \frac{1}{4\pi(m_\mathrm{i}+m_\mathrm{e})}\frac{(\nabla\times\mathbf{B})\times\mathbf{B}}{N} \end{aligned} \tag{3.13}$$

with

$$\frac{\mathrm{d}^{(\mathrm{e})}}{\mathrm{d}t} = \frac{\mathrm{d}^{(\mathrm{i})}}{\mathrm{d}t} - \frac{c}{4\pi eN}(\nabla\times\mathbf{B})\cdot\nabla \tag{3.14}$$

that is deduced from Eq. (3.7) for the ion part, where $\mathbf{v}_\mathrm{i}$ is taken from Eq. (3.8). Finally, $\mathbf{v}_\mathrm{e}$ taken from Eq. (3.12) is substituted in Eq. (3.8), in order to obtain an expression for $\mathbf{v}_\mathrm{i}$ where $\mathbf{v}_\mathrm{e}$ is canceled out, i.e.,

$$\mathbf{v}_\mathrm{i} = \mathbf{v} + \frac{c}{4\pi eN}\frac{m_\mathrm{e}}{m_\mathrm{i}+m_\mathrm{e}}(\nabla\times\mathbf{B}). \tag{3.15}$$

In summary, the electron fluid velocity and the electric field have been removed in favour of the center of mass velocity by the presented procedure.

3.2.1 Normalization

Now, the normalization of the physical quantities is performed here, as was introduced in Chapter 2, Sect. 2.2. Namely, all physical quantities can be expressed as a normalized value (denoted with primes) multiplied by some characteristic one for the given plasma state (that is also carrying the dimension), i.e.,

$$\begin{aligned} &\mathbf{B} = \mathbf{B}'B_0; \quad N = N'N_{\mathrm{e}0}; \quad \mathbf{v} = \mathbf{v}'v_\mathrm{A}; \quad \mathbf{v}_\mathrm{i} = \mathbf{v}_\mathrm{i}'v_\mathrm{A} \\ &t = t'T; \quad \nabla = L^{-1}\nabla'; \quad \frac{\mathrm{d}^{(\mathrm{e})}}{\mathrm{d}t} = T^{-1}\frac{\mathrm{d}^{(\mathrm{e})}}{\mathrm{d}t'}, \end{aligned} \tag{3.16}$$

where

$$L = \frac{c}{\omega_\mathrm{pi}} \equiv \frac{v_\mathrm{A}}{\omega_\mathrm{ci}}; \quad T = \omega_\mathrm{ci}^{-1}; \quad \frac{L}{T} \equiv v_\mathrm{A}; \quad v_\mathrm{A} = \frac{B_0}{\sqrt{4\pi(m_\mathrm{i}+m_\mathrm{e})N_{\mathrm{e}0}}}.$$

The normalized ion velocity from Eq.(3.15) becomes,

$$\mathbf{v}_{\mathrm{i}}' = \mathbf{v}' + \frac{\mu_{\mathrm{e}}}{N'}\,\nabla' \times \mathbf{B}' \tag{3.17}$$

with $\mu_{\mathrm{e}} = m_{\mathrm{e}}/m_{\mathrm{i}}$ as already defined in Chapter 2 and Eq. (3.14) reduces to

$$\frac{\mathrm{d}^{(\mathrm{e})}}{\mathrm{d}t'} = \frac{\mathrm{d}^{(\mathrm{i})}}{\mathrm{d}t'} - \frac{1+\mu_{\mathrm{e}}}{N'}(\nabla' \times \mathbf{B}') \cdot \nabla' \tag{3.18}$$

in normalized form. Eqs. (3.3), (3.10) and (3.13) are normalized according to (3.16), and additionally, the limit $\mu_{\mathrm{e}} \to 0$ is performed, so finally the following relations are obtained:

$$\frac{\partial N'}{\partial t'} + \nabla' \cdot (N'\mathbf{v}') = 0, \tag{3.19}$$

$$\frac{\partial \mathbf{v}'}{\partial t'} + (\mathbf{v}' \cdot \nabla')\mathbf{v}' = -\Gamma\,\beta_0\,\frac{\nabla' N'}{N'} + \frac{(\nabla' \times \mathbf{B}') \times \mathbf{B}'}{N'}, \tag{3.20}$$

$$\frac{\partial \mathbf{B}'}{\partial t'} - \nabla' \times (\mathbf{v}' \times \mathbf{B}') = -\nabla' \times \left[\frac{1}{N'}\left(\nabla \times \mathbf{B}'\right) \times \mathbf{B}'\right], \tag{3.21}$$

where $\beta_0 = 8\pi N_0 k_{\mathrm{B}} T/B^2$ and $\Gamma = \gamma N'^{(\gamma-1)}$ are dimensionless quantities. Thus the Eqs. (3.19)–(3.20) represent our basic equations, also called Hall-MHD equations [36].

3.2.2 Specifying the problem

The ambient magnetic field is assumed to lie in the x–z-plane and taking an angle θ to the x-axis, i.e., $\mathbf{B}_0 = B_0(\cos\theta, 0, \sin\theta)$. Additionally, all primes, denoting the dimensionless quantities, will be dropped henceforth. Here, all quantities are considered to depend only on x and t, i.e., the wave vector is aligned in the x-direction, then $\nabla \to \partial/\partial x$ and

$$\frac{\mathrm{d}}{\mathrm{d}t} = \frac{\partial}{\partial t} + v_x \frac{\partial}{\partial x}.$$

Then Eqs. (3.19)–(3.20), written by components, create a system of normalized equations, that is the so-called **Sakai–Sonnerup system** of equations, namely,

$$\frac{\partial N}{\partial t} + \frac{\partial}{\partial x}(N\,u) = 0 \tag{3.22}$$

$$\frac{\mathrm{d}u}{\mathrm{d}t} = -\Gamma\,\beta_0\,\frac{1}{N}\,\frac{\partial N}{\partial x} - \frac{1}{2N}\left[\frac{\partial}{\partial x}(B_y^2 + B_z^2)\right] \tag{3.23}$$

$$\frac{\mathrm{d}v_y}{\mathrm{d}t} = \frac{1}{N}\,B_x\,\frac{\partial B_y}{\partial t} \tag{3.24}$$

$$\frac{\mathrm{d}v_z}{\mathrm{d}t} = \frac{1}{N}\,B_x\,\frac{\partial B_z}{\partial t} \tag{3.25}$$

$$\frac{\mathrm{d}B_y}{\mathrm{d}t} = -B_y\,\frac{\partial u}{\partial x} + B_x\,\frac{\partial v_y}{\partial x} + \frac{\partial}{\partial x}\left(\frac{B_x}{N}\,\frac{\partial B_z}{\partial x}\right) \tag{3.26}$$

$$\frac{\mathrm{d}B_z}{\mathrm{d}t} = -B_z\,\frac{\partial u}{\partial x} + B_x\,\frac{\partial v_z}{\partial x} - \frac{\partial}{\partial x}\left(\frac{B_x}{N}\,\frac{\partial B_y}{\partial x}\right) \tag{3.27}$$

with $v_x \equiv u$. The Eqs. (3.22)–(3.27) represents our basic system of nonlinear equations, which need to be studied.

3.2.3 Linear case

In this Subsection, the usual linearization analysis is performed while assuming small amplitude waves. In this sense, the background/undisturbed state (denoted with subscript 0) can be presented in the following dimensionless form,

$$N_0 = 1, \qquad u_0 = v_{y0} = v_{z0} = 0, \qquad B_{x0} = \cos\theta, \qquad B_{y0} = 0, \qquad B_{z0} = \sin\theta. \tag{3.28}$$

In general, the dimensionless quantities can be expressed as a sum of the background and the perturbed ones, namely

$$N := 1 + n \tag{3.29}$$

$$u := u_1 \qquad v_y := v_{y1} \qquad v_z := v_{z1} \tag{3.30}$$

$$B_x := \cos\theta \qquad B_y := b_y \qquad B_z := b_z + \sin\theta. \tag{3.31}$$

Then, after substituting the above expressions for the plasma quantities in the Eqs. (3.22)–(3.27), the latter become a linearized system of equations, namely:

$$\frac{\partial n}{\partial t} + \frac{\partial u_1}{\partial x} = 0 \tag{3.32}$$

$$\frac{\partial u_1}{\partial t} = -\frac{\gamma\beta_0}{2}\frac{\partial n}{\partial x} - \sin\theta\,\frac{\partial b_z}{\partial x} \tag{3.33}$$

$$\frac{\partial v_{y1}}{\partial t} = \cos\theta\,\frac{\partial b_y}{\partial t} \tag{3.34}$$

$$\frac{\partial v_{z1}}{\partial t} = \cos\theta\,\frac{\partial b_z}{\partial t} \tag{3.35}$$

$$\frac{\partial b_y}{\partial t} = \cos\theta\,\frac{\partial v_{y1}}{\partial x} + \cos\theta\,\frac{\partial^2 b_z}{\partial x^2} \tag{3.36}$$

$$\frac{\partial b_z}{\partial t} = \cos\theta\,\frac{\partial v_{z1}}{\partial x} - \sin\theta\,\frac{\partial u_1}{\partial x} - \cos\theta\,\frac{\partial^2 b_y}{\partial x^2} \tag{3.37}$$

In the system above, one sets the perturbed values (n, u_1, v_{y1}, v_{z1}, b_x, b_y, b_z) to depend as $\propto \exp[i(kx - \omega t)]$, that implies $\partial/\partial t \to -i\omega$ and $\partial/\partial x \to i\,k$ (see for comparison Sect. 2.3). Performing such plane wave analysis leads to the following equations for the amplitudes:

$$n = \frac{k^2 \sin\theta}{\omega^2 - k^2\,\gamma\beta_0/2}\,b_z, \qquad u_1 = \frac{\omega}{k}\,n, \qquad v_{y1} = -\frac{k}{\omega}\,\cos\theta\,b_y, \qquad v_{z1} = -\frac{k}{\omega}\,\cos\theta\,b_z,$$

and after substituting them into Eqs. (3.36) and (3.37), a homogeneous system of equations is obtained. Its determinant provides the dispersion relation for this plasma state:

$$(\omega^2 - k^2\cos^2\theta)\left[(\omega^2 - k^2\cos^2\theta) - \frac{\omega^2 k^2 \sin^2\theta}{\omega^2 - k^2\,\gamma\beta_0/2}\right] - \omega^2 k^4 \cos^2\theta = 0. \tag{3.38}$$

The solutions of Eq. (3.38) give the dispersion relation for the different wave modes that occur in the case of such small wave approximation. The above dispersion relation is solved for four different angles, i.e., $\theta = 10°$, $40°$, $60°$, and $80°$. Only the positive part from all 6 modes is considered and these 3 modes are recognized as ion-cyclotron, sound and whistler mode, correspondingly plotted[1] on Fig. 3.4, Fig. 3.5 and Fig. 3.6.

[1] All plots in this Chapter were computed with the *Mathematica* software package

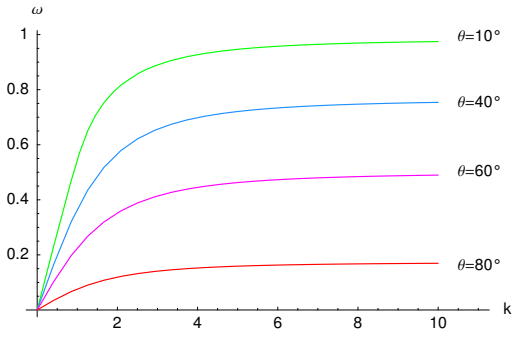

Figure 3.4: Plot of the ion-cyclotron mode of the dispersion relation (3.38) as function of θ.

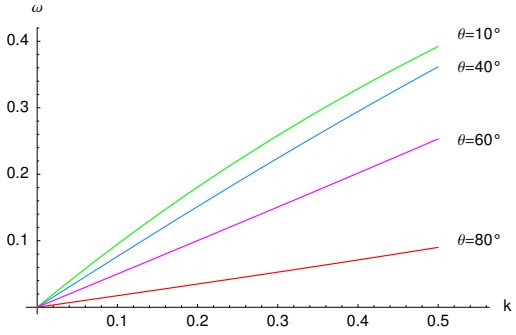

Figure 3.5: Plot of the sound mode of the dispersion relation (3.38) as a function of θ.

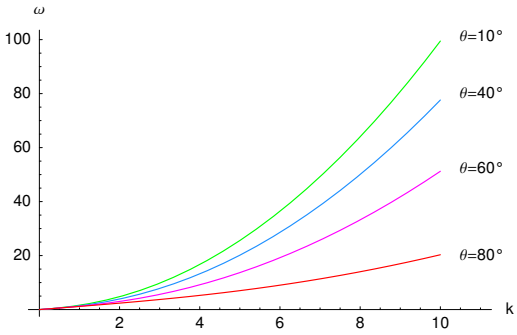

Figure 3.6: Plot of the whistler mode of the dispersion relation (3.38) as a function of θ.

3.3 Stationary solutions

When the amplitude of the wave is not small, the linearization analysis is no longer an appropriate description. Here, we search for stationary solutions of the Sakai–Sonnerup system (3.22)–(3.27), leading to solitary waves, for instance, [20, 108]. Because we look for

a stationary solution, all functions may be presented in the form:

$$\xi = x - Vt, \tag{3.39}$$

i.e., all varying quantities depend only from ξ and the new coordinate system is moving with the wave. Then, it is true that,

$$\frac{\partial}{\partial t} = -V\frac{\partial}{\partial \xi} \qquad \text{and} \qquad \frac{\partial}{\partial x} = \frac{\mathrm{d}}{\mathrm{d}\xi}. \tag{3.40}$$

The following 'four-step'-analysis is performed further on, starting with the first equation from the Sakai–Sonnerup system, Eq. (3.22). In the beginning, a change of the coordinate systems is done, namely the equation is re-written in a stationary system (moving with the same velocity V of the wave), or equivalently, the relations (3.40) are taken into account leading to,

$$-V\frac{\mathrm{d}N}{\mathrm{d}\xi} + \frac{\mathrm{d}(Nu)}{\mathrm{d}\xi} = 0. \tag{3.41}$$

After that, a spatial integration over ξ is performed,

$$-VN + Nu = C_1, \tag{3.42}$$

where the integration constant C_1 can be fixed by means of the conditions (3.28), which defines the undisturbed plasma state, as

$$C_1 = -V. \tag{3.43}$$

Then it is substituted it back into Eq. (3.42) and one finally gets,

$$u = V\left(1 - \frac{1}{N}\right). \tag{3.44}$$

Now, the same procedure is performed for Eq. (3.23), where one uses (3.31) for the components of the magnetic field. Then, Eq. (3.23) takes the form:

$$-V\,\frac{\mathrm{d}u}{\mathrm{d}\xi} = -\frac{\gamma\beta_0}{2}\,N^{\gamma-1}\,\frac{\mathrm{d}N}{\mathrm{d}\xi} - \frac{1}{2}\,\frac{\mathrm{d}\left(b_y^2 + (b_z + \sin\theta)^2\right)}{\mathrm{d}\xi}. \tag{3.45}$$

The integration provides

$$-V\,u = -\frac{\beta_0}{2}\,N^{\gamma} - \frac{b_y^2 + (b_z + \sin\theta)^2}{2} + C_2, \tag{3.46}$$

where the integration constant C_2 can be fixed to

$$C_2 = \frac{\beta_0}{2} + \frac{\sin^2\theta}{2} \tag{3.47}$$

by means of Eq. (3.28) leading to

$$\frac{b_y^2 + b_z^2 + 2b_z\sin\theta}{2} = \frac{\beta_0}{2}\left(1 - N^{\gamma}\right) + V^2\,\frac{N-1}{N} \tag{3.48}$$

as a final result. Similarly, performing the same four-step analysis, Eq. (3.24) and Eq. (3.25) will result correspondingly into:

$$
\begin{aligned}
-V\frac{\mathrm{d}v_y}{\mathrm{d}\xi} &= \cos\theta\,\frac{\mathrm{d}b_y}{\mathrm{d}\xi} && (3.49)\\
-V\,v_y &= b_y\cos\theta + C_3 && (3.50)\\
C_3 &= 0 && (3.51)\\
v_y &= -\frac{\cos\theta}{V}\,b_y && (3.52)
\end{aligned}
$$

and

$$
\begin{aligned}
-V\,\frac{\mathrm{d}v_z}{\mathrm{d}\xi} &= \cos\theta\,\frac{\mathrm{d}b_z}{\mathrm{d}\xi} && (3.53)\\
-Vv_z &= b_z\cos\theta + C_4 && (3.54)\\
C_4 &= 0 && (3.55)\\
v_z &= -\frac{\cos\theta}{V}\,b_z && (3.56)
\end{aligned}
$$

Finally, Eq. (3.26) and Eq. (3.27) lead to:

$$
\begin{aligned}
-V\,\frac{\mathrm{d}b_y}{\mathrm{d}\xi} &= \cos\theta\,\frac{\mathrm{d}v_y}{\mathrm{d}\xi} - \frac{\mathrm{d}(ub_y)}{\mathrm{d}\xi} + \frac{\mathrm{d}}{\mathrm{d}\xi}\left(\frac{\cos\theta}{N}\frac{\mathrm{d}b_z}{\mathrm{d}\xi}\right) && (3.57)\\
C_5 &= -\frac{\cos^2\theta}{V}b_y + \frac{V}{N}b_y + \frac{\cos\theta}{N}\frac{\mathrm{d}b_z}{\mathrm{d}\xi} && (3.58)
\end{aligned}
$$

and

$$
\begin{aligned}
-V\frac{\mathrm{d}b_z}{\mathrm{d}\xi} &= \cos\theta\frac{\mathrm{d}v_z}{\mathrm{d}\xi} - \frac{\mathrm{d}(ub_z)}{\mathrm{d}\xi} - \frac{\mathrm{d}}{\mathrm{d}\xi}\left(\frac{\cos\theta}{N}\frac{\mathrm{d}b_y}{\mathrm{d}\xi}\right) && (3.59)\\
C_6 &= -\frac{\cos^2\theta}{V}b_z + \frac{V}{N}b_z - V\left(1-\frac{1}{N}\right)\sin\theta - \frac{\cos\theta}{N}\frac{\mathrm{d}b_y}{\mathrm{d}\xi}. && (3.60)
\end{aligned}
$$

In the case of solitary solutions, all disturbed quantities and their derivatives should vanish at infinity, i.e. $\xi \to \pm\infty$. In the case of oscillatory (or periodic) solutions, one should assume that b_y should be 0 at the maximum of b_z, i.e., at $\mathrm{d}b_z/\mathrm{d}\xi = 0$, as well as $b_z = 0$ at the maximum of b_y, i.e., at $\mathrm{d}b_y/\mathrm{d}\xi = 0$. Both conditions lead to

$$C_5 = C_6 = 0. \qquad (3.61)$$

In summary, the following system of equations

$$
\begin{aligned}
\frac{b_y^2 + b_z^2 + 2b_z\sin\theta}{2} &= \frac{\beta_0}{2}\left(1-N^\gamma\right) + V^2\,\frac{N-1}{N} && (3.62)\\
0 &= -\frac{\cos^2\theta}{V}b_y + \frac{V}{N}b_y + \frac{\cos\theta}{N}\frac{\mathrm{d}b_z}{\mathrm{d}\xi} && (3.63)\\
0 &= -\frac{\cos^2\theta}{V}b_z + \frac{V}{N}b_z - V\left(1-\frac{1}{N}\right)\sin\theta - \frac{\cos\theta}{N}\frac{\mathrm{d}b_y}{\mathrm{d}\xi} && (3.64)
\end{aligned}
$$

is the basic system of equations for the further study. It consists of one algebraic equation and two ordinary differential equations. One need to bear in mind that the particle number density is a function of ξ, i.e., $N = N(\xi)$.

3.3.1 Discussion of the parameter regime of the solutions

In the present Subsection it is intended to study the parameter regime of the different solutions of the stationary Sakai–Sonnerup system, that are basically nonlinear ones.
Because in the case of solitary solutions all disturbed quantities need to take small values at infinity, this justifies to linearize the Eqs. (3.62)–(3.64) and the linearization of Eq. (3.62) provides:

$$n = \frac{\sin\theta}{V^2 - c_\mathrm{s}^2} b_z, \tag{3.65}$$

where $c_\mathrm{s} = (\gamma\beta_0/2)^{1/2}$ is the sound speed. Since all disturbed quantities are decreasing with $\exp(-\lambda\xi)$ at $\xi \to \pm\infty$ for solitary solutions, Eqs. (3.63) and (3.64) result in a homogeneous system of equations,

$$\begin{aligned} 0 &= -\lambda\cos\theta\, b_z + \frac{V^2 - c_\mathrm{s}^2}{V}\, b_y \\ 0 &= \lambda\cos\theta\, b_z + \frac{1}{V}\left(V^2 - \cos^2\theta - \frac{V^2\sin^2\theta}{V^2 - c_\mathrm{s}^2}\right) b_z \end{aligned}$$

that leads to an expression for λ,

$$-\lambda^2 = \frac{(V^2 - \cos^2\theta)\left[(V^2 - V_+^2)(V^2 - V_-^2)\right]}{V^2\cos^2\theta(V^2 - c_\mathrm{s}^2)}, \tag{3.66}$$

where $V_\pm$ are the solutions of the equation $(V^2 - \cos^2\theta)(V^2 - c_\mathrm{s}^2) - V^2\sin^2\theta = 0$, namely,

$$V_\pm^2 = \frac{1 + c_\mathrm{s}^2}{2}\left[1 \pm \sqrt{1 - \frac{4c_\mathrm{s}^2\cos^2\theta}{(1 + c_\mathrm{s}^2)^2}}\right].$$

From Eq. (3.66) we have two possibilities: (i) $-\lambda^2 < 0$ for solitary solutions, and (ii) $-\lambda^2 > 0$ for oscillatory solutions (waves). That gives the following ranges of solutions:

- $V < V_-$, c_s, $\cos\theta$, V_+ – osc. I
- $V_- < V < c_\mathrm{s}$, $\cos\theta$, V_+ – sol. I
- V_-, $c_\mathrm{s} < V < \cos\theta$, V_+ – osc. II
- V_-, $\cos\theta < V < c_\mathrm{s}$, V_+ – osc. IV
- V_-, c_s, $\cos\theta, < V < V_+$ – sol. II
- V_-, c_s, $\cos\theta$, $V_+ < V$ – osc. III

plotted on Fig. 3.7, where the ranges of solitary and oscillatory solutions are denoted by 'sol' and 'osc', respectively. Here, a low-beta plasma is assumed, $\beta_0 = 0.4$. Otherwise, as will be shown in Chapter 4 for the case of high-beta plasma, kinetic effects need to be taken into account, i.e., the fluid approach would not be an appropriate plasma description anymore. The other free parameters are the angle θ and the phase speed V. With the so-chosen parameters, some representative plots in each range of all possible solutions (oscillatory and solitary ones) can be computed. Note that the specific values of V and θ place the solutions in the oscillatory or in the solitary regime.

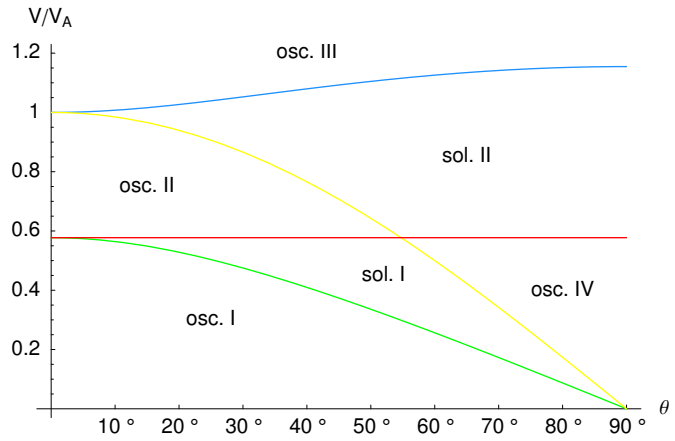

Figure 3.7: Plot of $V/V_{\mathrm{A}}(\theta)$, where V_+ is denoted with blue, V_- with green, c_{s} with red and $\cos\theta$ with yellow line. Additionally $\beta_0 = 0.4$.

Before calculating the solutions in each range of Fig. 3.7, here it is considered the right hand side of Eq. (3.48) as a function of N, i.e.,

$$F(N) = \frac{\beta_0}{2}\left(1 - N^{\gamma}\right) + V^2\left(1 - \frac{1}{N}\right) \tag{3.67}$$

and look for its maximum, $F(N_{\max})$, found at $N_{\max} = \left[2V^2/(\gamma\beta_0)\right]^{1/(\gamma+1)}$. Note that the function $F(N)$ has only one local extremum, namely a maximum at $N_{\max}$. The procedure of finding $F(N_{\max})$ is done in order to obtain an estimate for the range of possible values that the initial condition $b_z(0)$ can take. The value of the initial condition $b_z(0)$ is necessary for solving the differential equations (3.63) and (3.64). At $\xi = 0$, Eq. (3.48) reduces to:

$$b_z(0)^2/2 + b_z(0)\sin\theta \leq F(N_{\max}) \tag{3.68}$$

since $b_y(0) = 0$ is required. Or in short, after setting the angle θ to certain value and taking the already obtained values for $F(N_{\max})$, will lead to a range of possible solutions for $b_z(0)$, that was originally the aim. The used set of parameters for calculating the solutions of the stationary Sakai–Sonnerup system, presented in the next Subsections, are summarized in Table 3.1 (computed for $\gamma = 5/3$).

3.3.2 Example of a mathematical pendulum

Now as an example, we look at the 'mathematical pendulum' in order to illustrate the nature of 'oscillatory' and 'solitary' solutions. The movement of a mathematical pendulum with the length l is usually described by

$$\frac{d^2\phi}{dt^2} + \omega_0^2 \sin\phi = 0, \tag{3.69}$$

θ	V	$F(N_{\max})$	$N_{\max}$	Range of $b_z(0)$	Solution
0°	10.0	81.355	8.49	(–12.76; 12.76)	oscillatory
30°	0.2	0.0983	0.451	(–1.168; 0.168)	oscillatory
30°	0.55	0.0005	0.964	(–1.001; 0.001)	solitary
30°	0.7	0.1146	1.155	(–1.022; 0.022)	oscillatory
30°	0.86	0.0619	1.348	(–1.111; 0.111)	oscillatory
30°	1.0	0.1403	1.509	(–1.228; 0.228)	solitary
30°	1.6	0.853	2.148	(–1.898; 0.898)	oscillatory
30°	4.0	10.205	4.27	(–5.045; 4.045)	oscillatory
60°	0.2	0.0983	0.451	(–1.839; 0.107)	oscillatory
60°	0.4	0.0229	0.759	(–1.758; 0.026)	solitary
60°	1.0	0.1403	1.509	(–1.881; 0.149)	solitary
60°	1.6	0.853	2.148	(–2.433; 0.701)	oscillatory
80°	0.4	0.0229	0.759	(–1.992; 0.022)	oscillatory

Table 3.1: Computed $b_z(0)$-range and the parameter set, used for the numerical calculation.

with $\omega_0 = (g/l)^{1/2}$ and g is the gravitational acceleration. The angle ϕ denotes the temporal deflection of the pendulum off the vertical axis. Normalizing the time t to the inverse of the frequency ω_0, i.e., $t' = t\omega_0$, the Eq. (3.69) reduces to

$$\frac{d^2\phi}{dt'^2} + \sin\phi = 0, \tag{3.70}$$

where the prime will be omitted further on. In order to solve directly Eq. (3.70), one needs to set two initial conditions. For obtaining the oscillatory solutions of the pendulum, one sets $\phi(t=0) = \phi_0$ and $\dot{\phi}(t=0) = 0$. Then, ϕ_0 denotes the amplitude of the oscillations. The initial angle of deflection of the pendulum ϕ_0 can take any value in the range 0–π, but here for illustration are chosen $\phi_0 = 30°$, 90°, and 150°. Such choice of the initial conditions will result in the concentric curves in the (ϕ–$\dot{\phi}$)-plane, plotted on Fig. 3.8.

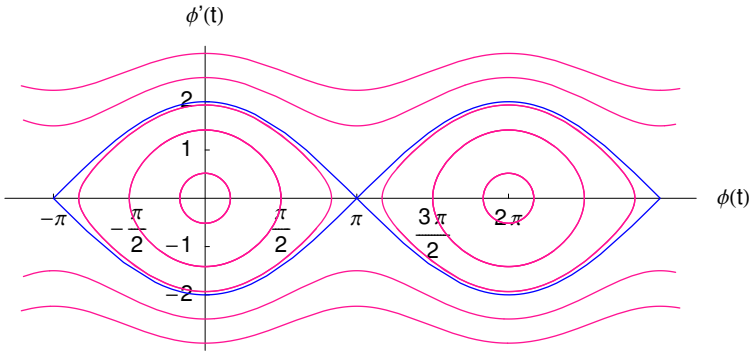

Figure 3.8: Phase portraits in the (ϕ-$\dot{\phi}$)-plane of a mathematical pendulum.

However, at one special point, namely $\phi_0 = \pi$, the only possible solitary solution is obtained (this is the separatrix, plotted in blue on Fig. 3.8). For the rotational motion, which is also possible for a mathematical pendulum, the initial conditions need to be changed (in this case to $\phi(t=0) = 0$ and $\dot{\phi}(t=0)$ with values ± 2.5 and ± 3). Note, that both the 'oscillatory' and 'rotational' solutions are periodic ones and a solitary solution occurs only for a single (definite) value of the initial conditions. In the case of 'solitary' solution, the movement starts with $\dot{\phi}(t=0) = 0$ at $\phi(t=0) = \pi$ and needs an infinite time to reach $\phi = -\pi$.
Multiplying Eq. (3.70) with $\dot{\phi}$ and, subsequently, integrating once, one gets

$$\dot{\phi} = \pm\sqrt{2(C + \cos\phi)}, \tag{3.71}$$

where C is the integration constant. In order to get a real solution, $C + \cos\phi \geq 0$ is required. Then, the three types of solutions are obtained with the following choice for the constant C:

1. $-1 < C < 1$ leads to an 'oscillatory' solution (see the curves enclosed by the blue curve on Fig. 3.8). Then, $\phi_{\max} = \arccos(-C) < \pi$ gives the amplitude of the oscillations.

2. $C = 1$ provides the 'solitary' solution (see the blue curve on Fig. 3.8). Here, the movement starts at $\phi = \pi$ at $t = 0$ and needs an infinite time to reach the final point at $\phi = -\pi$.

3. $C > 1$ provides no zeros of $\dot{\phi}$, i.e., it leads to 'rotational' solutions. Here, it is chosen, $C = 2.125$ (corresponding to $\dot{\phi}(0) = \pm 2.5$), and $C = 3.5$ ($\dot{\phi}(0) = \pm 3$), both for $\phi(0) = 0$ (see the open curves on Fig. 3.8).

Additionally, the half period of a mathematical pendulum is given by,

$$\frac{T}{2} = 2\int_0^{\phi_{\max}} \frac{d\phi}{\sqrt{2(C + \cos\phi)}},$$

where $\phi_{\max} = -\arccos(C)$. A plot of the dependence of the half period of the mathematical pendulum $T/2$ on the constant C is given on Fig. 3.9. In the case of a solitary solution, i.e., $C = 1$, the period of the pendulum tends to infinity.

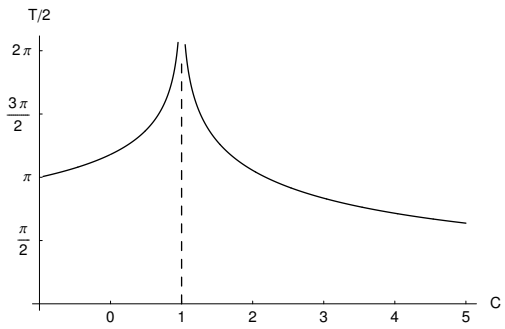

Figure 3.9: Dependence of $T/2$ from C.

On Fig. 3.10, the dependence $\phi(t)$ and $\dot{\phi}(t)$ for four different initial conditions is shown, as given on the top of each plot. Each row of two plots represents the certain solution/curve from Fig. 3.8, namely, two oscillatory solutions, the separatrix/solitary solution and one rotational solution (from top to bottom). There, one can follow the change in the shape of the curves (in the corresponding columns), while passing from one type of solution (e.g., oscillatory/solitary) to another (e.g., solitary/rotational), correspondingly. One can see that the period is increasing with the amplitude for $\phi(0) < \pi$, whereas it is decreasing after

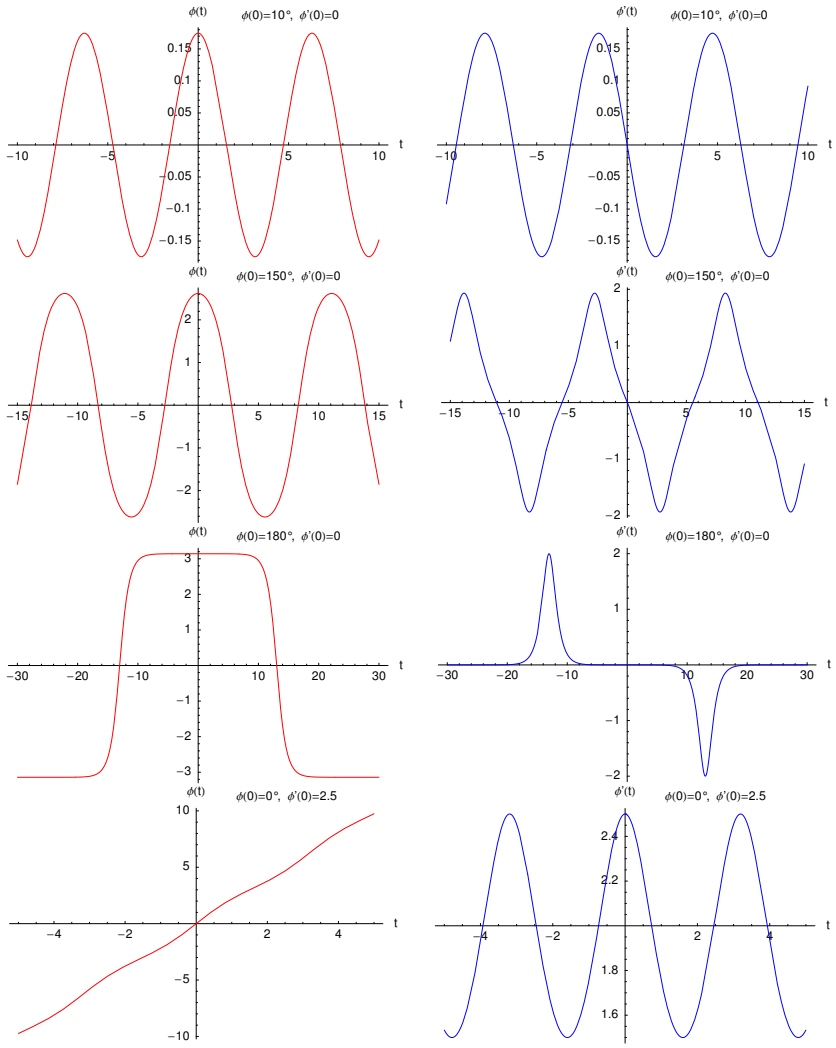

Figure 3.10: Plots of $\phi(t)$ (left panel) and $\dot{\phi}(t)$ (right panel) for initial conditions as given on the top of each plot.

exceeding $\phi(0) = \pi$. The solitary nature of the solution with $\phi(0) = \pi$ is obvious (see third row in Fig. 3.10).

The mathematical pendulum is a simple, but non-trivial example of a fully nonlinear problem, which fortunately can be easily imagined. For small deflections, one obtains linear oscillations with a frequency, which is not depending on the amplitude. With increasing amplitudes, the motion leaves the linear regime. That is characterized by the fact, that the period of the oscillation becomes dependent from the amplitude. The study performed here shows, that the period is increasing with the amplitude (see Fig. 3.10). If the amplitude reaches π, one gets a very special solution, which corresponds to the 'solitary' one. Here, the

pendulum starts with an infinitely slow velocity at π and reach asymptotically the state $-\pi$ after a infinitely long time, i.e., $T/2 \to \infty$ (Fig. 3.8 and Fig. 3.9). This 'solitary' solution separates the 'oscillatory' solutions from the 'rotational' ones (Fig. 3.8). All solutions can be characterized by the initial conditions, i.e., the choice of $\dot{\phi}$ and C, covering the range $0 \leq \dot{\phi} < \infty$ and $-1 \leq C < \infty$, respectively. It should be noted, that the 'solitary' solution is only given for one point in this parameter range, i.e., $\dot{\phi} = 0$ and $C = 1$. All other conditions provide periodic (either oscillatory or rotational) solution. That impressively demonstrates the singular nature of the 'solitary' solution.

3.3.3 Special stationary solutions

In this Subsection some special solutions of the system of Eqs. (3.62)–(3.64) are presented. Because the aim of the thesis is not to discuss the complete manifold of solutions of this system of equations, only some special cases of all solutions are presented here[2]. As expected, oscillatory and solitary solutions are obtained. The detailed numerical evaluation of the system of equations (3.62)–(3.64), provides in addition a third kind of solution, that is called here an 'open' solution. When the solutions are plotted in a (b_z–b_y)-plane, the oscillatory and solitary solutions appear as closed contours. In contrast to these cases, the 'open' solutions, as suggested by their notation, are characterized as a finite bow-like curve. A detailed inspection of the 'open' solutions, provides that outside the completed (and plotted on all images with dashes) path, the algebraic equation (3.62) is violated and hence the system of equations provides no more a common solution. Therefore, this type of the solutions is not discussed further.

As already mentioned, a solution of the Eqs. (3.62)–(3.64) is determined by choosing the parameters β_0, θ and V. Here for the parameter β_0 is chosen 0.4, because at a higher value kinetic effects become important and the fluid description used here is no longer an appropriate one (see also Chapter 4). Furthermore, in order to illustrate some special examples, one focuses on angles of propagation of $\theta = 30°$ and $\theta = 60°$. The last parameter, the velocity V, can take arbitrary positive values, that will place the solution in one of all 6 possible ranges of solutions (see Fig. 3.7).

Finally, the system of Eqs. (3.62)–(3.64), representing a system of one algebraic and two ordinary differential equations, can be solved numerically. Additionally, the initial conditions need to be introduced, that in this case are: $b_y(0) = 0$, range of $b_z(0)$ (from Eq. (3.68) given in details in Table 3.1), and $b_z'(0) = 0$. The solutions of the system of equations are sought inside a symmetric ξ-range in the form: $b_y(\xi)$, $b_z(\xi)$, $|b|(\xi)$ (i.e., the magnitude of the magnetic field, $b(\xi)^2 = \cos^2\theta + b_y(\xi)^2 + (b_z(\xi) + \sin\theta)^2$), and $N(\xi)$. Solutions are found for different combinations of the initial conditions and the parameters $\beta_0 = 0.4$, θ and V. Another important issue is to construct a so-called 'hodograph' representation of the solutions [73], i.e., plotting them in a (b_z–b_y)-plane. Hence, an analogy of the visual shape

[2] A detailed study of the different families of stationary solutions of the equations of Hall magnetohydrodynamics is found in [8, 65, 103, 73]. In the limit of small but finite amplitude magnetic field fluctuations, those equations reduce to the 'derivative non-linear Schrödinger' (DNLS) equation, which is basically non-linear and provides solitary solutions [8, 73].

of the 'hodograph' curves, can be drawn to the phase curves in the case of a mathematical pendulum, plotted in the phase portrait on Fig. 3.8, i.e., in the $(\phi$–$\dot{\phi})$-plane.

The numerical procedure is performed as follows: For each set of input parameters (i.e., $\beta_0 = 0.4$, θ, and V) and initial conditions (i.e., $b_y(0) = 0$, $b_z(0)$-range, see Table 3.1, and $b_z'(0) = 0$), the system of equations (3.62)–(3.64) is solved and the solution is plotted in the $(b_z$–$b_y)$-plane, see Figs. 3.11–3.14. The calculation is repeated with the same set of parameters, but this time with another value for $b_z(0)$. Choosing nearly equidistant values for the initial condition $b_z(0)$ (when possible), places the solutions or the curves also at equal separation on the $b_z(\xi)$-axis. For example, the following choice of parameters, $\theta = 30°$, $V = 0.2$, and $b_z(0) = 0.05$, corresponds to the innermost circular curve on Fig. 3.11. On the other side, choosing $b_z(0) = -0.2$ leads to a solution represented with an 'open' curve this time, that is passing exactly through the point -0.2 on the $b_z(\xi)$-axis (and plotted with dashed line). Because the parameter set given in Table 3.1 is used, each line of the table corresponds to a given 'hodograph' curve (i.e., in the $(b_z$–$b_y)$-plane).

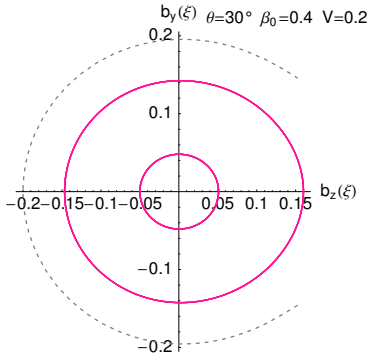

Figure 3.11: Oscillatory solutions (from right to left) for $b_z(0)$: 0.16, 0.05 (pink); -0.2 (dashed). For further details see the text.

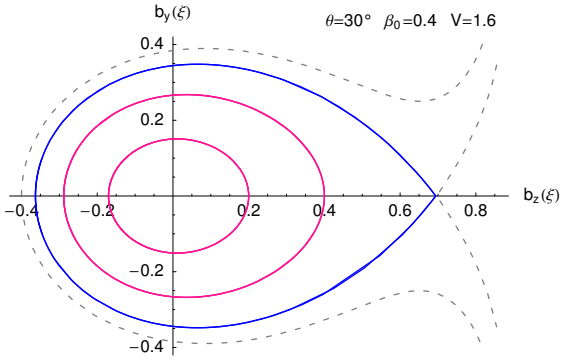

Figure 3.12: Oscillatory solutions (from right to left) for $b_z(0)$: 0.4, 0.2 (pink); -0.3632 (blue), and 0.7, -0.4 (dashed).

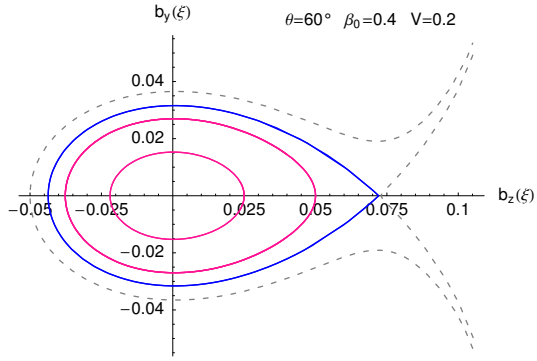

Figure 3.13: Oscillatory solutions (from right to left) for $b_z(0)$: 0.05, 0.25 (pink); 0.072 (blue), and 0.073, -0.05 (dashed).

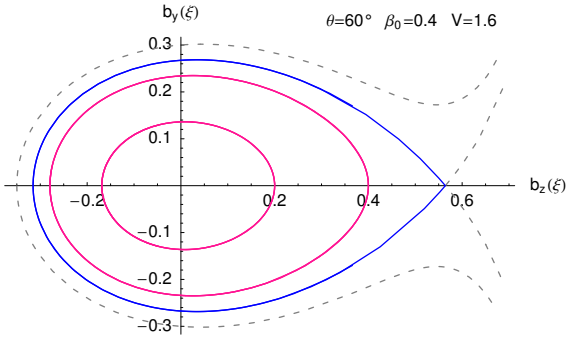

Figure 3.14: Oscillatory solutions (from right to left) for $b_z(0)$: 0.4, 0.2 (pink); 0.564 (blue), and 0.565, -0.35 (dashed).

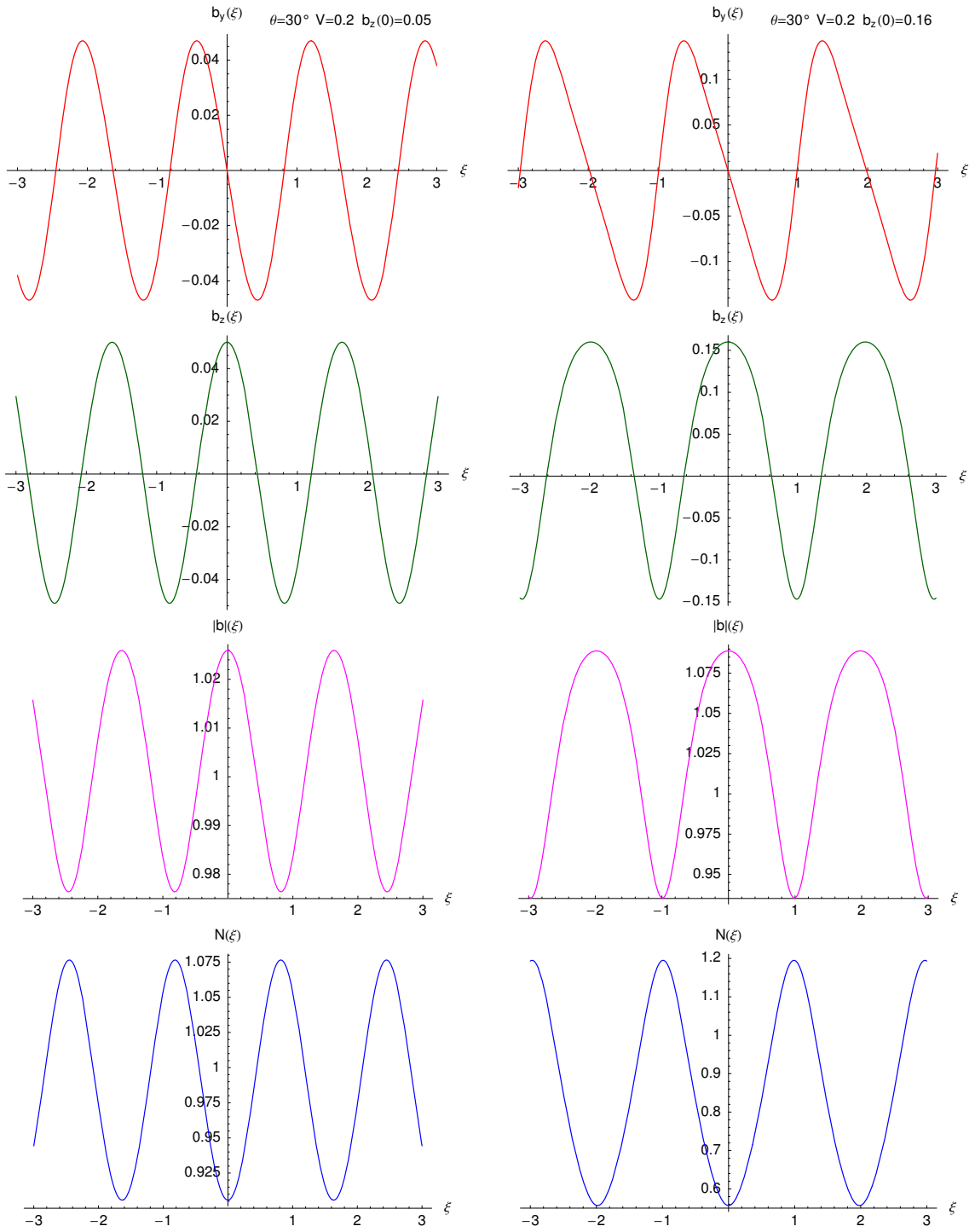

Figure 3.15: Plots of $b_y(\xi)$, $b_z(\xi)$, $|b|(\xi)$, and $N(\xi)$ from Fig. 3.11 'osc. I': for $b_z(0) = 0.05$ (left panel), and for $b_z(0) = 0.16$ (right panel).

The exact values for the parameters and the initial condition $b_z(0)$ vary for each case and thus they are explicitly given in each figure caption. Now it is focused on the 'osc I' and 'osc III'-ranges (from Fig. 3.7), where for the parameters are chosen to be the following values: $\theta = 30°$ with $V = 0.2$ and 1.6 and $\theta = 60°$ with $V = 0.2$ and 1.6, correspondingly plotted on Figs. 3.11–3.14. From nearly circular shape (Fig. 3.11), the curves 'degenerate' into ellipses for the same angle θ (Fig. 3.12), when the parameter V is increased.

The dependencies of b_y, b_z, $|b|$, and the density, N, on the coordinate ξ comprise a panel of 4 plots, as can be seen on Figs. 3.15–3.17 and Fig. 3.19. The plots on Fig. 3.15 are for $\beta_0 = 0.4$, $\theta = 30°$ and $V = 0.2$, as well as for $b_z(0) = 0.05$ and 0.16. i.e., in the range of 'osc. I'. In the case of $b_z(0) = 0.05$, the plots are reminiscent to the harmonic wave accompanied with very weak density variations. In the case of $b_z(0) = 0.16$, an asymmetric shape (i.e., steepened trailing edge) of the $b_y(\xi)$ behaviour is visible. This is a non-linear property. After comparing both panels on Fig. 3.15, it is seen that the period of the oscillations is increasing with increasing the initial value of $b_z(0)$, i.e., the period of the oscillatory solution is depending on the amplitude. That is a typical non-linear property as already seen in the example of the mathematical pendulum (Fig. 3.10). In addition, strong density variations are accompanied with the magnetic field fluctuations in the case of $b_z(0) = 0.16$, according to Eq. (3.62).

Changing the angle from 30° to 60° and choosing the initial condition $b_z(0) = 0.05$, the departure from the harmonic bahaviour is seen at the $b_y(\xi)$-behaviour, comparing Fig. 3.15 (left panel) to Fig. 3.16 (also left panel). In all these cases, belonging to the 'osc. I' range on Fig. 3.7, a maximum of $|b|$ is related to a local density depletion. In contrast, the parameters on Fig. 3.16 (right) correspond to the 'osc. III' range, and in this range a compression in the density is seen for a maximum of $|b|$ at $\xi = 0$. For completeness, similar four-panel plots are computed for the oscillatory solutions in the 'osc. II' and 'osc. IV' ranges, as presented on Fig. 3.17. There, for a maximum of $|b|$ at $\xi = 0$, one can see a density compression in the 'osc. II' case and density depletion in the 'osc. IV' case. However, the b_y-behaviour (i.e., the positions of the minimum and maximum values) is different in both 'depletion' ranges ('osc. I' and 'osc. IV') and also in both 'compression' ranges ('osc. II' and 'osc. III'), compare the corresponding panels on Fig. 3.16 and Fig. 3.17. Another important issue in the range of oscillatory solutions is the appearance of a 'separatrix' (the blue curve on the Figs. 3.12–3.14). It is similar to the separatrix in the case of a pendulum motion (see Fig. 3.8), but here it can be obtained for two different values of the initial condition $b_z(0)$.

Approaching the range of solitary solutions (i.e., moving towards 'sol. I'-range on Fig. 3.7), leads to the so-called 'banana'-like curves, that can be clearly seen on Fig. 3.18. The dependence on ξ for $b_z(0) = -0.1$, is plotted on Fig. 3.19. Such 'banana'-like (or also called 'arc'-like) polarizations are really seen in terms of magnetic field fluctuations in the interplanetary space [112]. In comparison to the other oscillating solutions (see Figs. 3.15–3.17), they have long periods of about 75 in the dimensionless ξ-space. Additionally, they show steepened trailing edges, where density depletions occur. Both are pure non-linear properties.

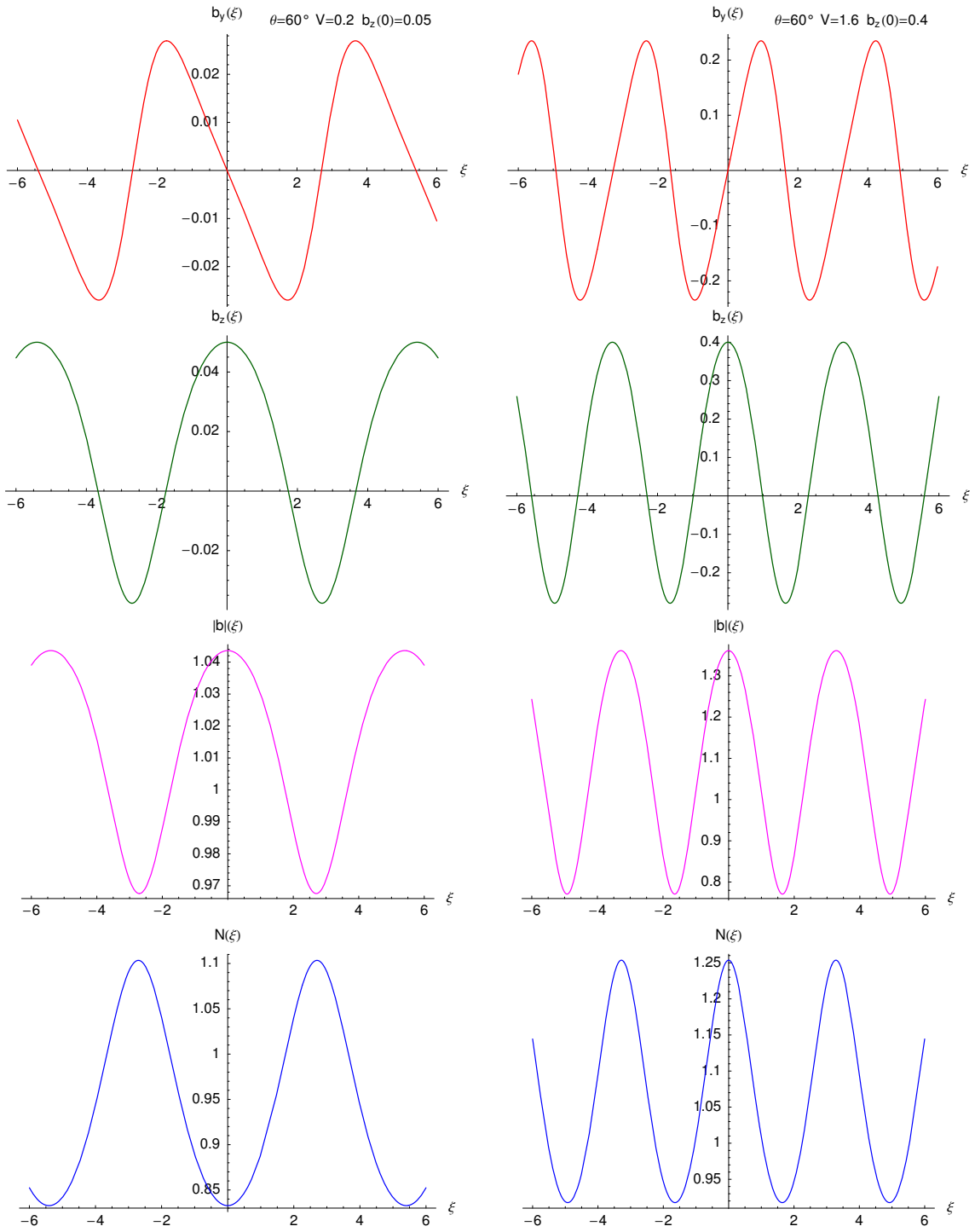

Figure 3.16: Plots of $b_y(\xi)$, $b_z(\xi)$, $|b|(\xi)$, and $N(\xi)$: from Fig. 3.13 'osc. I', for $b_z(0) = 0.05$ (left panel), and from Fig. 3.14 'osc. III', for $b_z(0) = 0.4$ (right panel).

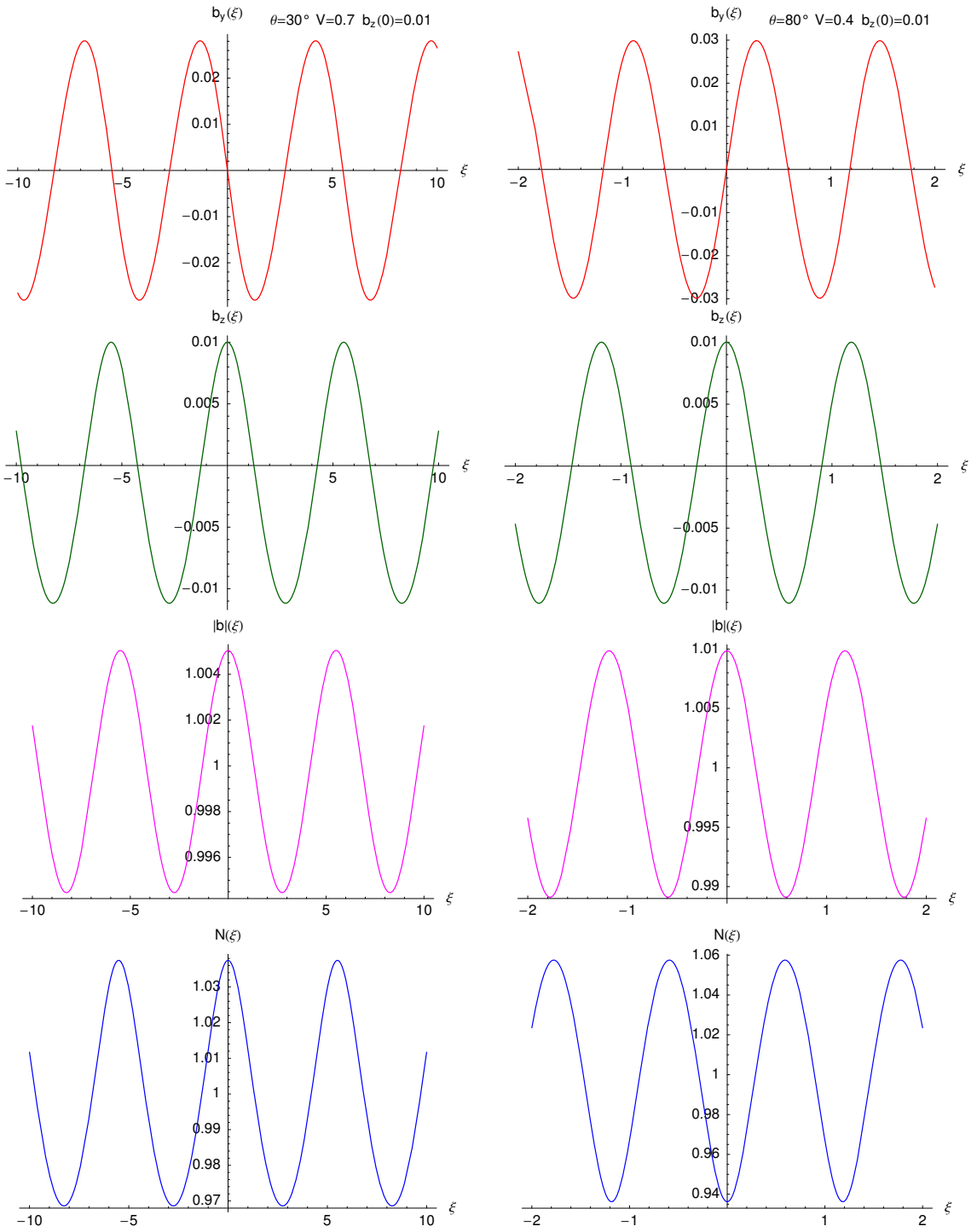

Figure 3.17: Plots of $b_y(\xi)$, $b_z(\xi)$, $|b|(\xi)$, and $N(\xi)$ for $b_z(0) = 0.01$: 'osc. II'-range (left panel), and 'osc. IV'-range (right panel).

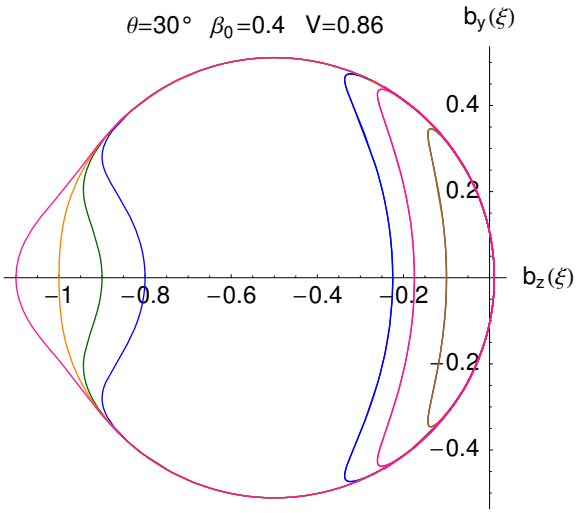

Figure 3.18: Oscillatory solutions (from right to left) for $b_z(0)$: -0.1 (brown), -0.8 (blue), -0.9 (green), -1.0 (orange) and -1.1 (pink). No solutions for $b_z(0) \in (0.25, 0.75)$.

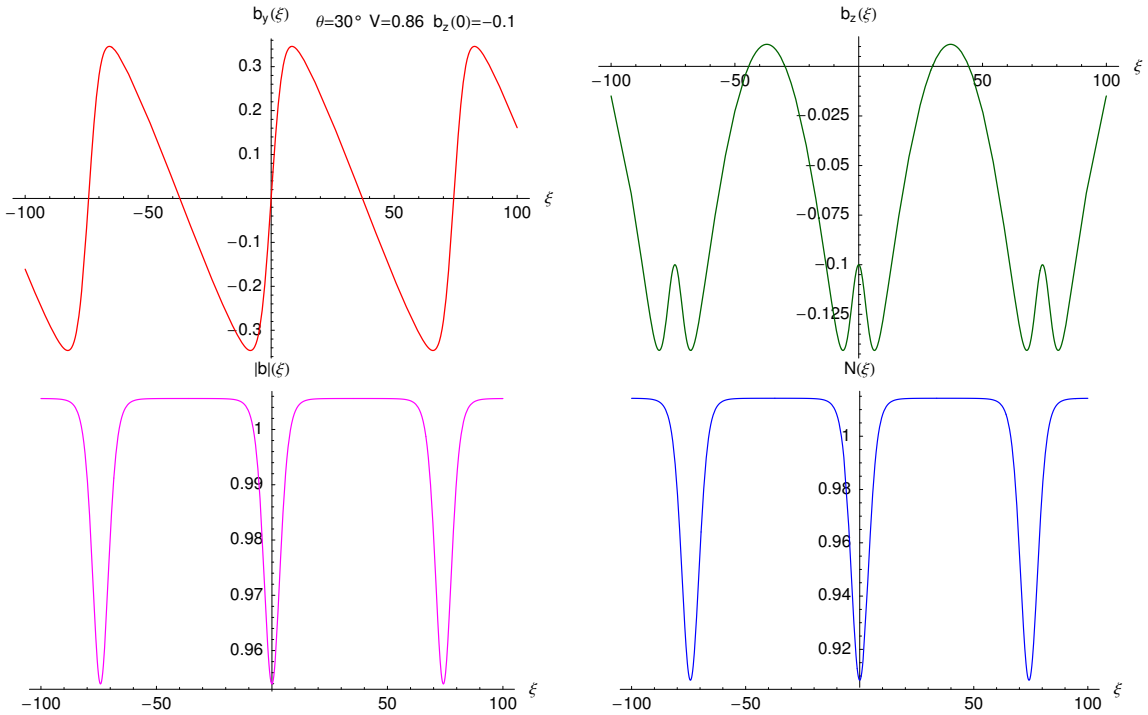

Figure 3.19: Plots of $b_y(\xi)$, $b_z(\xi)$, $|b|(\xi)$, and $N(\xi)$ from Fig. 3.18 for $b_z(0) = -0.1$.

In the range of parameters corresponding to the areas of 'sol. I' and 'sol. II' (see Fig. 3.7), solitary solutions are obtained, as depicted on the 'hodographs' on Figs. 3.20 and 3.22 ('sol. I') and on Figs. 3.21 and 3.23 ('sol. II'), respectively. The corresponding explicite solutions are presented in Figs. 3.24 and 3.25. In all presented cases, $b_z(\xi)$ and $|b|(\xi)$ are

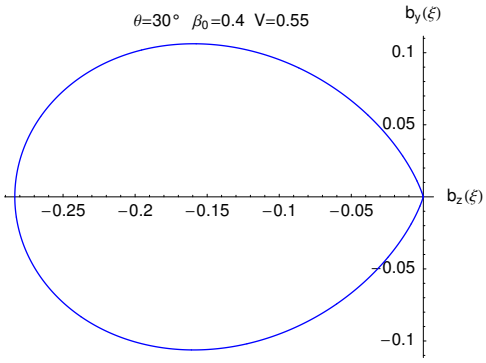

Figure 3.20: Solitary solution in the 'sol. I' range for $b_z(0) = -0.2835$.

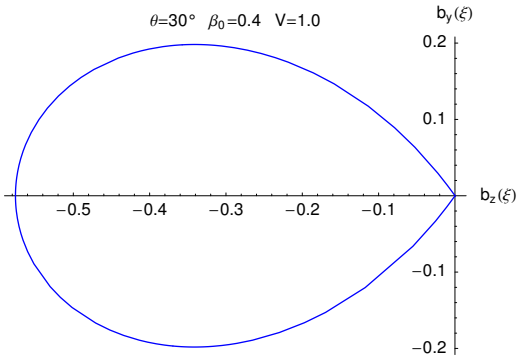

Figure 3.21: Solitary solution in the 'sol. II' range for $b_z(0) = -0.5758$.

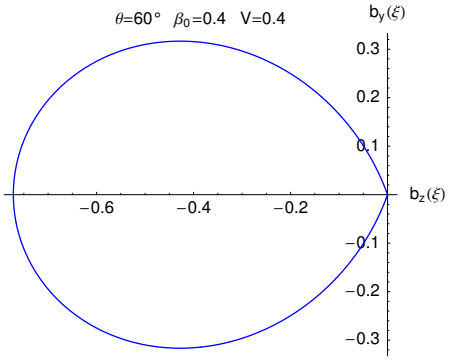

Figure 3.22: Solitary solutions in the 'sol. I' range for $b_z(0) = -0.7716$.

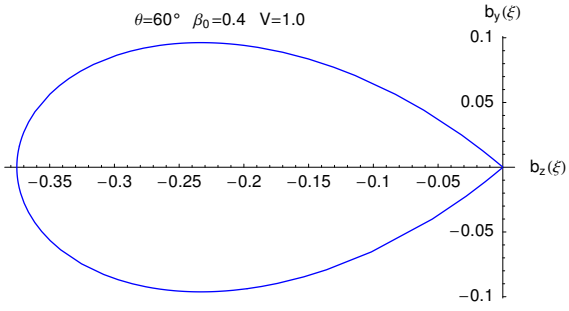

Figure 3.23: Solitary solution in the 'sol. II' range for $b_z(0) = -0.3754$.

always smaller than 0 and 1, respectively. For parameters related to 'sol. I'-range, the solitons are accompanied by a density compression. A density depletion occurs for the solitary solutions in the parameter range 'sol. II'. Such solutions are found as so-called magnetic holes in the interplanetary space [8, 103], for instance.

Additionally, the overall shape of the oscillatory and the solitary solutions intrinsically differs as a function of ξ. From Eq. (3.63), follows that an extremum of b_z (i.e., $\mathrm{d}b_z/\mathrm{d}\xi = 0$), corresponds to $b_y = 0$, in the specific case of b_z^{extr}. An analytical expression for the value of b_z in the point of the extremum can be found setting the condition $b_y = 0$ in Eq. (3.62), or finally,

$$b_z^{\mathrm{extr}} = \sin\theta \pm \sqrt{\sin^2\theta + 2F(N)}.$$

This can be seen comparing the numerical solutions for the oscillatory solutions (Figs. 3.15–3.17), having maximum of b_z at $\xi = 0$, whereas in the solitary case (Figs. 3.24 and 3.25), b_z has minimum at $\xi = 0$. The density compression (maximum of $N(\xi = 0)$) is obtained in the 'osc. II', 'osc. III', and 'sol. I' ranges, whereas the density depletion (minimum of $N(\xi = 0)$) occurs in the 'osc. I', 'osc. IV', and 'sol. II' ranges. In all plots, $b_y(\xi = 0) = 0$, as required from the initial condition.

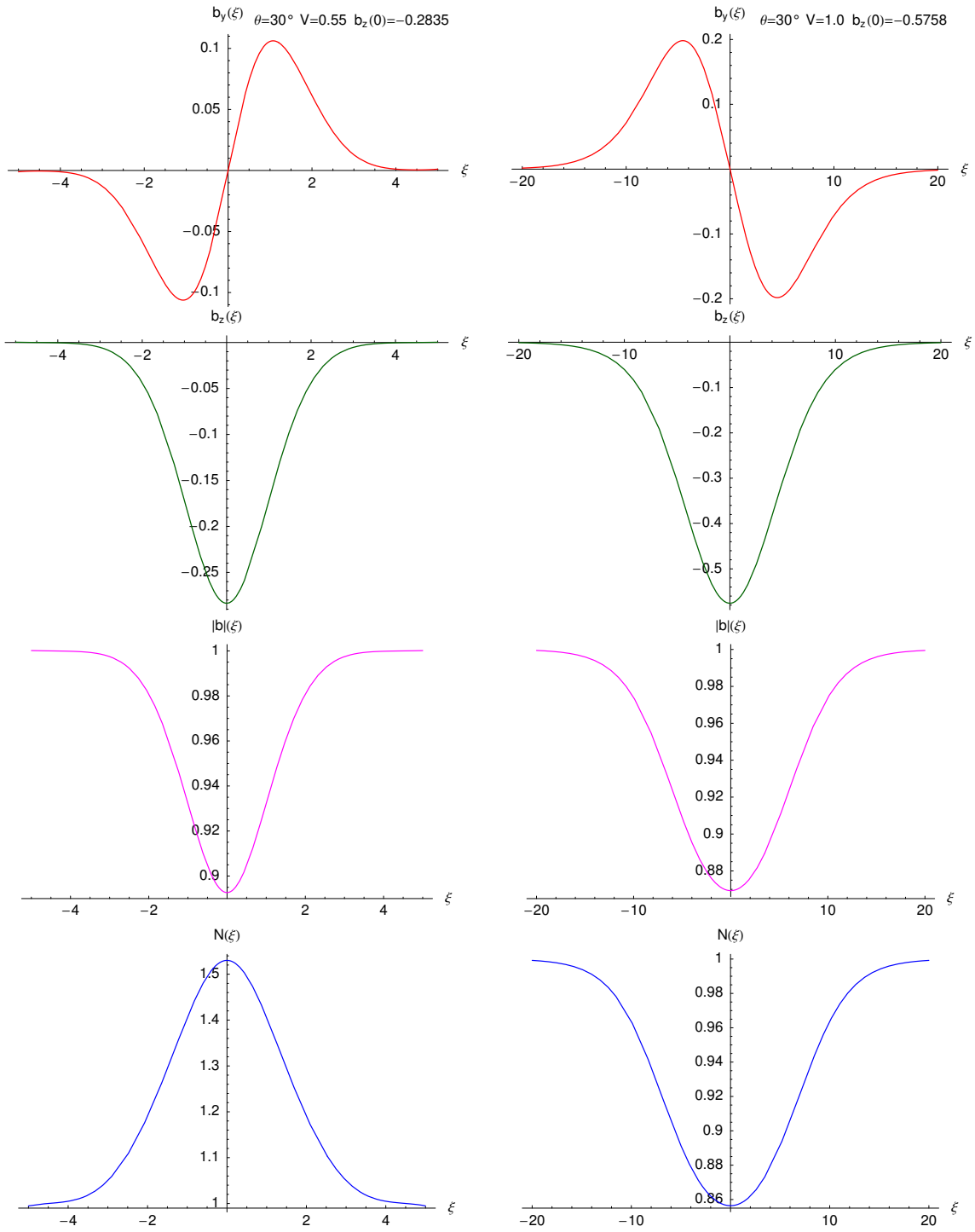

Figure 3.24: Plots of $b_y(\xi)$, $b_z(\xi)$, $|b|(\xi)$, and $N(\xi)$ for $b_z(0) = -0.2835$ from Fig. 3.20 (left panel), and for $b_z(0) = -0.5758$ from Fig. 3.21 (right panel).

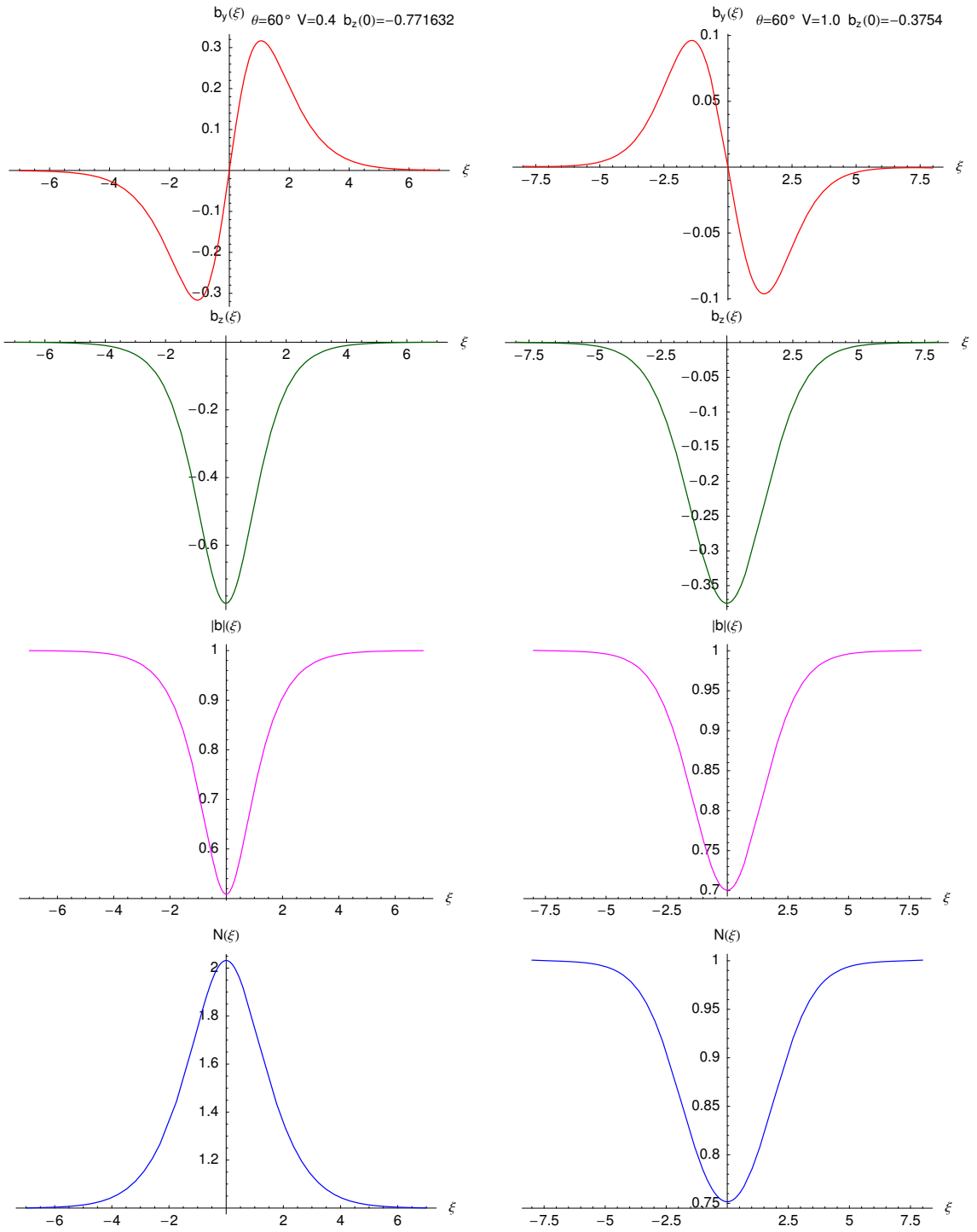

Figure 3.25: Plots of $b_y(\xi)$, $b_z(\xi)$, $|b|(\xi)$, and $N(\xi)$ for $b_z(0) = -0.7716$ from Fig. 3.22 (left panel), and for $b_z(0) = -0.3754$ from Fig. 3.23 (right panel).

3.3.4 Nonlinear whistler waves

The parametric range associated with the 'osc. III' corresponds to whistler waves at low frequencies, i.e., much lower than the electron cyclotron frequency. For these solutions, the velocity V exceeds the Alfvén speed. In this subsection, the hodograph curves for $\theta = 0°$ and $30°$ are computed, see Fig. 3.27 and Fig. 3.26, respectively. The corresponding behaviour

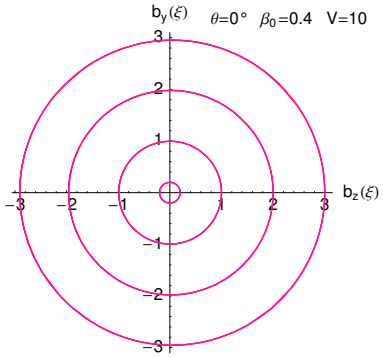

Figure 3.26: Solutions (from right to left) for $b_z(0)$: 3, 2, 1, and 0.2.

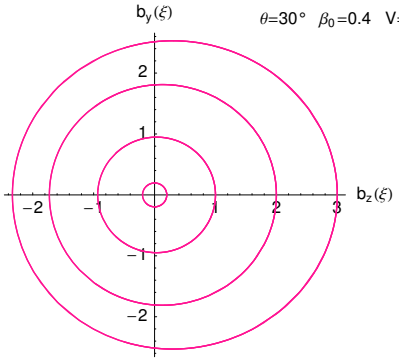

Figure 3.27: Solutions (from right to left) for $b_z(0)$: 3, 2, 1 and 0.2.

in the ξ-space is given on Fig. 3.28. The case for $60°$ was already presented on Figs. 3.12, 3.14 and 3.16 (the right panel there). In general, the period is decreasing with increasing V, and the associated density fluctuations become weaker with increasing V, as expected by Eq. (3.62). For $V \gg 1$, Eq. (3.62) reduces to

$$\frac{b_y^2 + b_z^2 + 2\, b_z\, \sin\theta}{2} = V^2\, \frac{N-1}{N}$$

providing $|N-1| \ll 1$ for finite amplitudes, i.e., b_y, $b_z < 1$. Such whistlers are really seen in space plasmas (see Fig. 3.3) and play important role for accelerating electrons in the upstreaming region of shocks in collisionless plasmas, as will be discussed in Chapter 5.

In summary, the Sakai–Sonnerup system (3.62)–(3.64) describes the evolution of one-dimensional plasma waves for frequencies much lower than the electron cyclotron frequency, so that the displacement current and the charge separation effects can be neglected. The stationary solutions of the Sakai–Sonnerup system offers both oscillatory and solitary solutions, reminiscent to the fully non-linear motion of a mathematical pendulum. In this respect, the solitary solution separates different types of solutions as was discussed in details in the present Chapter. It should be pointed out, that the solitary solution is related to a very special choice of parameters and initial conditions. This fact means actually that the oscillatory (or periodic) solutions are mostly probably to occur in space plasmas. They are related to different kinds of polarization, e.g., circular, elliptical and banana-like polarization, as really observed in terms of low frequency magnetic field fluctuations in space plasmas.

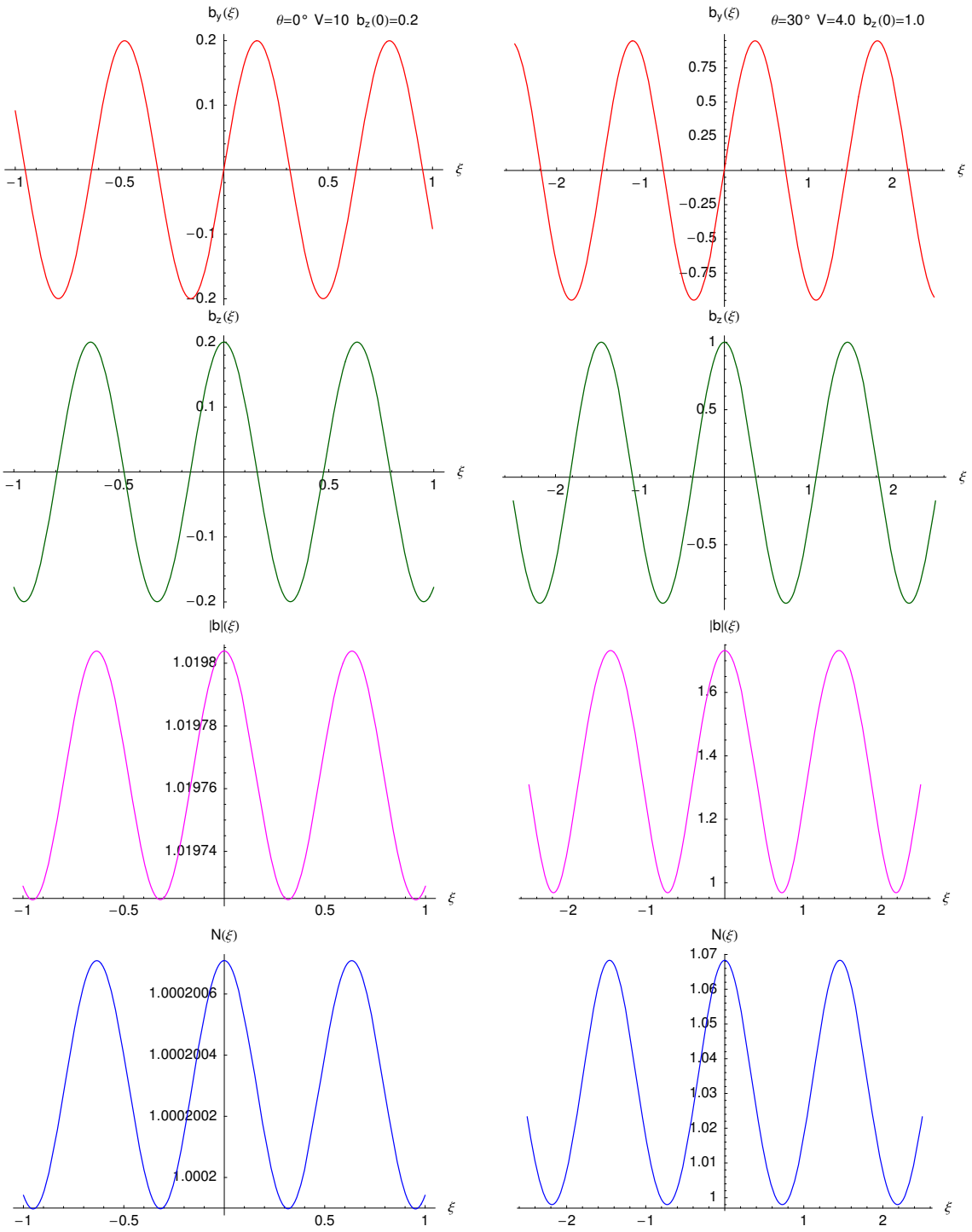

Figure 3.28: Plots of $b_y(\xi)$, $b_z(\xi)$, $|b|(\xi)$, and $N(\xi)$ for $b_z(0) = 0.2$ (left panel) from Fig. 3.26 and for $b_z(0) = 1.0$ (right panel) from Fig. 3.27.

Chapter 4

Electron energization due to jet propagation in the solar corona

4.1 Introduction

4.1.1 Observations on solar jets and accelerated electrons

Solar jets

Plasma jets in the solar corona were discovered on the images from the soft X-ray telescope (SXT) aboard *Yohkoh* satellite, see e.g., [97, 106, 99]. Example of a solar jet is presented as a sequence of snap shots at 195 Å from the TRACE satellite on Fig. 4.1. The observed physical parameters of the jets were already summarized in Subsect. 1.5.1.

Many jets were observed to occur at flare events, e.g., in X-ray bright points (XBPs), emerging flux regions (EFRs) or active regions (ARs). As it is widely known, during solar flares stored magnetic field energy is suddenly released and transfered into plasma heating, mass motions (e.g., jets and/or coronal mass ejections), energetic particles (e.g., electrons, protons, and heavy ions), and radiation across the whole electromagnetic spectrum, i.e., from radio waves up to γ-rays, [30]. When two magnetic field lines with opposite directions approach each other due to their photospheric footpoint motion (see Fig. 1.18), a current sheet is established between them. If the electric current exceeds a certain critical value, the anomalous resistivity is suddenly increased by exciting plasma waves owing to various

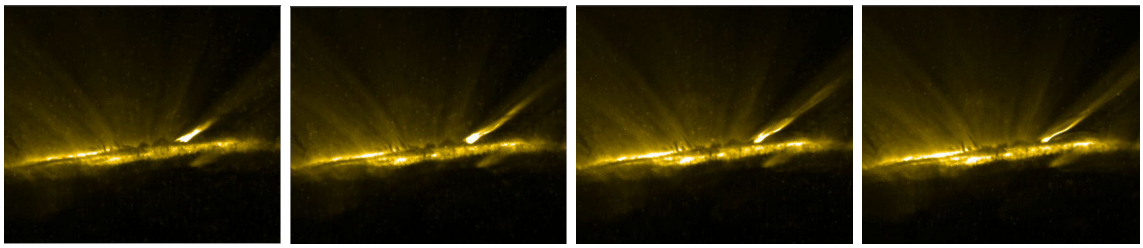

Figure 4.1: Solar jets from TRACE satellite, detected on 30–Jul–2004 at 195 Å.

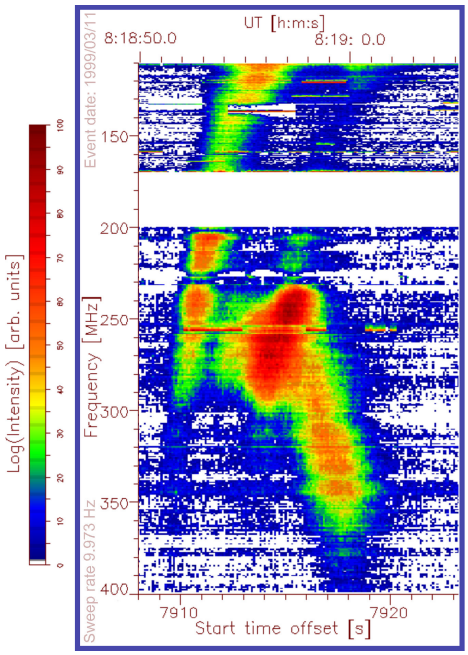

Figure 4.2: Metric type III and U radio bursts in the frequency range 110–400 MHz, seen in the dynamic radio spectrum recorded by the radio spectralpolarimeter [53] of the Observatory for Solar Radio Astronomy (OSRA), Germany.

plasma instabilities, [110]. A process known as magnetic reconnection takes place rearranging the magnetic field line configuration. Due to the strong curvature of the newly formed magnetic field lines, the plasma is shooting away from the reconnection site leading to the establishment of (sometimes oppositely directed) jets of hot plasma (see also Fig. 1.18, Chapter 1). As already discussed by [124, 125], magnetic reconnection is the most probable mechanism leading to the generation of the solar jets.

Accelerated electrons

Beams of accelerated electrons are observed in the solar corona, in terms of type III metric radio bursts (see Chapter 1). The solar type III radio bursts are usually regarded as the signature of beams of supra-thermal electrons [74]. An example of a solar type III and U radio bursts is presented in Fig. 4.2. It shows a dynamic radio spectrum in the range 110–400 MHz, recorded in the Observatory for Solar Radio Astronomy (OSRA), Germany. A stripe of enhanced radio emission starts near 350 MHz at 08:18:51 UT and rapidly drifts towards lower frequencies down to 110 MHz. This is a typical type III radio burst, which is considered to be a signature of an electron beam traveling along open magnetic field lines outwards in the corona. Another feature starts near 300 MHz at 08:18:53 UT, reaches 230 MHz at 08:18:57 UT, and turns back towards higher frequencies, reaching 400 MHz at 08:19:00 UT. It represents the so-called type U radio burst, that is regarded as an electron beam traveling along closed magnetic field lines in the corona, according to the commonly

accepted interpretation of such emission [3, 4] (see Subsect. 1.4.1). The dynamic radio spectrogram indicates that both electron beams are generated near the same place and time in the corona.

The accelerated electron beams in terms of type III/U radio bursts and the mass motion through the solar corona in terms of soft X-ray jets, are the two components of the performed theoretical analysis in the present Chapter. The analytical and numerical explanation of the electron energization due to the jet propagation in the coronal plasma is the aim of the subsequent Sections. Initially, a procedure of association between the two kind of events (i.e., jets and radio bursts) needs to be performed, and its main properties are summarized in the following Subsection.

4.1.2 Jet associated type III/U radio bursts

Soon after the *Yohkoh* discovery of the solar jets with its SXT instrument, a good spatial and temporal correspondence of soft X-ray jets to type III and U metric bursts in radio emission was recognized. Here, an attempt of a summary comprising the reported events on jet associated radio bursts is performed, and its results are presented in Table 4.1.

The first reports, see [81, 5, 45], on the correlation of a type III radio burst and a jet-like brightening in the corona were done by a joint multi-frequency analysis of: i) spectrographic radio data, e.g., from University of Porto[1] (Portugal), OSRA Tremsdorf[2] (Germany), ARTEMIS[3] (Greece); ii) imaging radio data, e.g., from the Nançay radioheliograph (NRH)[4] (France); and iii) soft X-ray data, from *Yohkoh*/SXT. Type III and U radio bursts were clearly associated (temporally and spatially) with: a coronal structure, a jet-like feature, or a whip-like brightening from a XBP. The general outcome from the data analysis is that the path of the electron beams responsible for the type III/U radio burst is directed along the soft X-ray jet.

Further examples on the association between metric type III bursts and soft X-ray jets soon followed, see [43, 84]. There, for a first time it was presented a comprehensive radio and soft X-ray analysis, where the physical parameters of the jets were also estimated. Additionally, the centroids of the type III bursts at different frequencies were confirmed to be aligned in the direction of the soft X-ray jets. Further evidence for the production of non-thermal radio emission associated with soft X-ray ejection at the top of a coronal loop was reported by [85]. The collected data set by all these authors gives an evidence for the good spatial and temporal correspondence between soft X-ray jet and nonthermal electron beams in terms of metric radio bursts. In general, when solar jets occur in a complex magnetic field configuration (as in the case of a two-sided-loop jet, see Fig. 1.19), the accelerated electrons also will travel along the closed field lines and hence type U radio bursts are naturally expected to be observed in the radio spectrum. In fact, reports on type U radio bursts were given, by [5, 81], but with no information on the type of the associated jet. On the other hand,

[1]Radio Spectrograph of University of Porto, located at 40° 59' 57" N, 8° 13' 52" W, in Espiunca, 70 km away from Porto, Portugal, [50].

[2]OSRA, located at 52.286° N, 13.135° E, in Tremsdorf, 15 km south-east of Potsdam, Germany. http://www.aip.de/groups/osra/

[3]ARTEMIS, located at 38° 49' N, 22° 41' E, in Thermopylae, Greece. http://www.cc.uoa.gr/artemis/

[4]NRH, located at 47°N, 02° E, near Meudon, France. http://www.obs-nancay.fr/

No.	dd-Mon-yyyy	jet position	SXT jet time, UT	radio burst time, UT[i)]	reference
1	13–Nov–1992	AR 7335	12:13:12[1)]	12:12:43	[5]
2a	18–Aug–1992		13:01:45	13:00:45	[81]
2b	18–Aug–1992		13:01:45	13:00:50	[81]
3	20–Jun–1992		22:29:10		[45]
4	16–Aug–1992	AR 7260	12:37:28[1)]	12:37:50	[43]
5	06–Dec–1991	AR 6958	11:42:30	11:40:38	[84]
6	21–Apr–1992	AR 7138	11:44:02	11:48:05	[84]
7a	10–Sep–1994	AR 7773	$\sim$10:24[max)]	10:26:51	[85]
7b	10–Sep–1994	AR 7773	$\sim$10:24[max)]	10:27:01	[85]
8	26–Sep–1992	AR 7296	09:50		[44]
9	07–Aug–1998	AR 8293	15:16:51[*)]	15:16:51[g)]	[40]

Table 4.1: Reports on: date, jet position on the solar disk (AR number), time in UT, together with the time of the associated metric radio bursts. The superscripts notate, correspondingly: [i)] initial time of the jet or radio burst; [1)] time of the first available image of the jet; [max)] time of estimated maximum of the jet; [*)] TRACE image at 171 Å; [g)] part of a group of type IIIs; if time is not explicitly classified, to be regarded as in case [1)].

when the jet (called anemone-type, Fig. 1.19) occurs near an area of predominantly open magnetic field lines, the electron beam follows these field lines and a type III radio burst is reported.

The physical parameters of the solar jets from the soft X-ray images, following the same enumeration as in Table 4.1, together with the corresponding type of the associated radio bursts, are gathered in Table 4.2. The so-reported values were taken into account while performing the numerical calculations, as shown in the next Section.

No.	$v_{\rm jet}^{\rm proj}$ $\rm km\,s^{-1}$	$T_{\rm jet}$ $\times 10^6$ K	$N_{\rm jet}$ $\times 10^9\,\rm cm^{-3}$	association, burst type	temporal delay	remarks
1	320			yes, U	65 s	$V_{\rm source} > 0.2c$
2a,b				yes, III&U		$V_{\rm source} \sim c/3$
3		5		?, III		
4	300	5.8 ± 1.5	0.6–1	yes, III	no	
5	250	1.5–3.5	1.3 ± 0.15	yes, III	> 4 min	
6	800	1.5–3.5	0.6 ± 0.35	yes, III	~ 1.5 min	
7a,b		1.8 ± 0.4		yes, III		
8, 9				yes, III		

Table 4.2: Available physical parameters of the soft X-ray jets from Table 4.1, and the corresponding types of the associated radio bursts.

4.2 Jet–plasma interaction

The interaction of the jet with the surrounding plasma is studied in the present Chapter. From observations is known that the jet consists of a hot plasma [102], thus a kinetic approach in terms of the Vlasov–Maxwell equations is much more appropriate than the multi-fluid approach (the latter was investigated in [67, 68]). The analysis of the interaction of the hot jet with the cold background plasma provides that such unstable configuration leads to excitation of electrostatic waves. Further on, the movement of an electron considered as a test particle in this growing electrostatic wave field is numerically treated, that results into an energizing and/or heating of these electrons. The settings for the jet and the electrons are done under typical coronal conditions. This mechanism can explain the occurrence of jet related type III metric radio bursts, as really observed (see Table 4.1), see also [72, 71].

4.2.1 Kinetic approach

A kinetic analysis is performed here, considering close relationship between plasma jets in the solar corona and a consequent acceleration of electrons. This analysis argue on the possibility of regarding the plasma jet as a trigger mechanism for the electron energization (heating or/and acceleration).

A collisionless plasma can be described by the well-known Vlasov–Maxwell equations, see e.g., [9, 42]. It is intended to study the interaction of a hot neutral plasma stream (jet) with the surrounding background plasma with the aim to search for a plasma wave excitation. That is usually done by a linear treatment of the Vlasov–Maxwell equations leading to a homogeneous system of equations

$$\varepsilon_{ij} E_j = 0 \tag{4.1}$$

with the dielectric tensor ε_{ij} [9, 42]. The determinant of the tensor ε_{ij} provides the dispersion relation of the different waves. Here, E_j denotes the components of the vector of the electric field accompanied by these plasma waves. The jet and the waves are assumed to propagate along the ambient magnetic field (chosen to be the z-direction). Since it is intended to look only for the excitation of electrostatic waves, the system of equations (4.1) can be reduced to

$$\varepsilon_{33}\, E_z = 0 \qquad \text{and} \quad \text{finally} \qquad \varepsilon_{33} = 0 \tag{4.2}$$

with

$$\varepsilon_{33} = 1 - 2\pi \sum_j \frac{\omega_{\mathrm{p}j}^2}{k^2} \int_{-\infty}^{\infty} dV_\parallel \int_0^{\infty} dV_\perp V_\perp \, \frac{k}{kV_\parallel - \omega} \, \frac{\partial f_j}{\partial V_\parallel} \tag{4.3}$$

with the wave number k and the frequency ω [9]. Here, each kind of particle j, with a charge q_j, a mass m_j, a temperature T_j, and a velocity distribution function f_j (normalized to unity), interacts with each other by electromagnetic forces. N_j and $\omega_{\mathrm{p}j} = (4\pi q_j^2 N_j / m_j)^{1/2}$ denote the number density of each kind of particles and its corresponding plasma frequency, respectively.

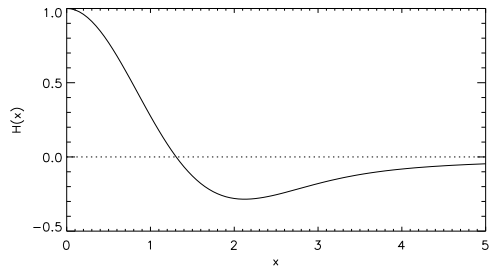

Figure 4.3: Numerical behavior of the function $H(\xi_j)$ (here $x \equiv \xi_j$).

Since a magnetized plasma is considered, the velocity distribution function f_j basically depends on the particle velocities parallel ($V_\parallel$) and perpendicular ($V_\perp$) to the ambient magnetic field, i.e., $f_j = f_j(V_\parallel, V_\perp)$. Here, the jet is regarded as propagating along the magnetic field lines, hence a drifting Maxwellian distribution is assumed for the velocity distribution function

$$f_j = \frac{1}{(2\pi v_{\mathrm{th},j}^2)^{3/2}}\, e^{-[(V_\parallel - V_{0,j})^2 + V_\perp^2]/2v_{\mathrm{th},j}^2} \tag{4.4}$$

with $v_{\mathrm{th},j} = (k_\mathrm{B} T_j/m_j)^{1/2}$, as the thermal velocity of the particle species j and $V_{0,j}$, as the drift velocity of the species j. Inserting the velocity distribution function (4.4) into Eq. (4.2) and performing the integrals, one gets the expression for the general dispersion relation of electrostatic waves

$$-k^2 = \sum_j \frac{\omega_{\mathrm{p}j}^2}{v_{\mathrm{th},j}^2}\, H(\xi_j), \tag{4.5}$$

with

$$\xi_j = \frac{V_\mathrm{ph} - V_{0,j}}{2^{1/2}\, v_{\mathrm{th},j}}. \tag{4.6}$$

The phase velocity is denoted with $V_\mathrm{ph} = \omega/k$ and the function $H(\xi_j)$ is given by

$$H(\xi_j) = 1 + \xi_j\, Z(\xi_j) \tag{4.7}$$

with the well-defined from [9] plasma dispersion function

$$Z(\xi_j) = \frac{1}{\pi^{1/2}} \int_{-\infty}^{+\infty} du\, \frac{e^{-u^2}}{u - \xi_j}.$$

The numerical behavior of the $H(\xi_j)$-function is shown on Fig. 4.3. The H-function changes its sign at $\xi_j = 1.3$, takes a global minimum of -0.2875 at $\xi_j = 2.1$, and finally tends to zero for $\xi_j \to \infty$ as seen on Fig. 4.3.

4.2.2 Electrostatic wave excitation due to the jet–plasma interaction

Now, the interaction of a hot plasma jet with the coronal background plasma is studied. Both, the jet and the background plasma are considered to be neutral. The jet is drifting with the velocity V_0 with respect to the background plasma. The electrons of the jet are considered to be hot, i.e., their temperature is $\theta\, T_0$ (with $\theta > 1$), whereas the protons of the jet have the same temperature as the protons of the background plasma, T_0. The number density of the jet electrons is νN_0 (with $0 < \nu < 1$), where $N_0 = 1.2 \times 10^9\,\mathrm{cm}^{-3}$ is the assumed value for the total number density of all electrons in the combined jet–background plasma system. It corresponds to the 300 MHz level, at which type III bursts are usually seen. Since a neutral plasma is considered, the same needs to be valid for the protons. Finally, the parameters of the jet (abbreviated with subscript 'j') are given by

$$\begin{aligned} V_{0\mathrm{j,e}} &= V_{0\mathrm{j,i}} = V_0 \\ T_{\mathrm{j,e}} &= \theta\, T_0 \quad \text{and} \quad T_{\mathrm{j,i}} = T_0 \\ N_{\mathrm{j,e}} &= N_{\mathrm{j,i}} = \nu N_0. \end{aligned}$$

In the case of the background plasma (denoted with subscript 'b'), the electrons and protons (with subscripts 'e' and 'i', correspondingly) have the temperature T_0, and their drift velocity is zero. Then, the background parameters can be fixed to be

$$\begin{aligned} V_{0\mathrm{b,e}} &= V_{0\mathrm{b,i}} = 0 \\ T_{\mathrm{b,e}} &= T_{\mathrm{b,i}} = T_0 \\ N_{\mathrm{b,e}} &= N_{\mathrm{b,i}} = (1-\nu) N_0. \end{aligned}$$

Here, the abbreviation for the jet/background plasma is given with the first lower index 'j/b', whereas the electrons/protons are denoted with the second lower index 'e/i', respectively.

Thus, the considered plasma configuration represents a four component plasma. The following normalization is now introduced (see also Chapter 2, Sect. 2.2),

$$\begin{aligned} \omega' &:= \frac{\omega}{\omega_{\mathrm{p0}}}, \qquad \omega_{\mathrm{p0}} = \left(\frac{4\pi e^2 N_0}{m_{\mathrm{e}}}\right)^{1/2}; \qquad q := k\lambda_{\mathrm{De}}, \qquad \lambda_{\mathrm{De}} = \frac{v_{\mathrm{th,e}}}{\omega_{\mathrm{p0}}}; \\ v_{\mathrm{ph}} &:= \frac{V_{\mathrm{ph}}}{v_{\mathrm{th,e}}}, \qquad v_{\mathrm{th,e}} = \left(\frac{k_{\mathrm{B}} T_0}{m_{\mathrm{e}}}\right)^{1/2}; \qquad v_0 := \frac{V_0}{v_{\mathrm{th,e}}}; \\ T'_{\mathrm{b,e/i}} &= T'_{\mathrm{j,i}} := 1, \qquad T'_{\mathrm{j,e}} := \theta; \qquad N'_{\mathrm{b,e/i}} := 1-\nu, \qquad N'_{\mathrm{j,e/i}} := \nu, \end{aligned}$$

where the quantities ω', q, v_{ph}, v_0, T' and N' are already dimensionless ones. Here, the spatial and temporal coordinates are normalized to the Debye length λ_{De} and the inverse plasma frequency $\omega_{\mathrm{p0}}^{-1}$, respectively. Consequently, all velocities are normalized with respect to the electron thermal one $v_{\mathrm{th,e}}$ (see Sect. 2.2 and Subsect. 2.3.2). Then, the dispersion relation (4.5) reduces to

$$-q^2 = (1-\nu) H(\xi_{\mathrm{b,e}}) + (1-\nu) H(\xi_{\mathrm{b,i}}) + \frac{\nu}{\theta} H(\xi_{\mathrm{j,e}}) + \nu H(\xi_{\mathrm{j,i}}), \tag{4.8}$$

where $\xi_{\mathrm{b,e}} = v_{\mathrm{ph}}/2^{1/2}$, $\xi_{\mathrm{b,i}} = v_{\mathrm{ph}}/(2\mu_{\mathrm{e}})^{1/2}$, $\xi_{\mathrm{j,e}} = (v_{\mathrm{ph}} - v_0)/(2\theta)^{1/2}$, $\xi_{\mathrm{j,i}} = (v_{\mathrm{ph}} - v_0)/(2\mu_{\mathrm{e}})^{1/2}$, are already normalized quantities and $\mu_{\mathrm{e}} = m_{\mathrm{e}}/m_{\mathrm{i}}$ is again the electron–proton mass ratio.

Since the jet speeds are in the range $V_0 = 10$–$1000\ \mathrm{km\,s^{-1}}$ [101], and the thermal electron velocity is $v_{\mathrm{th,e}} = 4600\ \mathrm{km\,s^{-1}}$ for a coronal temperature of $T_0 = 1.4 \times 10^6$ K, then the normalized jet velocity is in the range $v_0 \ll 1$. Therefore, the waves excited by the jet plasma interaction will have phase speeds that also are $v_{\mathrm{ph}} \ll 1$. That leads to $\xi_{\mathrm{b,e}}, \xi_{\mathrm{j,e}} \ll 1$ and, consequently, to $H(\xi_{\mathrm{b,e}}) \approx 1$ and $H(\xi_{\mathrm{j,e}}) \approx 1$. This is not in general valid for the ion parts, due to the presence of the factor μ_{e} in both denominators (of $\xi_{\mathrm{b,i}}$ and $\xi_{\mathrm{j,i}}$). In the case of a wave-like solution of Eq. (4.8), i.e., $q^2 > 0$, one needs to find for which condition the right-hand-side of Eq. (4.8) becomes negative. As already mentioned, the H-function, Eq. (4.3), has a global minimum of $H_{\min} = -0.2875$ at $\xi_j = 2.1$ (see Fig. 4.3). If the ion-parts are adjusted in such a way that their H-functions take $H_{\min}$, finally one gets the condition

$$(1-\nu) + \frac{\nu}{\theta} - 0.2875 < 0 \qquad \text{or} \qquad \nu > \frac{0.7125}{\theta - 1}\,\theta \tag{4.9}$$

for a wave-like solution. This condition should be fulfilled in the sense of a rough estimate. For example, if one has an upper limit for the parameter ν, Eq. (4.9) gives the lower limit for the other parameter θ. The condition $\nu = 1$ can be regarded as an upper limit, because then all particles are to be considered inside the jet, $N_{\mathrm{j}} = N_0$. In the other extreme, $\nu = 0$, all particles are in the background plasma and $N_{\mathrm{b}} = N_0$, i.e., no jet. The requirement $\nu \leq 1$ in Eq. (4.9) results in $\theta \geq 3.4783$. From observations, see also [102], one could estimate the upper temperature limit of the jet, i.e., $\theta \leq 5.71$, which leads to $\nu \geq 0.864$. Even higher value for the jet temperature was reported by [98], where the jet temperature was estimated to reach 10^7 K (or equivalently, $\theta = 7.1$ and hence $\nu = 0.829$). In general, only a jet with hot electrons is able to provide a wave-like solution of Eq. (4.8), but one needs to keep in mind the relation (4.9), which gives the limits of the constructed theoretical approach. Finally, the limits of the dimensionless quantities θ and ν are summarized below:

$$\begin{aligned} (7.1)\quad 5.71 \geq\ & \theta\ & \geq 3.4783 \\ (0.829)\quad 0.864 \leq\ & \nu\ & \leq 1 \end{aligned}$$

or in terms of physical quantities, the jet temperature and density need to be confined in the following ranges,

$$\begin{aligned} (10^7)\quad 8 \times 10^6 \geq\ & T_{\mathrm{jet}},\ \mathrm{K} & \geq 4.87 \times 10^6 \\ (0.995 \times 10^9)\quad 1.033 \times 10^9 \leq\ & N_{\mathrm{jet}},\ \mathrm{cm^{-3}} & \leq 1.2 \times 10^9 \end{aligned}$$

where the extreme observed case [98] is given in brackets.

For the numerical evaluation of Eq. (4.8), the jet parameters observed during the solar event on 28$^{\mathrm{th}}$ December 1993 [100] are adopted, namely jet speed of $532\,\mathrm{km\,s^{-1}}$ ($= 0.12\,v_{\mathrm{th,e}}$) and a temperature in the range of 7.4–8.2×10^6 K or $\theta = 5.28$–5.86. These parameters are typical ones. The relation (4.9) gives $\nu > 0.88$ (for $\theta = 5.28$). Bearing in mind the uncertainties for the reported observed physical parameters of the jets, $\theta = 5.5$ and $\nu = 0.9$ are taken for the numerical calculations further on. With the so-chosen parameters, Eq. (4.8) is calculated numerically using the procedure, described in [9], but adapted here for the ion-acoustic case.

Additionally, the jet velocity is set to have a value in the range $v_0 = \pm 0.45$ (in normalized quantities). Further on, it is assumed that the wave frequency is a complex quantity, i.e., sum of real ω and imaginary γ counterparts, namely $\omega_{\rm complex} = \omega + i\,\gamma$. In this sense, the solutions of Eq. (4.8) is plotted in terms of a $v_0(\omega)$-dependence, where the values of γ are given in colour code (from blue to green). When the imaginary part of the complex frequency (i.e., γ) is positive, the wave grows in time (given with yellow-green color on the plots). The case of negative γs gives the wave damping (with blue color, respectively). The task here is to look for electrostatic wave excitations, so the yellow-green areas on the $v_0(\omega)$-plots are to be of main interest.

As could be seen from Fig. 4.4, the numerical evaluation of Eq. (4.8) provides growth rates of the instability for jet speeds in the interval $0.09 < v_0 < 0.15$, i.e., in the range $414{-}690\ \mathrm{km\,s^{-1}}$, leading to an excitation of electrostatic waves up to frequencies of $0.01\,\omega_{\rm p0}$. These waves are of the ion-acoustic mode (see Chapter 2). The maximum of the growth rate $\gamma_{\rm max} = 0.00319\,\omega_{\rm p0}$ appears at a frequency $\omega = 0.00372\,\omega_{\rm p0}$.

Two additional runs were performed[5], using different set of jet's parameters, as could be seen on Figs. 4.5 and 4.6, namely with lower and higher jet temperature of $T_{\rm jet} = 5.87{\times}10^6\,\mathrm{K}$ and $T_{\rm jet} = 10^7\,\mathrm{K}$, respectively, in comparison with the first analysis. Some general trends

[5]The calculations resulting in Figs. 4.3–4.6 were done by means of a numerical code available at AIP.

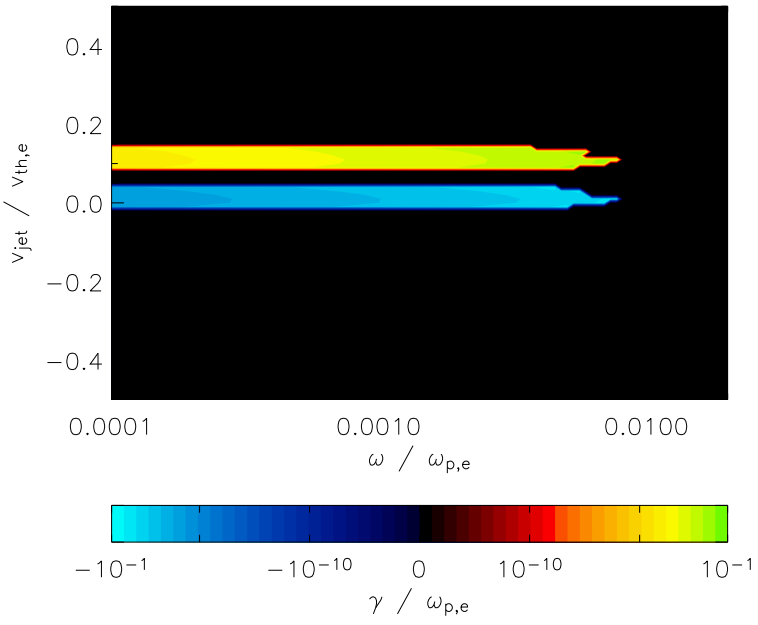

Figure 4.4: Jet velocity–real frequency plot, the imaginary part of the frequency is colour-coded, as given below the graphic. The parameters set is: $\theta = 5.5$ ($T_{\rm jet} = 7.7 \times 10^6\,\mathrm{K}$) and $\nu = 0.9$ (and $v_{\rm jet} \equiv v_0$).

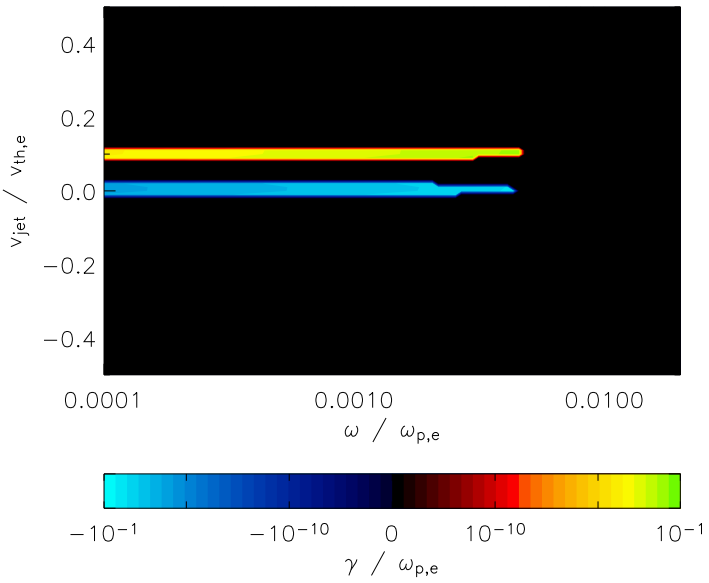

Figure 4.5: Jet velocity–real frequency plot for a parameter set: $\theta = 4.2$ ($T_{\rm jet} = 5.87 \times 10^6$ K) and $\nu = 0.95$.

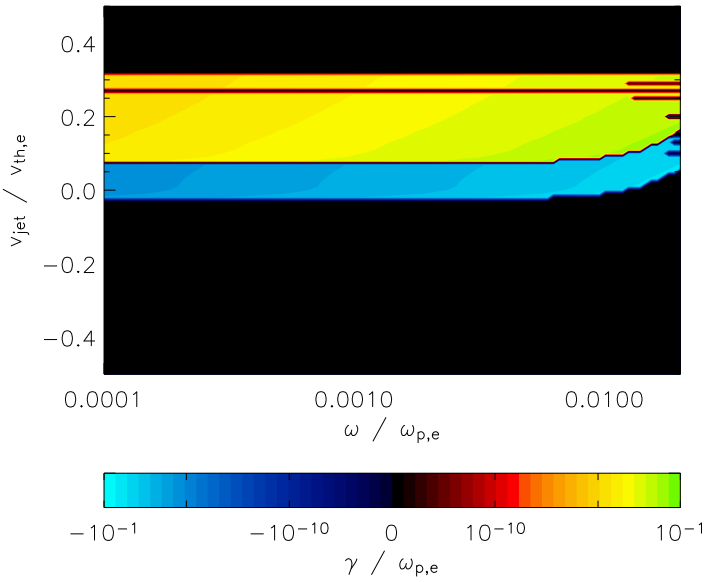

Figure 4.6: Jet velocity–real frequency plot for a parameter set: $\theta = 7.14$ ($T_{\rm jet} = 10^7$ K) and $\nu = 0.9$.

Fig.	θ	$T_{\rm jet}$, MK	ν	$N_{\rm jet}$, cm^{-3}	$\Delta\, v_{\rm jet}/v_{\rm th,e}$	$\Delta\, v_{\rm jet}$, km s^{-1}
4.5	4.2	5.87	0.95	1.14×10^{9}	0.08–0.11	368–506
4.4	5.5	7.7	0.9	1.08×10^{9}	0.09–0.15	414–690
4.6	7.14	10	0.9	0.96×10^{9}	0.075–0.25	345–1472

Table 4.3: Summary on the input/output parameters for the jet excited instability.

can be immediately noticed. Namely, simultaneously with the increasing of the parameter θ, the range of jet velocities for which the instability occurs, Δv_0, also increases (e.g., compare Fig. 4.4 and Fig. 4.6). It is easily to notice that the hotter jets allow growth of the instability for broader range of values of the jet velocities. Another important outcome confirms the θ–ν-constrain, namely, if one wants to obtain instability for much colder jets (for example with $T_{\rm jet} < 5.8\,$MK), it needs to consider that nearly all plasma particles are in the jets (i.e., $\nu > 0.95$ that becomes unrealistic) and the assumption for a four-component plasma becomes questionable! The values of all input and output parameters in these calculations are summarized in the Table 4.3.

In summary, the interaction of the jet with the background plasma leads to an instability for a small range of jet speeds, exciting electrostatic waves in the sense of the ion-acoustic mode. For example, in the case of a jet with temperature of 7.7 MK, this range is $415-690$ km s^{-1}. The electrostatic fluctuations represent localized spatial structures which grow in time. In order to see if such waves are able to accelerate electrons, one needs to follow the movement of an electron in this wave field. When the kinetic energy of the co-moving electron increases in time, the ability of such wave structure to energize electrons is proven. This is shown in details in the next Subsection.

4.2.3 Test electron movement in an oscillatory electrostatic field

In this Subsection, the movement of an electron in a given electrostatic wave field is studied. The wave field results from the jet–plasma interaction, as discussed in the previous Subsection. Here, the electron is generally considered to be a test particle, i.e., only one electron is taken into account in the numerical analysis.

The equation of motion of a test electron in an electrostatic field is usually given by

$$\frac{{\rm d}p}{{\rm d}t} = -eE = e\frac{\partial\varphi}{\partial x}, \tag{4.10}$$

with the electrostatic potential φ, the momentum $p = m_{\rm e}v/(1-\beta^2)^{1/2}$, and particle velocity v ($\beta = v/c$; c, velocity of light). Introducing dimensionless quantities,

$$t' := \omega_{\rm p0}\, t, \quad x' := x/\lambda_{\rm De}, \quad \phi := \varphi/(k_{\rm B}T_0/e).$$

and dropping the primes henceforth, the equation of motion is transformed into the normalized one:

$$\frac{1}{\beta_{\rm th}}\,\frac{1}{(1-\beta^2)^{3/2}}\,\frac{{\rm d}\beta}{{\rm d}t} = \frac{\partial\phi}{\partial x}, \tag{4.11}$$

with $\beta_{\rm th} = V_{\rm th,e}/c$. Additionally, the definition of the velocity $v = {\rm d}x/{\rm d}t$, i.e.,

$$\frac{{\rm d}x}{{\rm d}t} = \frac{\beta}{\beta_{\rm th}} \tag{4.12}$$

in normalized quantities, must be added, in order to complete the system of equations for describing the test particle motion. The ansatz

$$\phi = \phi_0 \, e^{\gamma \, t} \cos[q \, x(t) - \omega \, t] \tag{4.13}$$

is adopted for the spatial–temporal behavior of the electrostatic potential. Here, the same normalization has been employed. The electrostatic fluctuations are generated by the instability appearing due to the jet–plasma interaction (as found in the previous Section). Since the conditions of maximum growth rate should be used, $\gamma = 0.00319$, $\omega = 0.00372$, and $q = 0.05$ are chosen. At the thermal, i.e., undisturbed level, the amplitude of the electrostatic (ion-acoustic) fluctuations can be assumed to be about $k_{\rm B}T_0$ ($k_{\rm B}T_0 = 0.12\,{\rm keV}$ for $T_0 = 1.4 \times 10^6\,{\rm K}$), or $\phi_0 = 1$ in normalized quantities. The normalized equations of motion, (4.11) and (4.12), have been numerically solved with the choice of these parameters. Since the electron is regarded as a test particle, it must be collisionless with respect to Coulomb collisions. To be sure concerning this subject, the initial velocity of the electron is chosen to be 4 times the thermal one, i.e., $\beta_0 = 0.0613$ in normalized quantities [22]. It corresponds to a kinetic energy of about 1 keV. In summary, the initial conditions are $x(t = 0) = 0$ and $\dot{x}(t = 0) = 4$ in the sense of normalized quantities. The resulted movement in the x–t plane is presented in Fig. 4.7.

As seen from Fig. 4.7, the electron is initially moving with a nearly constant velocity until t $\approx$ 650 in the initial phase. Then, its motion is dramatically changed into a much more slower one superimposed by an oscillatory motion with a frequency increasing with time.

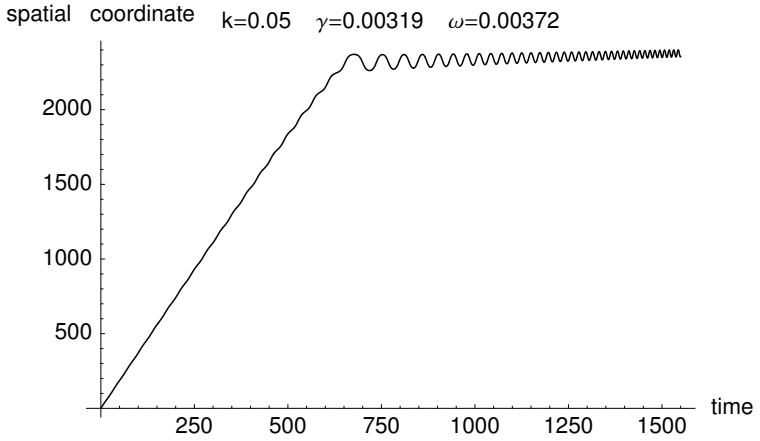

Figure 4.7: Co-movement of the test electron with the electrostatic wave.

That can be explained in the following manner:

Initially, the amplitude of the electrostatic wave is small, see Eq. (4.13), so that its influence on the electron motion can be neglected. Then, the electron continuously propagates with a constant velocity of β_0. Since the amplitude of the electrostatic field is increasing with time t, its influence on the particle motion will become essential, if the potential energy of the particle in the electrostatic wave, $\phi_0\, e^{\gamma t}$, is comparable with the kinetic energy of the particle, $W/(k_\mathrm{B}T_0)$, i.e.

$$\frac{W}{k_\mathrm{B}T_0} \equiv \frac{1}{\beta_\mathrm{th}^2}\left[\frac{1}{\sqrt{1-\beta^2}} - 1\right] := \phi_0\, e^{\gamma t}. \tag{4.14}$$

That state is reached after the time

$$t = \frac{1}{\gamma}\,\ln\left(\frac{W}{k_\mathrm{B}T_0}\cdot\frac{1}{\phi_0}\right) \tag{4.15}$$

The kinetic energy, corresponding to $\beta_0 = 4\,V_\mathrm{th,e}/c = 0.0613$ (the minimal speed for the electrons to be regarded as collisionless) and $\beta_\mathrm{th} = 0.015$, is $W_0/k_\mathrm{B}T_0 = 8$. Setting this values in Eq. (4.15), one gets $t_0 = 652$, as in agreement with the (exact) numerical solution on Fig. 4.7. After this time the electrostatic field dramatically changes the particle movement. Namely, the particle starts to co-move with the electrostatic wave, i.e., its averaged velocity is the phase speed of the wave, as depicted in Fig. 4.7. An oscillatory motion with temporally increasing frequency is superimposed upon this slow co-motion with the wave.

That can be demonstrated in the following way: Inserting the Ansatz (4.13) into Eq. (4.11) one gets

$$\frac{1}{\beta_\mathrm{th}}\,\frac{\mathrm{d}\beta}{\mathrm{d}t} = -q\,\phi_0\, e^{\gamma t}\,\sin[q\,x(t) - \omega t] \tag{4.16}$$

in the non-relativistic approach (i.e., $\beta \ll 1$). In the case of the co-motion with the wave, the function $x(t)$ can be expressed by

$$x(t) = v_\mathrm{ph}^* t + \delta x + x_0 \tag{4.17}$$

with $v_\mathrm{ph}^* = \omega/q$ as the phase velocity of the wave, δx as the oscillatory motion superimposed on the slowly translatory motion, and x_0 as the initial spatial displacement. Inserting the expression (4.17) into Eq. (4.16) and using Eq. (4.12) one obtains

$$\frac{\mathrm{d}^2\delta x}{\mathrm{d}t^2} = -q\phi_0\, e^{\gamma t}\,\sin[q\,\delta x + q\,x_0]. \tag{4.18}$$

Since the oscillatory motion has small amplitudes, $q\,\delta x \ll 1$ should be assumed, leading to

$$\sin[q\,\delta x + q\,x_0] = q\,\delta x\,\cos[q\,x_0] + \sin[q\,x_0].$$

Then, Eq. (4.18) reduces to

$$\frac{\mathrm{d}^2\delta x}{\mathrm{d}t^2} + \varpi^2\delta x = -q\,\phi_0\, e^{\gamma t}\,\sin[qx_0] \tag{4.19}$$

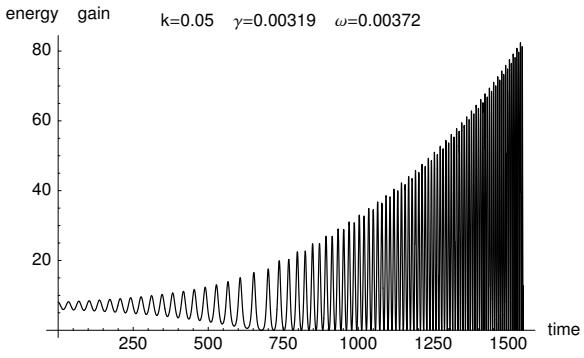

Figure 4.8: Energy gain of the test electron with the time, calculated from Eq. (4.14) for the kinetic energy, taking into account Eqs. (4.11), (4.12) and the initial conditions.

with $\varpi^2 = q^2\phi_0 \exp(\gamma t)\cos[qx_0]$. Equation (4.19) actually represents an equation of an oscillatory motion with the frequency ϖ, which increases with time. That can be really observed on Fig. 4.7. Adopting the parameters used in the numerical solution of the Eqs. (4.11) and (4.12), one finds a period of $2\pi/\varpi = 35$ at $t = 800$ for the oscillatory motion. This value is similar to that deduced from the numerical calculations as depicted in Fig. 4.7. It should be emphasized that a total agreement between the analytical approach and the numerical solution should not be expected since the numerical result (Fig. 4.7) is the exact one, whereas the analytical treatment presented above is only an approximative approach. It, however, demonstrates the important appearance of an oscillatory motion with a temporally increasing frequency during the co-motion of the electron with the wave.

While co-moving with the wave, the electron obtains an energy from the electrostatic wave (Fig. 4.8)[6]. The particle gets an energy of 80 $k_\mathrm{B}T_0$ within a period of $\approx 1\,600/\omega_{\mathrm{p}0}$, i.e., corresponding to an energy of 10 keV within 0.85 μs for $\omega_{\mathrm{p}0} = 2\pi \times 300$ MHz, for instance.

4.3 Discussion

During magnetic reconnection, which is one possible process of solar flares, jets of hot plasma are ejected from the reconnection site into the surrounding coronal plasma. The interaction of such jets with background plasma leads to the excitation of electrostatic waves due to an instability, if the jet speed is for example in the range 415–690 $\mathrm{km\,s^{-1}}$ for a jet's electron temperature of 7.7 MK. Such values for the jet speed are typical ones, as observed in the soft X-ray images by *Yohkoh* [101, 102].

If the jet moves through the surrounding coronal plasma, it is decelerated due to Coulomb collisions within a period of the order of the Coulomb collision time t_{Cc}, which is given by

$$t_{\mathrm{Cc}} = \frac{1}{\omega_{\mathrm{pe}}} \frac{4\pi\lambda_{\mathrm{De}}^3 N_\mathrm{e}}{\ln\Lambda}, \tag{4.20}$$

[6]Figs. 4.7 and 4.8 were computed with the *Mathematica* software package.

with $\Lambda = 4\pi\lambda_{\mathrm{De}}^3 N_{\mathrm{e}}$ [9, 22]. At the 300 MHz level and a coronal temperature of 1.4×10^6 K, one gets $N_{\mathrm{e}} = 1.12 \times 10^9\,\mathrm{cm}^{-3}$ and $\lambda_{\mathrm{De}} = 0.244\,\mathrm{cm}$ resulting in $t_{\mathrm{Cc}} = 10^7/\omega_{\mathrm{p0}}$. In comparison, the growing time t_{growing} for the excitation of electrostatic waves is given by $t_{\mathrm{growing}} = \gamma^{-1}/\omega_{\mathrm{p0}} = 313/\omega_{\mathrm{p0}}$ for $\gamma = 0.00319$. Thus, the instability acts much faster than the deceleration of the jet due to Coulomb collisions.

As discussed in this Chapter, the plasma stream ejected from the reconnection site passes through the surrounding coronal plasma leading to the excitation of electrostatic fluctuations in terms of the ion-acoustic mode. If these fluctuations act on supra-thermal (i.e., collisionless free) electrons, these electrons co-move with the wave (Fig. 4.7) and gain energy (Fig. 4.8). That process represents a collisionless energizing and/or heating of the electrons during flares. It is well-known that electrons are rapidly heated and energized in a collisionless manner during flares [48, 49]. That is impressively seen in the hard X-ray emission of the flaring plasma as observed by the spacecraft RHESSI [49], for instance.

Since the instability only appears in a small range of the jet speed (Fig. 4.4), the enhanced level of electrostatic fluctuations is localized in a small spatial region in the corona. Consequently, if the energized electrons leave the region of instability, some of them can run away with a high velocity along a magnetic field line. That leads to either solar type III or type U radio bursts due to their propagation along open and closed magnetic field lines (see Fig. 4.2 for example), respectively.

The observations show that there are generally three kinds of events:

i. jets that are not accompanied by type III bursts,

ii. jets with a simultaneous appearance of type III bursts,

iii. jets accompanied with type III bursts, but with a temporal delay concerning the jet onset time.

They can be explained in the framework of our approach, summarized in [71]. Since the instability only occurs in a small range of the jet speed around V_0, jets with a speed smaller than V_0 do not give rise to an electrostatic instability and, hence, to type III bursts (case i). On the other hand, if the jet speed is greater than V_0, it is initially not able to excite electrostatic fluctuations. However, the jet is decelerating due to its interaction with the surrounding plasma, e.g., due to Coulomb collisions. Then, it needs time until the jet speed slows down to V_0 leading to the onset of the electrostatic instability and, consequently, to the occurrence of type III radio bursts (case iii). That could be the reason of the observed delay between the onset of the jet and that of the type III burst, [5, 84]. Only in the special case, at which the jet speed is very close to V_0, the type III radio bursts can simultaneously appear with the jet (case ii), [43].

In summary, the interaction of a solar jet ejected from the reconnection site with the surrounding plasma leads to both the collisionless energizing and/or heating of electrons (as seen in the hard X-ray emission) and to type III bursts (as observed in the solar radio emission during flares). Here, the kinetic energy of the jet is partly transfered into energy of electrostatic fluctuations and, subsequently, into the energy of the electrons. This process represents an electron acceleration at a localized wave structure in the solar corona.

Chapter 5

Electron acceleration at coronal shock waves with attached whistler packets

5.1 Observational background

In the solar corona, shock waves can be generated either by blast waves due to the flare process [115, 118] and/or by coronal mass ejections (CMEs) [104, 105, 27, 16, 46, 26]. It should be emphasized, that a shock wave is a discontinuity accompanied with an increase of the entropy. The jump of the density, temperature, and magnetic field across the shock is governed by the Rankine–Hugoniot relationships [83], i.e., the shock itself and the processes immediately associated with it should be considered independently from its exciter.

Coronal shock waves can be observed as type II bursts in the solar radio radiation [123, 115]. As introduced in Sect. 1.4, a type II radio burst can morphologically be divided into two types of emission in its dynamic radio spectrum: the 'backbone' (Fig. 1.13) and the 'herringbone' (Fig. 1.14) emission. The so-called backbone emission is slowly drifting from high to low frequencies with a typical drift rate of about $-0.1375\,\mathrm{MHz\,s^{-1}}$ at 55 MHz [58] and shows often a fundamental–harmonic structure. It is widely accepted to be the radio signature of a shock wave traveling through the corona [74, 51, 2, 52]. Sometimes, very fast drifting patches of emission (see Fig. 1.14) can be seen to emanate from the backbone, toward both lower or higher frequencies with typical drift rates of about $\pm 7.2\,\mathrm{MHz\,s^{-1}}$ at 55 MHz [58]. These features are the so-called herringbone emission, regarded as the radio signature of shock-accelerated electrons [14, 126, 59]. According to the interpretation of a dynamic radio spectrum (see Subsect. 1.4.1) the 55 MHz plasma level is located at a distance of 1.63 $R_\odot$ from the center of the Sun, i.e., in a height of about 450 Mm above the photosphere, if a two-fold Newkirk [75] model is used, see Sect. 1.4 (the choice of $\alpha = 2$ in Eq. (1.2) is appropriate for type II burst sources [55]). At this height, a magnetic field strength of 1 G is expected according Eq. (1.3) [21]. That provides for $\omega_{\mathrm{pe}} = 2\pi \times 55\,\mathrm{MHz}$, the electron cyclotron frequency to be $\omega_{\mathrm{ce}} = 1.76 \times 10^7\,\mathrm{s^{-1}}$, the ratio $\omega_{\mathrm{pe}}/\omega_{\mathrm{ce}} = 20$, the Alfvén speed to be $v_{\mathrm{A}} = 360\,\mathrm{km\,s^{-1}}$, and the plasma beta to be 0.36, if an usual coronal

temperature of 1.4×10^6 K is adopted (see Table 1.1). Assuming the same density model [75], the velocities related to the backbone V_{BB} and herringbone emission V_{HB} are estimated to be 1000 km s^{-1} and 50 000 km s^{-1} ($= 0.17c$, corresponding to a kinetic energy of 7.3 keV), respectively. Since the backbone is associated with the shock traveling through the corona, coronal shock waves have typical Alfvén Mach numbers ($M_{\mathrm{A}} = V_{\mathrm{BB}}/v_{\mathrm{A}}$) of 2.76. Such shocks can be considered to be super-critical [38, 55] under coronal conditions.

Holman and Pesses [32] proposed, that the electrons associated with the herringbones are generated by shock-drift acceleration. Further studies on this subject show that, this mechanism provides a beam-like distribution function for the accelerated electrons [59], that corresponds well to the observed characteristics of the herringbone emission stripes. The beam has a velocity parallel to the ambient magnetic field

$$V_{\mathrm{beam}} = V_{\mathrm{sh}} \sec\theta_{\mathrm{B,n}} \left(1 + \cos^2 \alpha_{\mathrm{lc}}\right) \tag{5.1}$$

with V_{sh} as the shock speed [59], and $\theta_{\mathrm{B,n}}$ denotes the angle between the upstream magnetic field and the shock normal. The loss-cone angle α_{lc} is defined by the jump of the magnetic field across the shock, i.e., $\alpha_{\mathrm{lc}} = \arcsin[(B_{\mathrm{up}}/B_{\mathrm{down}})^{1/2}]$ with B_{up} and B_{down} as the magnetic field in the up- and downstream region, respectively. If we apply the shock-drift acceleration as a mechanism for electron acceleration in the case of herringbone emission, we need to take into account the values from the observed drift rates, i.e., $V_{\mathrm{beam}} = V_{\mathrm{HB}} = 50\,000\,\mathrm{km\,s^{-1}}$ and $V_{\mathrm{sh}} = V_{\mathrm{BB}} = 1000\,\mathrm{km\,s^{-1}}$. Assuming for the jump of the magnetic field across the shock $B_{\mathrm{down}}/B_{\mathrm{up}} = 2$, i.e., $\alpha_{\mathrm{lc}} = 45°$, Eq. (5.1) provides $\theta_{\mathrm{B,n}} = 88.28°$. This result shows, that shock-drift acceleration is an efficient mechanism for electron acceleration under coronal circumstances only for nearly perpendicular shocks.

However, considering this mechanism for the herringbone emission, a nearly perpendicular shock configuration is required to be present during the whole event. For the example shown in Fig. 1.14, the type II burst appears for about 2 minutes, i.e., it would cover a spatial scale in the corona of about 120 Mm for a source velocity of 1000 km s^{-1}. Hence, despite that the shock-drift acceleration is able to explain the electron acceleration rates, the physical conditions required for this mechanism to work are difficult to sustain, since the shock travels more than 100 Mm and needs to be nearly perpendicular all the time. That is an event with low probability. Thus, there is a need for another mechanism for electron acceleration at coronal shocks. This new mechanism should avoid the restriction of a nearly perpendicular shock geometry. That is the purpose of this Chapter.

Spacecraft observation of the Earth's bow shock, interplanetary shocks, and shocks related with co-rotating interaction regions (CIRs), are the only possibility for in-situ measurements of shocks in space plasmas. Observations of the spacecraft *Ulysses* at CIR-related shocks reveal, that electrons are really accelerated up to 0.1–0.4 MeV at such shocks (see top panel of Fig. 5.1). CIR related shocks are efficient to accelerate particles when the conditions $M_{\mathrm{A}} > 2.5$ and $50° < \theta_{\mathrm{B,n}} < 80°$ are simultaneously fulfilled by the shock waves, [18]. Such shocks can be regarded as super-critical shocks [38] and are usually associated with whistler waves in the up- and downstream region [29, 17, 54]. These quasi-perpendicular and super-critical shocks with attached whistler waves preferably generate energetic electrons.

In summary, the aim of the present Chapter is to look for a new mechanism for electron

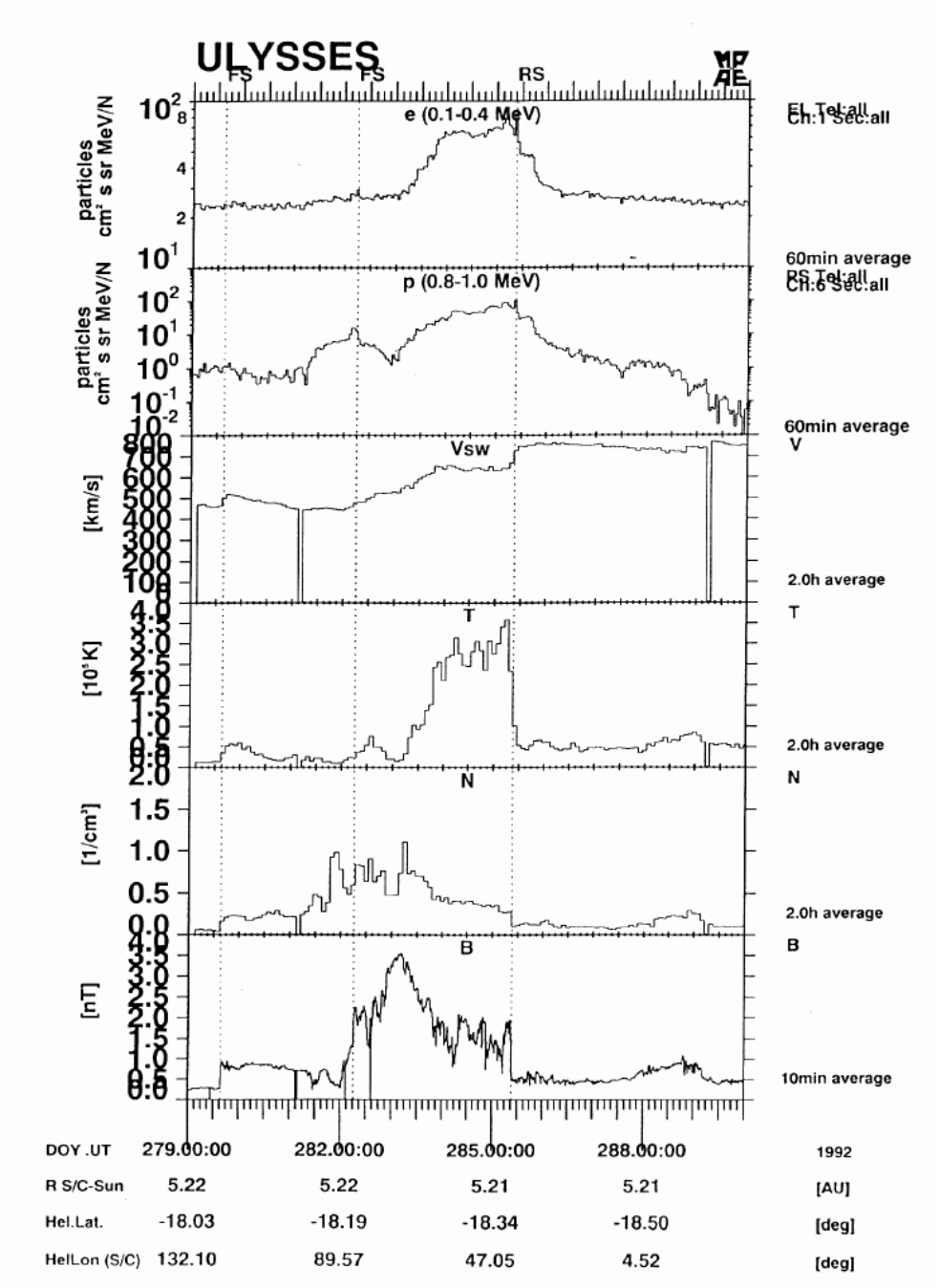

Figure 5.1: Behaviour of the fluxes of energetic electrons (0.1−0.4 MeV) and protons (0.8–1.0 MeV), the solar wind speed V_{SW}, the proton temperature, the proton number density, and the magnitude of the magnetic field (from top to bottom) during the crossing of a CIR by *Ulysses* [90].

acceleration at quasi-perpendicular shocks in the solar corona. Motivated by the observations at CIR related shocks, we consider an electron–whistler–shock interaction. Here, it is basically assumed that the same physical processes for the collisionless shocks in space (e.g., at CIRs), are also true for the coronal shock waves.

5.2 The model

The model presented here considers the following scenario (schematically shown on Fig. 5.2). A shock wave is moving through the solar atmosphere with a velocity of about $1000\,\mathrm{km\,s^{-1}}$. The in-flowing protons (i.e., toward the shock) can be successfully accelerated by reflection at the shock (see Subsect. 5.2.1). Due to their relatively slow thermal velocity (of the order of $110\,\mathrm{km\,s^{-1}}$ for a typical coronal temperature of 1.4 MK), the quasi-perpendicular configuration with $\theta_{\mathrm{B,n}} = 70°$, as a typical value for instance, is sufficient for a substantial velocity gain of the protons of about $6000\,\mathrm{km\,s^{-1}}$. (A quasi-perpendicular configuration is one for which $45° < \theta_{\mathrm{B,n}} < 90°$, so that $\theta_{\mathrm{B,n}} = 70°$ is roughly a mean value.) The protons are accelerated and reflected at the shock back to the upstream region, where they are able to excite whistler waves by resonant wave–particle interaction (see Subsect. 5.2.2). These so-excited whistlers can interact only with the in-flowing electrons, that fulfill the resonance condition. These electrons are accelerated (i.e., gain energy) in the whistler electric field (see Subsect. 5.2.3). Consequently, the perpendicular electron velocity component with respect to the ambient magnetic field is increasing during this resonant interaction. That also leads to an increase of its magnetic moment. Simultaneously with this process, the accelerating electrons are moving toward the shock front. Since the shock is accompanied by a jump of the magnetic field, it represents a traveling magnetic mirror (see Subsect. 5.2.4). Finally, the electrons are mirror-reflected at the shock and propagate into the upstream region. The

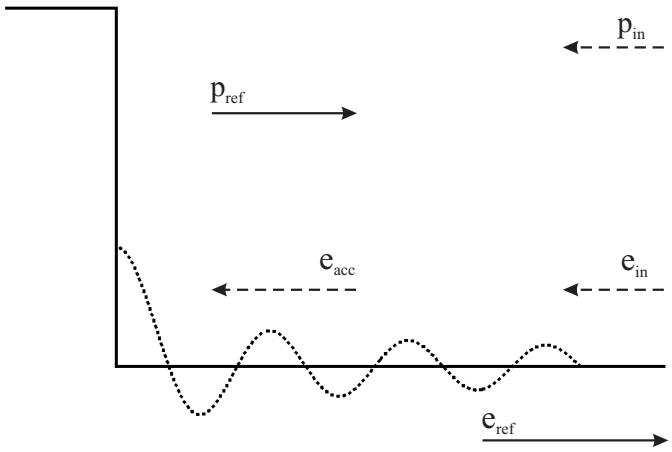

Figure 5.2: Sketch of a shock ramp (with solid lines) with attached whistler wave (dotted curves), propagating to the right (chosen as the positive direction). The in-flowing proton ('p') and electron ('e') are denoted with subscript 'in', the out-flowing, with subscript 'ref', and the accelerated electrons with 'acc'.

out-flowing electrons (i.e., away from the shock) do not fulfill the resonance condition and, hence, are not in resonance with the whistler wave. Then, they can travel undisturbed into the far upstream region, and be detected as herringbone emission, for example.

5.2.1 Inflow of the upstream protons and their acceleration

It is well-known from observations at Earth's bow shock [78, 80], that protons are reflected and accelerated by nearly conserving their magnetic moment at the quasi-perpendicular region of Earth's bow shock. The proton (denoted with superscript 'i') velocity gain parallel to the upstream magnetic field can be expressed by

$$V^{\mathrm{i}}_{\parallel,\mathrm{ref}} = 2V_{\mathrm{sh}} \sec\theta_{\mathrm{B,n}} - V^{\mathrm{i}}_{\parallel,\mathrm{in}} \tag{5.2}$$

[78, 32], where the subscript 'in' denotes the initial velocity of the particle and 'ref', the reflected one, correspondingly.

For the protons in the initial state in the upstream region a Maxwellian distribution normalized to unity is assumed

$$f_{\mathrm{i}}(V) = \frac{1}{(2\pi V^2_{\mathrm{th,i}})^{1/2}}\, \mathrm{e}^{-V^2/(2V^2_{\mathrm{th,i}})},$$

with a proton thermal velocity $V_{\mathrm{th,i}} = (k_{\mathrm{B}}T/m_{\mathrm{i}})^{1/2}$ (k_{B}, Boltzmann's constant; T, temperature; m_{i}, proton mass). Then, the numbers of particles with velocities parallel to the ambient magnetic field in the range $-V_u < V^{\mathrm{i}}_{\parallel,\mathrm{in}} < V_u$ is given by

$$\frac{N(V_u)}{N_0} = \frac{2\pi}{(2\pi V^2_{\mathrm{th,i}})^{3/2}} \int_{-V_u}^{V_u} \mathrm{d}V_{\parallel} \int_0^{\infty} \mathrm{e}^{-(V^2_{\parallel}+V^2_{\perp})/(2V^2_{\mathrm{th,i}})} V_{\perp} dV_{\perp} = 2\Phi(V_u/V_{\mathrm{th,i}}) \tag{5.3}$$

with

$$\Phi(V_u/V_{\mathrm{th,i}}) = \frac{1}{(2\pi)^{1/2}} \int_0^{V_u/V_{\mathrm{th,i}}} \mathrm{e}^{-t^2/2}\mathrm{d}t. \tag{5.4}$$

Equation (5.3) provides that 99% of all protons have velocities parallel to the ambient magnetic field in the range,

$$-2.576\, V_{\mathrm{th,i}} \le V^{\mathrm{i}}_{\parallel,\mathrm{in}} \le 2.576\, V_{\mathrm{th,i}} \qquad \text{or} \qquad -277 \le V^{\mathrm{i}}_{\parallel,\mathrm{in}} \le 277,\ \mathrm{km\,s^{-1}},$$

where for the thermal velocity of the protons was used the value of $V_{\mathrm{th,i}} = 107.5\,\mathrm{km\,s^{-1}}$ for a coronal temperature of $T = 1.4\,\mathrm{MK}$. Note that such a value is essentially smaller than the shock speed, which is $1000\,\mathrm{km\,s^{-1}}$. Since 99% of all initial protons have velocities parallel to the ambient magnetic field in the above given range, $V_{\mathrm{sh}} = 1000\,\mathrm{km\,s^{-1}}$ and $\theta_{\mathrm{B,n}} = 70°$, the substitution of these values in Eq. (5.2) will give the final speed of the main part of the reflected proton to be in the range

$$5571 < V^{\mathrm{i}}_{\parallel,\mathrm{ref}} < 6125, \mathrm{km\,s^{-1}} \qquad \text{or} \qquad 0.0186 < \beta^{\mathrm{i}}_{\parallel} = V^{\mathrm{i}}_{\parallel,\mathrm{ref}}/c < 0.0204.$$

Here, the shock propagation is chosen to be in the positive direction, and the reflected and accelerated protons are moving in the same direction, i.e., away from the shock. That demonstrates that the protons get a substantial gain of energy due to the encounter with the quasi-perpendicular coronal shock wave.

5.2.2 Whistler excitation

In order to excite whistler waves by wave–particle interaction in the case of the accelerated protons, they need to fulfill the resonance condition, see [9, 42],

$$k\,c\,\beta_{\parallel}^{\mathrm{i}} - \omega - \omega_{\mathrm{ci}} = 0, \tag{5.5}$$

where k, ω, and ω_{ci} are the wave number, the wave frequency, and the proton cyclotron frequency, respectively. Because whistler waves are predominantly excited along the magnetic field [116], the whistler waves propagating parallel to the ambient magnetic field are considered here (see Subsect. 2.3.1), namely

$$\frac{k^2c^2}{\omega^2} = 1 + \frac{\omega_{\mathrm{pe}}^2}{\omega(\omega_{\mathrm{ce}} - \omega)}, \tag{5.6}$$

in the case of $\omega \gg \omega_{\mathrm{ci}}$. Now, the following normalization (see Sect. 2.2) is introduced for the wave number $k' = k\,c/\omega_{\mathrm{pe}}$ and the frequency $\omega' = \omega/\omega_{\mathrm{ce}}$, correspondingly. Here, the primed quantities are already dimensionless. Substituting these expressions back into the Eq. (5.5) we obtain the normalized ion resonance condition, namely,

$$S\,k'\,\beta_{\parallel}^{\mathrm{i}} - \omega' - \mu_{\mathrm{e}} = 0, \tag{5.7}$$

with $S = \omega_{\mathrm{pe}}/\omega_{\mathrm{ce}}$ and μ_{e} as the electron to proton mass ratio (that is neglected further on). In the case of a coronal plasma at the 55 MHz-level, the frequency ratio is estimated to be $S = 20$ (see Table 1.1). Because of $S \gg 1$, the normalized dispersion relation for the whistler waves is found to be, see Eq. (2.62),

$$k' = \sqrt{\frac{\omega'}{1-\omega'}}. \tag{5.8}$$

This relation is substituted into the normalized ion resonance condition (5.7) leading to

$$\beta_{\parallel}^{\mathrm{i}} = \frac{1}{S}\sqrt{\omega'(1-\omega')}. \tag{5.9}$$

In order to obtain an estimation for the frequencies of the excited whistlers, $0.0186 < \beta_{\parallel}^{\mathrm{i}} < 0.0204$ are employed for $\beta_{\parallel}^{\mathrm{i}}$ in Eq. (5.9) resulting in

$$0.165 < \omega' < 0.211 \qquad \text{or equivalently from Eq. (5.8),} \qquad 0.445 < k' < 0.518.$$

In summary, shock-accelerated protons are able to excite whistler waves with frequencies in the range (0.165–0.211) ω_{ce}. These whistlers are propagating away from the shock in the upstream region. From the resonance condition Eq. (5.5) one gets $\omega_{\mathrm{ci}} = k(V_{\parallel}^{\mathrm{i}} - V_{\mathrm{ph}})$ with the whistler phase velocity V_{ph}. Since the proton cyclotron frequency ω_{ci} is positive, the proton velocity is faster than the phase speed of the whistlers, so that the right-hand circularly polarized whistlers appear to be left-hand circularly polarized in the rest frame of the energetic protons. Thus, the shock accelerated protons do fulfill the resonance condition and the condition for providing the right whistler polarization, which is left-handed circularly polarized in the proton rest frame, but right-handed circularly polarized in the laboratory frame.

5.2.3 Resonant electron–whistler interaction

The so-excited whistler waves can resonantly interact with the electrons in the upstream region. The electron resonance conditions is given by

$$k\,c\,\beta_{\parallel}^{\mathrm{e}} - \omega + \omega_{\mathrm{ce}} = 0, \tag{5.10}$$

with $\beta_{\parallel}^{\mathrm{e}} = V_{\parallel}^{\mathrm{e}}/c$, see [9, 42]. The electron part is denoted with superscript 'e', again. Then, one gets

$$S\,k'\,\beta_{\parallel}^{\mathrm{e}} - \omega' + 1 = 0. \tag{5.11}$$

after the usual normalization (see Subsect. 2.2). Using again relation (5.8) for the normalized wave number, the equation above becomes

$$-\beta_{\parallel}^{\mathrm{e}} = \frac{1}{S}\sqrt{\frac{(1-\omega')^3}{\omega'}}. \tag{5.12}$$

With $S = 20$ and the ω'-range, $0.165 < \omega' < 0.211$, one gets finally that

$$-0.094 < \beta_{\parallel}^{\mathrm{e}} < -0.076 \quad \text{or} \quad -28\,200 \le V_{\parallel}^{\mathrm{e}} \le -22\,800, \mathrm{km\,s^{-1}}$$

or $-6.13\,V_{\mathrm{th,e}} \le V_{\parallel}^{\mathrm{e}} \le -4.96\,V_{\mathrm{th,e}}$, with $V_{\mathrm{th,e}} = 4600\,\mathrm{km\,s^{-1}}$. Thus, only counter-streaming (i.e., moving towards the shock) electrons are in resonance with the whistler waves.

In order to study relativistic electrons, one needs to correct the above result using the extended, relativistic resonance condition, i.e.,

$$k\,c\,\beta_{\parallel}^{\mathrm{e}} - \omega + \omega_{\mathrm{ce}}\left[1 - (\beta_{\parallel}^{\mathrm{e}})^2 - (\beta_{\perp}^{\mathrm{e}})^2\right]^{1/2} = 0, \tag{5.13}$$

see [9]. Employing the same normalization, the above equation becomes,

$$S\,k'\,\beta_{\parallel}^{\mathrm{e}} - \omega' + \left[1 - (\beta_{\parallel}^{\mathrm{e}})^2 - (\beta_{\perp}^{\mathrm{e}})^2\right]^{1/2} = 0. \tag{5.14}$$

Taking into account relation (5.8) for k', a quadratic equation for the parallel component of the electron velocity is obtained, namely

$$c_1\,(\beta_{\parallel}^{\mathrm{e}})^2 - c_2\,\beta_{\parallel}^{\mathrm{e}} + c_3 = 0, \tag{5.15}$$

with the coefficients, $c_1 = S^2\omega'/(1-\omega') + 1$, $c_2 = S\sqrt{\omega'^3/(1-\omega')}$ and $c_3 = (\beta_{\perp}^{\mathrm{e}})^2 + \omega'^2 - 1$. Setting a value for the S and ω', one can plot the relation (5.15) for $0 \le \beta_{\perp}^{\mathrm{e}} < 1$, as done on Fig. 5.3 in the ($\beta_{\parallel}^{\mathrm{e}}$–$\beta_{\perp}^{\mathrm{e}}$)-plane. There, one could see two curves, corresponding to the minimum (0.165) and the maximum (0.211) values of ω' (or to -0.094 and -0.076 in terms of $\beta_{\parallel}^{\mathrm{e}}$ at $\beta_{\perp}^{\mathrm{e}} = 0$, respectively). The curvature (as enhanced on the plot) is due to the relativistic effects, since in the non-relativistic case it would be two straight lines parallel to the $\beta_{\perp}^{\mathrm{e}}$-axis.

During the resonant interaction with the whistler wave field, the electron is increasing its

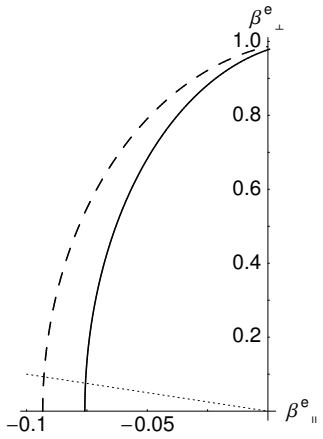

Figure 5.3: Resonance curves, plotted in the ($\beta^e_\parallel$–$\beta^e_\perp$)-plane, as solutions of Eq. (5.14) for: $S = 20$, $\omega' = 0.165$ (dashed line) and 0.211 (solid line). The dotted line corresponds to a pitch angle of 45°.

velocity component perpendicular to the magnetic field. That represents a motion upward in the the ($\beta^e_\parallel$–$\beta^e_\perp$)-plane between these curves, or in the so-called **'resonance band'** leading to an increase of its kinetic energy. Normalized to the rest energy (i.e., $m_0\,c^2 = 512\,\mathrm{keV}$), the kinetic energy of the electron is usually defined as

$$W'_{\mathrm{kin}} = \frac{W_{\mathrm{kin}}}{m_0\,c^2} = \frac{1}{\sqrt{1-\beta^2}} - 1 \tag{5.16}$$

with $\beta^2 = (\beta^e_\parallel)^2 + (\beta^e_\perp)^2$. Taking into account the relation (5.14), the kinetic energy (5.16) can be plotted[1] in terms of the perpendicular velocity component $\beta^e_\perp$, see Fig. 5.4. A substantial energy gain for the electrons can be noticed due to the resonant electron–whistler interaction.

Now, the movement of an electron in the whistler wave field is investigated. In general, the movement of an electron in given electric and magnetic fields can be described by

$$\frac{\mathrm{d}\mathbf{p}}{\mathrm{d}t} = -e\,[\mathbf{E} + \boldsymbol{\beta} \times \mathbf{B}]\,, \tag{5.17}$$

together with the kinematic equation,

$$\frac{\mathrm{d}\mathbf{r}}{\mathrm{d}t} = c\boldsymbol{\beta}, \tag{5.18}$$

with $\boldsymbol{\beta} = \mathbf{v}/c$. The momentum is defined by $\mathbf{p} = m_0\,c\boldsymbol{\beta}/\sqrt{1-\beta^2}$. In order to normalize the above equations of motion, the following dimensionless quantities are introduced (compare with Sect. 2.2): time, $t' = t\omega_{\mathrm{ce}}$; spatial coordinate, $r' = r\omega_{\mathrm{pe}}/c$; momentum, $p' = p/(m_0\,c)$; energy, $W'_{\mathrm{kin}} = W_{\mathrm{kin}}/(m_0\,c^2)$; the magnetic and electric fields are normalized

[1] All plots in this Chapter were computed with *Mathematica* software package.

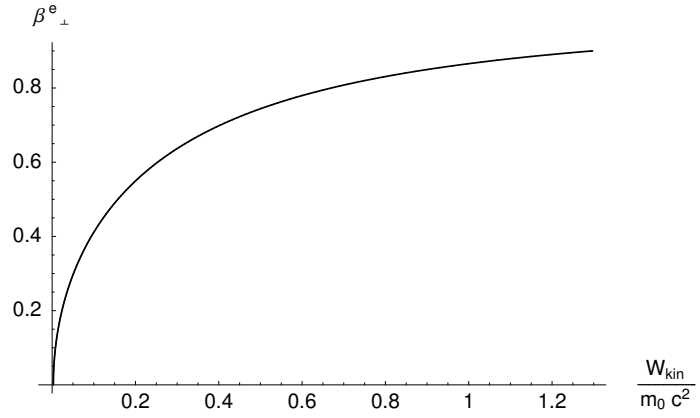

Figure 5.4: Relation between $\beta_\perp^{\mathrm{e}}$ and the kinetic energy $W_{\mathrm{kin}}/m_0\,c^2$, Eq. (5.16), where $\beta_\perp^{\mathrm{e}}$ is related to $\beta_\parallel^{\mathrm{e}}$ by the resonance curve, Eq. (5.14), for the case $\omega' = 0.211$ and $S = 20$ (see the solid line in Fig. 5.3).

to the background (upstream) magnetic field, B_0, and B_0/S, respectively. Substituting these normalizations into the above equations of motion, one gets the following normalized system of equations,

$$\frac{\mathrm{d}\mathbf{p}'}{\mathrm{d}t'} = -\mathbf{E}' - \boldsymbol{\beta} \times \mathbf{B}', \tag{5.19}$$

$$\frac{\mathrm{d}\mathbf{r}'}{\mathrm{d}t'} = S\,\boldsymbol{\beta}. \tag{5.20}$$

In order to find the energy gain, the time derivative of Eq. (5.16) is performed, i.e.,

$$\dot{W}'_{\mathrm{kin}} = \frac{\boldsymbol{\beta} \cdot \dot{\boldsymbol{\beta}}}{(1-\beta^2)^{3/2}}, \tag{5.21}$$

which gives the same result as a dot-product of Eq. (5.19) with $\boldsymbol{\beta}$, since Eq. (5.19) can be rewritten as

$$\frac{\mathrm{d}\mathbf{p}'}{\mathrm{d}t'} = \frac{\dot{\boldsymbol{\beta}}(1-\boldsymbol{\beta}^2) + (\boldsymbol{\beta}\cdot\dot{\boldsymbol{\beta}})\cdot\boldsymbol{\beta}}{(1-\boldsymbol{\beta}^2)^{3/2}} = -\mathbf{E}' - \boldsymbol{\beta} \times \mathbf{B}'.$$

Finally using the relation $\boldsymbol{\beta} = \mathbf{p}'/(1+p'^2)^{1/2}$, one obtains the following expression for the time derivative of the normalized kinetic energy,

$$\dot{W}'_{\mathrm{kin}} = -\frac{\mathbf{E}' \cdot \mathbf{p}'}{(1+p'^2)^{1/2}}, . \tag{5.22}$$

Thus, the energy gain can be obtained if one knows the wave electric field and the momentum of the particle.

Whistler wave field

In order to describe the electric and magnetic fields accompanied with the whistler wave, the ambient magnetic field is assumed to be along the $\hat{x}$-axis, i.e., $\mathbf{B}_0 = B_0(1,0,0)$. Since whistler waves propagating along the magnetic field are considered, they are not accompanied with an electric field along the magnetic field, i.e., $\mathbf{E}_{\rm wh} = (0, E_y, E_z)$. Additionally, all varying quantities are assumed to depend only on the spatial and temporal coordinate x and t, respectively. Then, the Ansatz

$$B'_y = B'_{\rm wh} \sin\left[k'x' - \omega' t'\right] \tag{5.23}$$
$$B'_z = B'_{\rm wh} \cos\left[k'x' - \omega' t'\right] \tag{5.24}$$

describes a right-hand circularly polarized whistler wave in normalized quantities. The corresponding electric fields are deduced from the induction equation, see Eq. (2.5),

$$\frac{1}{c}\frac{\partial B_x}{\partial t} = 0 \tag{5.25}$$
$$\frac{1}{c}\frac{\partial B_y}{\partial t} = \frac{\partial E_z}{\partial x} \tag{5.26}$$
$$\frac{1}{c}\frac{\partial B_z}{\partial t} = -\frac{\partial E_y}{\partial x} \tag{5.27}$$

It can be written in normalized quantities by

$$\frac{1}{S}\frac{\partial B'_y}{\partial t'} = \frac{\partial E'_z}{\partial x'} \tag{5.28}$$
$$\frac{1}{S}\frac{\partial B'_z}{\partial t'} = -\frac{\partial E'_y}{\partial x'} \tag{5.29}$$

Substituting the Ansatz (5.23) and (5.24) into Eqs. (5.28) and (5.29) and, subsequently, performing the integration, one can obtain an expression for the electric field of the whistler in terms of its magnetic field,

$$E'_y = \frac{V'_{\rm ph}}{S} B'_{\rm wh} \cos\left[k'x' - \omega' t'\right] \tag{5.30}$$
$$E'_z = -\frac{V'_{\rm ph}}{S} B'_{\rm wh} \sin\left[k'x' - \omega' t'\right] \tag{5.31}$$

with $V'_{\rm ph} = \omega'/k'$ as the normalized whistler phase velocity and $B'_{\rm wh}$ as the normalized amplitude of the whistler magnetic field. The integration constants are fixed requiring that the whistler electric field vanishes if the whistler magnetic field is absent. The normalized components for the whistler electric field can be substituted into Eq. (5.22).

Electron motion in a homogeneous magnetic field

The motion of an electron in an homogeneous magnetic field along the $\hat{x}$-axis can be expressed in the normalized way, see Eq. (5.19) and (5.20), by:

$$\frac{d\,p'_x}{dt'} = 0 \tag{5.32}$$

$$\frac{d\,p'_y}{dt'} = -\frac{p'_z}{(1+p'^2)^{1/2}} \tag{5.33}$$

$$\frac{d\,p'_z}{dt'} = \frac{p'_y}{(1+p'^2)^{1/2}} \tag{5.34}$$

and

$$\frac{d\,x'}{dt'} = \frac{S}{(1+p'^2)^{1/2}}\; p_\parallel \tag{5.35}$$

$$\frac{d\,y'}{dt'} = -S\,p_\perp \sin\left(\omega'_{\rm ce}t' + \phi_0\right) \tag{5.36}$$

$$\frac{d\,z'}{dt'} = S\,p_\perp \cos\left(\omega'_{\rm ce}t' + \phi_0\right) \tag{5.37}$$

Here, $\omega'_{\rm ce}$ denotes the relativistically shifted electron gyrofrequency normalized to $\omega_{\rm ce}$, i.e., $\omega'_{\rm ce} = \gamma^{-1}$ with $\gamma = (1-\beta^2)^{-1/2} = (1+p'^2)^{1/2}$. The solutions of the above equations of motion are:

$$p'_x = p_\parallel = \text{const} \tag{5.38}$$

$$p'_y = -p_\perp \sin\left(\omega'_{\rm ce}t' + \phi_0\right) \tag{5.39}$$

$$p'_z = p_\perp \cos\left(\omega'_{\rm ce}t' + \phi_0\right) \tag{5.40}$$

and

$$x'(t') = \frac{S}{(1+p'^2)^{1/2}}\; p_\parallel\, t' + x_0 \tag{5.41}$$

$$y'(t') = S\,p_\perp \cos\left(\omega'_{\rm ce}t' + \phi_0\right) + y_0 \tag{5.42}$$

$$z'(t') = S\,p_\perp \sin\left(\omega'_{\rm ce}t' + \phi_0\right) + z_0 \tag{5.43}$$

The normalized components for the momentum can be substituted into Eq. (5.22) for the energy gain.

Energy gain

Finally, substituting the expressions for the whistler electric field, Eq. (5.30) and Eq. (5.31), and the momentum of an electron in a homogeneous magnetic field, Eq. (5.39) and Eq. (5.40), in the expression for the energy gain, Eq. (5.22), one obtains the following result:

$$\dot{W}'_{\rm kin} = \frac{V'_{\rm ph}\beta_\perp B'_{\rm wh}}{S}\sin(\alpha_1+\alpha_2) \tag{5.44}$$

with $\alpha_1 = k'x'(t') - \omega' t'$ and $\alpha_2 = \omega'_{\rm ce} t' + \phi_0$, where the normalized frequency of the whistler magnetic field is ω'. Introducing the solution for $x'(t')$, see Eq. (5.41), the argument of the sin-function, $\alpha_1 + \alpha_2$, can be expressed by

$$\alpha_1 + \alpha_2 = Dt + \varphi_0,$$

with

$$D = k' S \beta^{\rm e}_{\parallel} - \omega' + (1 + p'^2)^{-1/2}, \tag{5.45}$$

$$\varphi_0 = k' x_0 + \phi_0.$$

Here x_0 and ϕ_0 are the initial conditions for the spatial coordinate and the phase, respectively. The temporal integration of Eq. (5.44) leads to

$$\Delta W'_{\rm kin} = -\frac{V'_{\rm ph} \beta_\perp B'_{\rm wh}}{D\, S} \left[\cos(Dt' + \varphi_0) - \cos\varphi_0\right], \tag{5.46}$$

which actually represents a temporally oscillating function. $\Delta W'_{\rm kin}$ only increases in time if the condition $D \to 0$ (which is exactly the resonance condition (5.14)) is fulfilled, resulting in

$$\Delta W'_{\rm kin} = \frac{V'_{\rm ph} \beta_\perp B'_{\rm wh}}{S}\, t' \sin\varphi_0. \tag{5.47}$$

From Eq. (5.47) follows that the particles either gain or loose energy due to the resonant interaction, if the phase φ_0 is in the range $0 < \varphi_0 < \pi$ and $\pi < \varphi_0 < 2\pi$, respectively. Assuming that the in-flowing electrons are gyrotropically distributed in an even way (i.e., equally distributed with respect to the gyro-phase), one half of them is accelerated, whereas the other half is decelerated with respect to the velocity perpendicular to the ambient magnetic field. Averaging over all angles φ_0 in the range $0 < \varphi_0 < \pi$, i.e.,

$$\frac{1}{\pi} \int_0^\pi \sin\varphi_0 \, {\rm d}\varphi_0 = \frac{2}{\pi} \tag{5.48}$$

one gets for the mean temporal energy gain of the accelerated electrons to be

$$\Delta \bar{W}'_{\rm kin} = 2\, \frac{V'_{\rm ph} \beta_\perp B'_{\rm wh}}{\pi S}\, t'. \tag{5.49}$$

As already mentioned, the gain and the loss of energy happens due to the change of the particle velocity perpendicular to the magnetic field due to the resonant electron–whistler interaction. Since a Maxwellian distribution, which is a monotonically decreasing function with respect to $V_\perp$, is assumed in the initial state, there are more particles that are accelerated, than those which are decelerated, which finally leads to a net energy gain of the whole population.

5.2.4 Magnetic mirroring at the shock

It is well known that a fast magnetosonic shock wave is accompanied by a jump of the density and the magnetic field. In this sense it represents a moving magnetic mirror at which charged particles can be reflected and subsequently accelerated. In a weakly varying magnetic field, i.e., $|r_{\rm L}\,\nabla B/B| \ll 1$, where $r_{\rm L}$ is the particle's Larmor radius, the particle motion is governed by the conservation of the kinetic energy (or amount of momentum) and the magnetic moment, [9], i.e.

$$p^2_{\parallel,j} \;+\; p^2_{\perp,j} = p^2_{\parallel,0} + p^2_{\perp,0} \qquad \left(\beta^2_{\parallel,j} + \beta^2_{\perp,j} = \beta^2_{\parallel,0} + \beta^2_{\perp,0}\right) \tag{5.50}$$

$$\frac{p^2_{\perp,j}}{B_j} \;=\; \frac{p^2_{\perp,0}}{B_0} \qquad \left(\frac{\beta^2_{\perp,j}}{B_j} = \frac{\beta^2_{\perp,0}}{B_0}\right) \tag{5.51}$$

where the index '0' denoted the values of the corresponding quantities in the undisturbed (i.e., upstream) region and the index 'j' denotes any subsequent temporal state. One can combine the above equations into the following expression

$$\frac{p^2_{\parallel,j}}{p^2_{\parallel,0}} = 1 - \left(\frac{B_j}{B_0} - 1\right)\frac{p^2_{\perp,0}}{p^2_{||,0}} \qquad \left(\frac{\beta^2_{\parallel,j}}{\beta^2_{\parallel,0}} = 1 - \left(\frac{B_j}{B_0} - 1\right)\frac{\beta^2_{\perp,0}}{\beta^2_{||,0}}\right). \tag{5.52}$$

Now, two important angles, as commonly used, are introduced here: the pitch angle,

$$\alpha_j = \arctan\frac{p_{\perp,j}}{p_{\parallel,j}} = \arctan\frac{\beta_{\perp,j}}{\beta_{\parallel,j}} \tag{5.53}$$

and the loss-cone angle,

$$\alpha_{{\rm lc},j} = \arcsin(B_0/B_j)^{1/2}, \tag{5.54}$$

and hence Eq. (5.52) can be re-written as

$$\frac{p^2_{\parallel,j}}{p^2_{\parallel,0}} = 1 - \frac{\tan^2\alpha_0}{\tan^2\alpha_{{\rm lc},j}}, \tag{5.55}$$

where $\alpha_0 = \arctan\left(p_{\perp,0}/p_{\parallel,0}\right) = \arctan\left(\beta_{\perp,0}/\beta_{\parallel,0}\right)$ is the initial pitch angle of the particles and depends on the initial conditions. The inspection of Eq. (5.55) provides that all particles with an initial pitch angle $\alpha_0 > \alpha_{{\rm lc},j}$ are reflected. Identifying B_0 and B_j with the magnetic fields $B_{\rm up}$ and $B_{\rm down}$ in the up- and downstream region, respectively, all particles with an initial pitch angle

$$\alpha_0 > \alpha_{\rm lc,sh} = \arcsin\left(B_{\rm up}/B_{\rm down}\right)^{1/2} \tag{5.56}$$

will be reflected by their encounter with the shock. The other ones are transmitted into the downstream region.

Since the shock is moving, the above presented consideration must actually be done in the so-called de Hoffmann-Teller frame, see e.g., [59]. The shock speed in the de Hoffmann-Teller frame is given by $V_{\rm sh}^{\rm HT} = V_{\rm sh}\sec\theta_{\rm B,n}$ [59], which has a typical value of $3000\,{\rm km\,s^{-1}}$

adopting $V_{\rm sh} = 1000\,{\rm km\,s^{-1}}$ and $\theta_{\rm B,n} = 70°$. Since this value is smaller than the thermal electron velocity $V_{\rm th,e} = (k_{\rm B}T/m_{\rm e})^{1/2}$, which has a typical value of $4600\,{\rm km\,s^{-1}}$ for a coronal temperature of 1.4 MK, the influence of the shock motion on the electron reflection process can be neglected for considering electrons, as done in this Subsection. Due to the motion of the shock, the electrons reflected at it get an additional energy gain due to shock drift acceleration, but this can be neglected in the case of quasi-perpendicular (but not for nearly perpendicular) shocks under coronal conditions.
As already discussed, the electrons increase their momentum perpendicular to the ambient magnetic field due to the resonant electron−whistler interaction (see Fig. 5.3) and, consequently, their pitch angle (see Eq. 5.53), as well. Thus, a major part of the energized electrons fulfill the reflection condition (5.56) if they encounter the shock and, finally, move away from the shock into the upstream region. After the reflection the accelerated electrons are co-streaming with the whistler and, thus, do not fulfill the resonance condition (5.14), i.e., they are out of resonance and can freely reach the far upstream region, where they can be observed in terms of herringbones in the solar type II radio emission.

5.3 Discussion

In the framework of the proposed mechanism, the electron acceleration happens in the $(\beta_\perp^{\rm e}$–$\beta_\parallel^{\rm e})$-plane due to the resonant electron−whistler interaction as illustrated in Fig. 5.3. As already mentioned, it actually represents a motion toward higher values of $\beta_\perp^{\rm e}$ within the so-called 'resonance band' $(\beta_\perp^{\rm e}$–$\beta_\parallel^{\rm e})$-plane. Fig. 5.3 results from parameters, which are appropriate for shock wave associated with solar type II radio bursts around 55 MHz. In the initial state, the electron must be located in the 'resonance band' in order to become energized. The process of acceleration can be demonstrated with the following example. In the 'resonance band', the electrons with the lowest initial energy have values of $\beta_\parallel^{\rm e} = -0.076$ and $\beta_\perp^{\rm e} = 0$, i.e., they have an initial energy of $W_0 = 1.5\,{\rm keV}$. In the case of the most efficient energy gain, i.e., the electron experiences only acceleration, they move upward along a straight line parallel to the $\beta_\perp^{\rm e}$-axis in the $(\beta_\perp^{\rm e}$–$\beta_\parallel^{\rm e})$-plane (see Fig. 5.3). They leave the 'resonance band' at the point $(\beta_\parallel^{\rm e} = -0.076,\ \beta_\perp^{\rm e} = 0.537)$ in the $(\beta_\perp^{\rm e}$–$\beta_\parallel^{\rm e})$-plane. Then, they have a final kinetic energy of about 100 keV. During this process, the pitch angle changes from 0° to 82°. This example represents the most efficient process of electron energizing (i.e., from 1.5 to 100 keV) in the framework of the proposed mechanism. Particles with such a final pitch angle are reflected at shock, since their pitch angle is greater than the loss-cone angle $\alpha_{\rm lc,sh} = 45°$ as required for reflection, see Eq. (5.56). Such a value is obtained for the loss-cone angle, if one assumes a jump of the magnetic field $B_{\rm down}/B_{\rm up} = 2$ as a typical value for coronal shock waves.

After the reflection at the shock, the energized electrons are moving in an area of enhanced whistler waves. The whistler amplitude is about 0.2 of the upstream magnetic field [29, 38], so that the total magnetic field is enhanced by factor of 1.02 with respect to the undisturbed upstream magnetic field (see Fig. 3.28 (left panel) in Chapter 3). Since the electrons are out of resonance with these whistlers, they can freely leave this area. But due to the connected decrease of the total magnetic field from $B_j = 1.02\,B_{\rm up}$ to $B_0 = 1.0\,B_{\rm up}$, the electron velocity parallel to the magnetic field, experiences an increase from $\beta_{\parallel,0}^{\rm e} = -0.076$

($22\,800\,\mathrm{km\,s^{-1}}$) to $\beta^{\mathrm{e}}_{\parallel,j} = 0.1078$ ($32\,340\,\mathrm{km\,s^{-1}}$) after the reflection, i.e., by a factor of 1.42, see Eq. (5.52).

In summary, due to the resonant electron–whistler interaction the particle velocity perpendicular to the magnetic field is strongly enhanced. Subsequently, these particles are reflected at the jump of the magnetic field associated with the shock because of their high magnetic momentum. If they leave the area of enhanced whistlers, that is connected with a slightly decrease of the total magnetic field, the electron velocity parallel to the upstream magnetic field will increase as well. Thus, a part of the gained kinetic energy perpendicular to the magnetic field due to the resonant electron–whistler interaction is finally transfered into an enhanced kinetic energy parallel to the magnetic field, i.e., into a particle acceleration.

The inspection of Fig. 5.3 reveals, that only electrons with an initial energy $\geq 1.5\,\mathrm{keV}$ corresponding to a velocity of $0.076c = 4.96\,V_{\mathrm{th,e}}$ (with $V_{\mathrm{th,e}} = 4600\,\mathrm{km\,s^{-1}}$ as the thermal electron speed for a coronal temperature of 1.4 MK) will be accelerated. In the case of an initial Maxwellian distribution of the electrons in the upstream region, only $1.8 \times 10^{-6} N_{\mathrm{e}}$ of all electrons fulfill this conditions and can really be accelerated by the proposed mechanism, i.e., only a minor part of the electrons in the upstream region gain energy.

In order to give some estimation with respect to the acceleration time, we introduce the whistler period, $T_{\mathrm{wh}} = 2\pi/(\omega'\omega_{\mathrm{ce}})$. Then, the time in dimensionless form can be presented as $t' = \tau T_{\mathrm{wh}}\omega_{\mathrm{ce}}$, where τ is the number of periods of the whistler oscillation. Finally, we obtain the expression for the energy gain (5.49) in terms of whistler periods, i.e.,

$$\Delta\bar{W}'_{\mathrm{kin}} = \frac{\beta^{\mathrm{e}}_{\perp} B'_{\mathrm{wh}}}{Sk'} 4\tau. \tag{5.57}$$

This is however only a rough estimate for the time (given in whistler periods) needed for an electron to reach such an energy gain, $\Delta\bar{W}'_{\mathrm{kin}}$. From observations it is known that the whistler amplitude is about $B'_{\mathrm{wh}} = 0.2$ of the upstream magnetic field [38, 29]. Also, requesting certain final energy of the electron, $W_{\mathrm{kin}}/(m_0c^2)$, one can get the final value of $\beta^{\mathrm{e}}_{\perp}$, for example from the curve plotted on Fig. 5.4 (thus $k' = 0.518$, corresponding to $\omega' = 0.211$, will be used further on). The procedure is as follows: In the special case of herringbones, with a typical energy of $W^{\mathrm{HB}}_{\mathrm{kin}} = 7.3\,\mathrm{keV}$ (or $W'^{7.3\,\mathrm{keV}}_{\mathrm{kin}} = 0.0143$), from Eq. (5.16) one finds that in this case $\beta = 0.167$ and the corresponding value of $\beta^{\mathrm{e}}_{\perp} = 0.149$, if $\beta^{\mathrm{e}}_{\parallel} = -0.076$ is always assumed. Then, after substituting the mean energy gain (taking out the initial energy W_0 first), the obtained mean electron velocity $\bar{\beta^{\mathrm{e}}_{\perp}} \approx \beta^{\mathrm{e}}_{\perp}/2$, and the parameters $B'_{\mathrm{wh}} = 0.2$, $S = 20$ and $k' = 0.518$ into Eq. (5.57), finally one gets the estimate for τ. A summary of the obtained in this manner estimates for $\bar{\beta^{\mathrm{e}}_{\perp}}$ and τ in the case of herringbones (7.3 keV), and also for electrons with a final energy of 25 keV and 80 keV (or equivalently, with electron beam velocity of $0.3\,c$ and $0.5\,c$, respectively), is presented below:

$$\begin{aligned}
\Delta\bar{W}'_{\mathrm{kin}} &= W'^{7.3\,\mathrm{keV}}_{\mathrm{kin}} - W'_0 = 0.0113, \quad \beta = 0.167, \quad \bar{\beta^{\mathrm{e}}_{\perp}} = 0.0745, \quad \tau = 2; \\
\Delta\bar{W}'_{\mathrm{kin}} &= W'^{25\,\mathrm{keV}}_{\mathrm{kin}} - W'_0 = 0.0459, \quad \beta = 0.302, \quad \bar{\beta^{\mathrm{e}}_{\perp}} = 0.146, \quad \tau = 4.1; \\
\Delta\bar{W}'_{\mathrm{kin}} &= W'^{80\,\mathrm{keV}}_{\mathrm{kin}} - W'_0 = 0.1533, \quad \beta = 0.502, \quad \bar{\beta^{\mathrm{e}}_{\perp}} = 0.251, \quad \tau = 7.9.
\end{aligned}$$

Thus, the electrons associated with the herringbones can be generated by this mechanism within nearly two whistler periods, whereas the more energetic electrons need four to eight whistler periods. In general, the electrons are accelerated up to high energies within just several whistler periods. This result is consistent with the observation of attached whistler waves at shocks, where only several whistler periods are present [29, 38].

In the presented discussion, typical parameters of coronal shock waves are used, as deduced from solar radio observations. These are: the shock speed, $V_{\mathrm{shock}} = 1000\,\mathrm{km\,s^{-1}}$; the angle between the shock normal and the upstream magnetic field, $\theta_{\mathrm{B,n}} = 70°$; the coronal temperature of $1.4 \times 10^6\,\mathrm{K}$ and the ratio of the electron plasma frequency to the electron cyclotron frequency, $S = 20$. Naturally, the efficiency of the proposed process depends on the shock speed V_{sh}, the angle $\theta_{\mathrm{B,n}}$ and the ratio S. But the discussions here shows that the presented mechanism is in agreement with the observations of solar type II bursts in the solar radio radiation and by in-situ spacecraft measurements.

The proposed mechanism of electron acceleration in this Chapter is applicable for quasi-perpendicular shocks, i.e., the angle $\boldsymbol{\theta_{\mathrm{B,n}}}$ is in the range of $\mathbf{50°-80°}$. Thus, the problem connected with the pure shock-drift acceleration, i.e., the requirement for a nearly perpendicular shock geometry ($\boldsymbol{\theta_{\mathrm{B,n}} \approx 90°}$), is removed by the proposed new mechanism. It explains the production of highly energetic electrons at coronal shocks, as really observed (see Fig. 5.1). A continuous regime for electron acceleration is achieved, when the electron moves in the resonance band, i.e., the electrons are actually accelerated in a localized wave structure. The proposed mechanism, see [69, 70], can also act at other shocks in space plasmas, e.g., at supernova remnants.

Chapter 6

Summary

The aim of the dissertation was to propose new theoretical models on electron acceleration during flares in the solar corona, namely within the so-called localized wave structures, that arise for example due to solar jets and/or shock waves both moving through the solar corona. The question of how electrons are accelerated during flares in the solar corona is still not fully answered. The observed phenomena from the available high resolution data (provided by the fleet of satellite missions in space and the ground-based optical and radio observatories), demands for theoretical explanation. Beside naming the problem to be solved, the observations additionally provide the input parameters and the restrictions that need to be kept by the theoretical and numerical attempts.

The work in this thesis is a step in this direction, namely to provide new scenarios in order to explain the mechanisms leading to the successful acceleration of electrons in spatially localized wave structures in the solar corona. The two possible configurations that show evidence for the production of non-thermal electrons in the solar corona are the magnetic reconnection and the shock waves.

The solar corona is filled by a fully ionized (mainly electron–proton) plasma, which intrinsically contains a lot of different wave modes. Few of them are able to accelerate electrons by the electron–wave interaction. As already mentioned two such mechanisms are investigated in this thesis. Before summarizing both, the non-linear treatment of low-frequency plasma waves is done in terms of the so-called **Sakai–Sonnerup system**, which is considered with respect to the search of stationary solutions. This system of equations describe the evolution of one-dimensional plasma waves for low frequencies, i.e., much lower than the electron cyclotron frequency. As reminded of the fully non-linear treatment of the well-known **mathematical pendulum**, for illustration, the solutions of the Sakai–Sonnerup system also offer both oscillatory (or periodic) and solitary types of solutions, where the latter ones are related to very special choice of parameters and initial conditions. Nevertheless, the oscillatory (or periodic) solutions are mostly probably to occur in space plasmas and are related to different kinds of polarization, e.g., circular, elliptical and arc- or banana-like polarization, as really observed in terms of low frequency magnetic field fluctuations in space plasmas. This aspect, i.e., looking for non-linear solutions in the case of whistler waves, can be regarded as a preliminary stage for the study of electron acceleration at attached whistlers at shock waves in the solar corona.

Model for electron acceleration due to solar jets

With respect to the flares, here the conventional model for magnetic reconnection was adopted and a special attention is drawn toward one of the possible outcomes from the rearranging of the magnetic filed configuration after a flare: the solar jets. When the plasma is ejected from the reconnection site, it continues to propagate further through the corona. Such plasma jets are really seen in the soft X-ray emission with the *Yohkoh* satellite, and additionally they are spatially and temporally associated with type III metric radio bursts in the radio emission. This specific radio feature represents the signature of an electron beam propagating along the magnetic field lines through the corona. While the jet moves through the surrounding coronal plasma, it creates disturbances that lead to instability. The region of this instability was found to be localized, namely, the area, where the excited fluctuations (in electrostatic sense) are sustained, exists only for a small range of the jet initial velocity. Hence, when the jet speed has a value within the instability range, the excited wave-like disturbances grow in time. A test electron was investigated within the electrostatic field of such a wave: it displays a co-motion with it (in the space–time diagram) and also an energy gain within short time scales (in the energy–time diagram). The proposed here mechanism for electron acceleration gives an explanation for the observed classification of the jet–associated type III radio bursts, namely:

(i) Jets that are not accompanied by type III radio bursts, can be explained as plasma streams with initial speed smaller than the values comprising the instability range (for the current plasma configuration), so such jets cannot give rise to an electrostatic instability and, hence, to energize electrons that lead to the type III bursts in the radio spectrum;

(ii) Jets with a simultaneous appearance of type III bursts: in this case the jet is ejected with a speed within the instability range and the electrons are accelerated nearly simultaneously, i.e., type III radio burst is seen together with the observed in soft X-rays plasma motion;

(iii) Jets accompanied with type III radio bursts, but with a temporal delay concerning the jet onset time, are due to a faster onset velocity of the jet than the required from the instability range and thus initially the jet is not able to excite electrostatic fluctuations. With the time, however, the jet is decelerating due to Coulomb collisions, for example, and its speed slows down to a velocity leading to the onset of the electrostatic instability and, consequently, to the occurrence of type III radio bursts.

Model for electron acceleration due to attached whistlers at coronal shocks

The search for a new scenario for electron acceleration at coronal shock waves aims to propose a model that avoids the restriction for a nearly perpendicular shock configuration, as required by the existing theories (for example the mechanism for shock–drift acceleration). The observations of shocks in space, especially at co-rotating interaction regions, show, that electrons are efficiently accelerated at shocks attached by whistler waves. Motivated by this data, a new model for electron acceleration in the case of a quasi-perpendicular shocks (i.e., for an angle between the upstream magnetic field and the shock normal of $\theta_{\mathrm{B,n}} = 50°–80°$) is proposed, where the presence of whistler wave packets attached at the upstream part

of the shock wave are taken into account. Here, it is basically assumed that the physical processes at collisionless shocks are the same for all collisionless plasmas. The following scheme is proposed:

(a) The first stage of the model is the velocity gain of the incoming toward the shock front protons. They can increase substantially their velocity due to the reflection at the shock and after that they return in the upstream region.

(b) These so-accelerated protons are able to excite whistler waves due to a wave–particle resonance interaction in the upstream region. The whistler waves that fulfill the so-called resonance condition are considered to be excited by those protons.

(c) Now, the resonant interaction of these whistlers with the (in-coming) electrons is considered with the result, that only counter-streaming (i.e., toward the shock front) electrons are in resonance with these whistler wave packets (forming a so-called here resonance band), leading to a substantial electron velocity (and energy) gain.

(d) Due to the resonant electron–whistler interaction, the electron gains velocity and energy from the whistler electromagnetic field (while moving within the resonance band). When the electron leave this resonance band, the mechanism of energy gain ceases. Finally, the electrons reach the shock front and those of them who have increased their pitch angle to values greater that those of the loss-cone angle (given by the jump of the magnetic field across the shock) will be reflected back into the upstream region. The rest of the electron population are transmitted into the downstream region. Due to the motion of the shock itself, an additional energy gain can be obtained due to the reflection, but this is minor in comparison to that of the resonant electron–whistler interaction.

(e) The so-energized electron propagate further in the upstream region. Because they are co-streaming with the whistler packets now, they are out of resonance and can propagate undisturbed in the far upstream region and be detected as type II bursts in the solar radio emission.

The proposed mechanism of electron acceleration due to electron–whistler–shock interaction explains the production of highly energetic electrons at the shocks, within the more realistic quasi-perpendicular shock configuration, in contrast to the nearly perpendicular shock geometry necessary in previously existing models.

In both presented mechanisms, the kinetic energy of protons is transfered into electrons by the action of the localized wave structures, i.e., at jets outflowing from the magnetic reconnection site and at shock waves in the corona. Both models are motivated by observations and the obtained results agree well with radio and X-ray observations. The process of electron acceleration is also of general astrophysical interest and the proposed here models can be further applied to other plasma configurations in space, i.e., for shocks in the outflow reconnection region of the solar corona and in the interplanetary medium, as well as even beyond the domain of the solar system, e.g., at flares at other stars, relativistic jets, and supernova remnants.

Bibliography

[1] K. Akimoto, D. Winske, T. G. Onsager, M. F. Thomsen, and S. P. Gary. Steepening of parallel propagating hydromagnetic waves into magnetic pulsations – A simulation study. *J. Geophys. Res.*, 96:17599–17607, October 1991.

[2] H. Aurass. Coronal Mass Ejections and Type II Radio Bursts. In G. Trottet, editor, *LNP Vol. 483: Coronal Physics from Radio and Space Observations*, pages 135–160, 1997.

[3] H. Aurass and K.-L. Klein. Observations of electon beam propagation in closed magnetic structures in the solar corona. *Adv. Space Res.*, 17:269–272, 1996.

[4] H. Aurass and K.-L. Klein. Spectrographic and imaging observations of solar type U radio bursts. *A&AS*, 123:279–304, June 1997.

[5] H. Aurass, K.-L. Klein, and P. C. H. Martens. First detection of correlated electron beams and plasma jets in radio and soft x-ray data. *Sol. Phys.*, 155:203–206, November 1994.

[6] H. Aurass, B. Vršnak, and G. Mann. Shock-excited radio burst from reconnection outflow jet? *A&A*, 384:273–281, March 2002.

[7] J. N. Bahcall and R. K. Ulrich. Solar models, neutrino experiments, and helioseismology. *Reviews of Modern Physics*, 60:297–372, April 1988.

[8] K. Baumgärtel. Soliton approach to magnetic holes. *J. Geophys. Res.*, 104:28295–28308, December 1999.

[9] W. Baumjohann and R. A. Treumann. *Basic space plasma physics*. London: Imperial College Press, 1996.

[10] A. O. Benz. *Plasma astrophysics: Kinetic processes in solar and stellar coronae*. Astrophysics and Space Science Library, vol. 184, Dordrecht: Kluwer, 1993.

[11] A. Bhatnagar and W. Livingston. *Fundamentals of solar astronomy*. World Scientific Series in Astronomy and Astrophysics, Vol. 6, New Jersey, London, Singapore: World Scientific, ISBN 981-238-244-5, April 2005.

[12] J. C. Brown. The Deduction of Energy Spectra of Non-Thermal Electrons in Flares from the Observed Dynamic Spectra of Hard X-Ray Bursts. *Sol. Phys.*, 18:489–502, 1971.

[13] J. C. Brown. The Directivity and Polarisation of Thick Target X-Ray Bremsstrahlung from Solar Flares. *Sol. Phys.*, 26:441–459, 1972.

[14] I. H. Cairns and R. D. Robinson. Herringbone bursts associated with type II solar radio emission. *Sol. Phys.*, 111:365–383, 1987.

[15] J. Christensen-Dalsgaard, W. Dappen, S. V. Ajukov, E. R. Anderson, H. M. Antia, S. Basu, V. A. Baturin, G. Berthomieu, and 25 co-authors. The Current State of Solar Modeling. *Science*, 272:1286–1292, May 1996.

[16] H.-T. Classen and H. Aurass. On the association between type II radio bursts and CMEs. *A&A*, 384:1098–1106, March 2002.

[17] H.-T. Classen, G. Mann, R. J. Forsyth, and E. Keppler. Low frequency plasma turbulence and high energy particles at CIR-related shock waves. *A&A*, 347:313–320, July 1999.

[18] H.-T. Classen, G. Mann, and E. Keppler. Particle acceleration efficiency and MHD characteristics of CIR-related shocks. *A&A*, 335:1101–1110, July 1998.

[19] V. Domingo. SOHO, Yohkoh, Ulysses and Trace: The four solar missions in perspective, and available resources. *Ap&SS*, 282:171–188, 2002.

[20] P. G. Drazin and R. S. Johnson. *Solitons: an Introduction.* Cambridge University Press, Cambridge, ISBN 0-521-33655-4 (paperback), 1989.

[21] G. A. Dulk and D. J. McLean. Coronal magnetic fields. *Sol. Phys.*, 57:279–295, April 1978.

[22] C. Estel and G. Mann. Mean free path and energy loss of electrons in the solar corona and the inner heliosphere. *A&A*, 345:276–281, May 1999.

[23] D. H. Fairfield and K. W. Behannon. Bow shock and magnetosheath waves at Mercury. *J. Geophys. Res.*, 81:3897–3906, August 1976.

[24] A. H. Gabriel. A magnetic model of the solar transition region. *Royal Society of London Philosophical Transactions Series A*, 281:339–352, May 1976.

[25] M. L. Goldstein, C. W. Smith, and W. H. Matthaeus. Large amplitude MHD waves upstream of the Jovian bow shock. *J. Geophys. Res.*, 88:9989–9999, December 1983.

[26] N. Gopalswamy. *Coronal mass ejections and type II radio bursts*, pages 207–220. Solar Eruptions and Energetic Particles, 2006.

[27] N. Gopalswamy and M. R. Kundu. Estimation of the mass of a coronal mass ejection from radio observations. *ApJ*, 390:L37–L39, May 1992.

[28] J. T. Gosling and V. J. Pizzo. Formation and Evolution of Corotating Interaction Regions and their Three Dimensional Structure. *Space Sci. Rev.*, 89:21–52, July 1999.

[29] D. A. Gurnett, R. R. Anderson, B. Haeusler, G. Haerendel, and O. H. Bauer. Plasma waves associated with the AMPTE artificial comet. *Geophys. Res. Lett.*, 12:851–854, December 1985.

[30] J. Heyvaerts. *Particle acceleration in solar flares*, pages 429–555. Gordon and Breach, Science Publishers, Inc., NewYork, London, Paris, 1981.

[31] G. D. Holman. Acceleration of runaway electrons and Joule heating in solar flares. *ApJ*, 293:584–594, June 1985.

[32] G. D. Holman and M. E. Pesses. Solar type II radio emission and the shock drift acceleration of electrons. *ApJ*, 267:837–843, April 1983.

[33] M. Hoppe and C. T. Russell. On the nature of ULF waves upstream of planetary bow shocks. *Adv. Space Res.*, 1:327–332, 1981.

[34] M. M. Hoppe and C. T. Russell. Plasma rest frame frequencies and polarizations of the low-frequency upstream waves – ISEE 1 and 2 observations. *J. Geophys. Res.*, 88:2021–2027, March 1983.

[35] M. M. Hoppe, C. T. Russell, L. A. Frank, T. E. Eastman, and E. W. Greenstadt. Upstream hydromagnetic waves and their association with backstreaming ion populations – ISEE 1 and 2 observations. *J. Geophys. Res.*, 86:4471–4492, June 1981.

[36] J. D. Huba. Hall magnetohydrodynamics in space and laboratory plasmas. *Phys. Plasmas*, 2:2504–2513, June 1995.

[37] T. Kakutani, T. Kawahara, and T. Taniuti. Nonlinear hydromagnetic solitary waves in a collision-free plasma with isothermal electron pressure. *J. Phys. Soc. Japan*, 23:1138–1149, 1967.

[38] C. F. Kennel, J. P. Edmiston, and T. Hada. A quarter century of collisionless shock research. *Washington DC American Geophysical Union Geophysical Monograph Series*, 34:1–36, 1985.

[39] K. O. Kiepenheuer. *Solar Activity*, pages 322–465. The Sun, ed. G. P. Kuiper, University Chicago Press, Chicago, Illinois, 1953.

[40] A. Klassen, M. Karlický, and G. Mann. Superluminal apparent velocities of relativistic electron beams in the solar corona. *A&A*, 410:307–314, October 2003.

[41] S. Koutchmy. Coronal physics from eclipse observations. *A&AS*, 14:29–39, April 1994.

[42] N. A. Krall and A. W. Trivelpiece. *Principles of Plasma Physics*. San Francisco Press, 1986.

[43] M. R. Kundu, J. P. Raulin, N. Nitta, H. S. Hudson, M. Shimojo, K. Shibata, and A. Raoult. Detection of Nonthermal Radio Emission from Coronal X-Ray Jets. *ApJ*, 447:L135–L137, July 1995.

[44] M. R. Kundu, J.-P. Raulin, N. Nitta, K. Shibata, and M. Shimojo. Two-Sided-Loop Type X-ray Jets and Metric Radio Bursts. *Sol. Phys.*, 178:173–178, 1998.

[45] M. R. Kundu, K. T. Strong, M. Pick, K. T. Harvey, S. R. Kane, S. M. White, and H. S. Hudson. Metric Type III Bursts from Flaring X-ray Bright Points. In *Proc. Kofu Symp.*, pages 343–346, July 1994.

[46] A. Lara, N. Gopalswamy, S. Nunes, G. Muñoz, and S. Yashiro. A statistical study of CMEs associated with metric type II bursts. *Geophys. Res. Lett.*, 30:4–1, May 2003.

[47] R. B. Leighton, R. W. Noyes, and G. W. Simon. Velocity Fields in the Solar Atmosphere. I. Preliminary Report. *ApJ*, 135:474–499, March 1962.

[48] R. P. Lin. Non-relativistic solar electrons. *Space Sci. Rev.*, 16:189–256, 1974.

[49] R. P. Lin, B. R. Dennis, G. J. Hurford, and 63 co-autors. The Reuven Ramaty High-Energy Solar Spectroscopic Imager (RHESSI). *Sol. Phys.*, 210:3–32, November 2002.

[50] A. Magalhães and J. Carneiro. The University of Porto Radio Spectrograph. *Ap&SS*, 261:211–212, 1998.

[51] G. Mann. Theory and Observations of Coronal Shock Waves. In A. O. Benz and A. Krüger, editors, *LNP Vol. 444: Coronal Magnetic Energy Releases*, pages 183–200, 1995.

[52] G. Mann. *EIT waves and coronal shock waves*, pages 221–231. Solar Eruptions and Energetic Particles, 2006.

[53] G. Mann, H. Aurass, W. Voigt, and J. Paschke. Preliminary observations of solar type II bursts with the new radiospectrograph in Tremsdorf (Germany). In C. Mattok, editor, *ESA SP-348: Coronal Streamers, Coronal Loops, and Coronal and Solar Wind Composition*, pages 129–132, November 1992.

[54] G. Mann, H.-T. Classen, E. Keppler, and E. C. Roelof. On electron acceleration at CIR related shock waves. *A&A*, 391:749–756, August 2002.

[55] G. Mann, T. Classen, and H. Aurass. Characteristics of coronal shock waves and solar type II radio bursts. *A&A*, 295:775–781, March 1995.

[56] G. Mann, P. Hackenberg, and E. Marsch. Linear mode analysis in multi-ion plasmas. *J. Plasma Phys.*, 58:205–221, August 1997.

[57] G. Mann, F. Jansen, R. J. MacDowall, M. L. Kaiser, and R. G. Stone. A heliospheric density model and type III radio bursts. *A&A*, 348:614–620, August 1999.

[58] G. Mann and A. Klassen. Shock accelerated electron beams in the solar corona. In J. Kuijpers, editor, *ESA SP-506: Solar Variability: From Core to Outer Frontiers*, pages 245–248, December 2002.

[59] G. Mann and A. Klassen. Electron beams generated by shock waves in the solar corona. *A&A*, 441:319–326, October 2005.

[60] G. Mann, A. Klassen, H. Aurass, and H.-T. Classen. Formation and development of shock waves in the solar corona and the near-Sun interplanetary space. *A&A*, 400:329–336, March 2003.

[61] G. Mann and H. Luehr. Comparison of low frequency magnetic field fluctuations upstream of earth's bow shock with a strong Alfvénic turbulence model. *Ann. Geophysicae*, 9:681–689, October 1991.

[62] G. Mann, H. Luehr, and W. Baumjohann. Statistical analysis of short large-amplitude magnetic field structures in the vicinity of the quasi-parallel bow shock. *J. Geophys. Res.*, 99:13315–13323, January 1994.

[63] P. S. McIntosh. The classification of sunspot groups. *Sol. Phys.*, 125:251–267, February 1990.

[64] D. E. McKenzie. Signatures of Reconnection in Eruptive Flares [Invited]. In P. C. H. Martens and D. Cauffman, editors, *Multi-Wavelength Observations of Coronal Structure and Dynamics*, pages 155–164, January 2002.

[65] J. F. McKenzie and T. B. Doyle. The properties of fast and slow oblique solitons in a magnetized plasma. *Phys. Plasmas*, 9:55–63, January 2002.

[66] D. B. Melrose. *Plasma emission mechanisms*, pages 177–210. Solar Radiophysics: Studies of Emission from the Sun at Metre Wavelengths, 1985.

[67] R. Miteva and G. Mann. Electron Acceleration due to Jets in the Solar Corona. In *ESA SP-600: The Dynamic Sun: Challenges for Theory and Observations*, December 2005.

[68] R. Miteva and G. Mann. Excitation of electrostatic waves in a flaring plasma. In W. S. Rucker, H. O. Kurth and G. Mann, editors, *Planetary Radio Emissions VI*, pages 409–417, 2006.

[69] R. Miteva and G. Mann. Electron Acceleration at Whistler Wave Packets Attached to Coronal Shock Waves. *Central European Astrophysical Bulletin*, 31:155, 2007.

[70] R. Miteva and G. Mann. On electron acceleration at shock waves in the solar corona (submitted). *A&A*, 2007.

[71] R. Miteva, G. Mann, C. Vocks, and H. Aurass. Excitation of electrostatic fluctuations by jets in a flaring plasma. *A&A*, 461:1127–1132, January 2007.

[72] R. Miteva, C. Vocks, G. Mann, and H. Aurass. Mechanism for electron acceleration due to propagation of jets in the solar corona. In V. Bothmer and A. A. Hady, editors, *IAU Symposium*, pages 169–172, 2006.

[73] E. Mjølhus. Velocity–amplitude relationships and polarizations in families of MHD solitary waves. *Physica Scripta Volume T*, 122:135–153, February 2006.

[74] G. J. Nelson and D. B. Melrose. *Type II bursts*, pages 333–359. Solar Radiophysics: Studies of Emission from the Sun at Metre Wavelengths, 1985.

[75] G. J. Newkirk. The Solar Corona in Active Regions and the Thermal Origin of the Slowly Varying Component of Solar Radio Radiation. *ApJ*, 133:983–1013, May 1961.

[76] L. J. November, J. Toomre, K. B. Gebbie, and G. W. Simon. The detection of mesogranulation on the sun. *ApJ*, 245:L123–L126, May 1981.

[77] E. N. Parker. Dynamics of the Interplanetary Gas and Magnetic Fields. *ApJ*, 128:664–675, November 1958.

[78] G. Paschmann, N. Sckopke, J. R. Asbridge, S. J. Bame, and J. T. Gosling. Energization of solar wind ions by reflection from the earth's bow shock. *J. Geophys. Res.*, 85:4689–4693, September 1980.

[79] G. Paschmann, N. Sckopke, S. J. Bame, J. R. Asbridge, J. T. Gosling, C. T. Russell, and E. W. Greenstadt. Association of low-frequency waves with suprathermal ions in the upstream solar wind. *Geophys. Res. Lett.*, 6:209–212, March 1979.

[80] G. Paschmann, N. Sckopke, I. Papamastorakis, J. R. Asbridge, S. J. Bame, and J. T. Gosling. Characteristics of reflected and diffuse ions upstream from the earth's bow shock. *J. Geophys. Res.*, 86:4355–4364, June 1981.

[81] M. Pick, A. Raoult, G. Trottet, N. Vilmer, K. Strong, and A. Magalhaes. Energetic Electrons and Magnetic Field Structures in the Corona. In *Proc. Kofu Symp.*, pages 263–266, July 1994.

[82] V. Pizzo. A three-dimensional model of corotating streams in the solar wind. I - Theoretical foundations. *J. Geophys. Res.*, 83:5563–5572, December 1978.

[83] E. R. Priest. *Solar magneto-hydrodynamics*. Dordrecht, Holland; Boston: D. Reidel Pub. Co.; Hingham, 1982.

[84] J. P. Raulin, M. R. Kundu, H. S. Hudson, N. Nitta, and A. Raoult. Metric Type III bursts associated with soft X-ray jets. *A&A*, 306:299–304, February 1996.

[85] J. P. Raulin, M. R. Kundu, N. Nitta, and A. Raoult. Radio Continuum and Type III Bursts Associated with Coronal X-Ray Structures. *ApJ*, 472:874–881, December 1996.

[86] M. J. Reiner, M. L. Kaiser, N. Gopalswamy, H. Aurass, G. Mann, A. Vourlidas, and M. Maksimovic. Statistical analysis of coronal shock dynamics implied by radio and white-light observations. *J. Geophys. Res.*, 106:25279–25290, November 2001.

[87] W. Riedler, K. Schwingenschuh, Y. G. Yeroshenko, V. A. Styashkin, and C. T. Russell. Magnetic field observations in Comet Halley's coma. *Nature*, 321:288–289, May 1986.

[88] J.-I. Sakai and U. O. Sonnerup. Modulational instability of finite amplitude dispersive Alfven waves. *J. Geophys. Res.*, 88:9069–9079, November 1983.

[89] M. Scholer. Upstream waves, shocklets, short large-amplitude magnetic structures and the cyclic behavior of oblique quasi-parallel collisionless shocks. *J. Geophys. Res.*, 98:47–57, January 1993.

[90] M. Scholer, G. Mann, S. Chalov, M. I. Desai, L. A. Fisk, J. R. Jokipii, R. Kallenbach, E. Keppler, J. Kóta, H. Kunow, M. A. Lee, T. R. Sanderson, and G. M. Simnett. Origin, Injection, and Acceleration of CIR Particles: Theory Report of Working Group 7. *Space Sci. Rev.*, 89:369–399, July 1999.

[91] M. Scholer, K. J. Trattner, and H. Kucharek. Ion injection and Fermi acceleration at earth's bow shock – The 1984 September 12 event revisited. *ApJ*, 395:675–681, August 1992.

[92] S. J. Schwartz and D. Burgess. Quasi-parallel shocks – A patchwork of three-dimensional structures. *Geophys. Res. Lett.*, 18:373–376, March 1991.

[93] R. Schwenn. *Large-Scale Structure of the Interplanetary Medium*, pages 99–181. Physics of the Inner Heliosphere I, 1990.

[94] R. Schwenn. Space Weather: The Solar Perspective. *Living Rev. Solar Phys.*, 3:2, August 2006.

[95] A. Shanmugaraju, Y.-J. Moon, M. Dryer, and S. Umapathy. Statistical Characteristics of CMEs and Flares Associated with Solar Type II Radio Bursts. *Sol. Phys.*, 217:301–317, November 2003.

[96] K. Shibata. Reconnection Models of Flares. In T. S. Bastian, N. Gopalswamy, and K. Shibasaki, editors, *Proc. Nobeyama Symp. (NRO Report No. 479)*, pages 381–389, December 1999.

[97] K. Shibata, Y. Ishido, L. W. Acton, K. T. Strong, T. Hirayama, Y. Uchida, A. H. McAllister, R. Matsumoto, S. Tsuneta, T. Shimizu, H. Hara, T. Sakurai, K. Ichimoto, Y. Nishino, and Y. Ogawara. Observations of X-ray jets with the YOHKOH Soft X-ray Telescope. *PASJ*, 44:L173–L179, October 1992.

[98] K. Shibata, N. Nitta, K. T. Strong, R. Matsumoto, T. Yokoyama, T. Hirayama, H. Hudson, and Y. Ogawara. A gigantic coronal jet ejected from a compact active region in a coronal hole. *ApJ*, 431:L51–L53, August 1994.

[99] K. Shibata, T. Yokoyama, and M. Shimojo. Coronal X-ray Jets. In *Proc. Kofu Symp.*, pages 75–78, July 1994.

[100] M. Shimojo. Studies of Solar Coronal X-ray Jets. *Ph.D. Thesis*, March 1999.

[101] M. Shimojo, S. Hashimoto, K. Shibata, T. Hirayama, H. S. Hudson, and L. W. Acton. Statistical Study of Solar X-Ray Jets Observed with the YOHKOH Soft X-Ray Telescope. *PASJ*, 48:123–136, February 1996.

[102] M. Shimojo and K. Shibata. Physical Parameters of Solar X-Ray Jets. *ApJ*, 542:1100–1108, October 2000.

[103] K. Stasiewicz. Theory and Observations of Slow-Mode Solitons in Space Plasmas. *Phys. Rev. Lett.*, 93(12):125004(1–4), September 2004.

[104] R. T. Stewart, R. A. Howard, F. Hansen, T. Gergely, and M. Kundu. Observations of Coronal Disturbances from 1 to 9 $R_{\rm sun}$. II: Second Event of 1973, January 11. *Sol. Phys.*, 36:219–231, 1974.

[105] R. T. Stewart, M. K. McCabe, M. J. Koomen, R. T. Hansen, and G. A. Dulk. Observations of Coronal Disturbances from 1 to 9 $R_{\rm sun}$. I: First Event of 1973, January 11. *Sol. Phys.*, 36:203–217, 1974.

[106] K. T. Strong, K. Harvey, T. Hirayama, N. Nitta, T. Shimizu, and S. Tsuneta. Observations of the variability of coronal bright points by the Soft X-ray Telescope on Yohkoh. *PASJ*, 44:L161–L166, October 1992.

[107] S. Suzuki and G. A. Dulk. *Bursts of Type III and Type V*, pages 289–332. Solar Radiophysics: Studies of Emission from the Sun at Metre Wavelengths, 1985.

[108] D. G. Swanson. *Plasma waves.* Academic Press, Inc. Boston, San Diego, New York, ISBN 0-12-678955-X, 1989.

[109] A. M. Title and C. J. Schrijver. The Sun's Magnetic Carpet. In R. A. Donahue and J. A. Bookbinder, editors, *ASP Conf. Ser. 154: Cool Stars, Stellar Systems, and the Sun*, pages 345–358, 1998.

[110] R. A. Treumann and W. Baumjohann. *Advanced space plasma physics.* London: Imperial College Press, 1997.

[111] S. Tsuneta and T. Naito. Fermi Acceleration at the Fast Shock in a Solar Flare and the Impulsive Loop-Top Hard X-Ray Source. *ApJ*, 495:L67–L70, March 1998.

[112] B. T. Tsurutani, A. L. Brinca, E. J. Smith, R. M. Thorne, F. L. Scarfe, J. T. Gosling, and F. M. Ipavich. Magnetohydrodynamic Waves Detected by Ice at Distances Equal-To 280,000,000-kilometers from Comet p/Halley – Cometary or Solar Wind Origin. *A&A*, 187:97–102, November 1987.

[113] B. T. Tsurutani, C. M. Ho, J. K. Arballo, B. E. Goldstein, and A. Balogh. Large amplitude IMF fluctuations in corotating interaction regions: Ulysses at midlatitudes. *Geophys. Res. Lett.*, 22:3397–3400, 1995.

[114] B. T. Tsurutani, E. J. Smith, R. M. Thorne, J. T. Gosling, and H. Matsumoto. Steepened magnetosonic waves at Comet Giacobini-Zinner. *J. Geophys. Res.*, 92:11074–11082, October 1987.

[115] Y. Uchida, M. D. Altschuler, and G. J. Newkirk. Flare-Produced Coronal MHD-Fast-Mode Wavefronts and Moreton's Wave Phenomenon. *Sol. Phys.*, 28:495–516, 1973.

[116] C. Vocks and G. Mann. Whistler wave excitation by relativistic electrons in coronal loops during solar flares. *A&A*, 452:331–337, June 2006.

[117] B. Vršnak. Solar flares and coronal shock waves. *J. Geophys. Res.*, 106:25291–25300, November 2001.

[118] B. Vršnak, V. Ruždjak, P. Zlobec, and H. Aurass. Ignition of MHD shocks associated with solar flares. *Sol. Phys.*, 158:331–351, May 1995.

[119] B. Vršnak, D. Sudar, and D. Ruždjak. The CME-flare relationship: Are there really two types of CMEs? *A&A*, 435:1149–1157, June 2005.

[120] A. Warmuth and G. Mann. The application of radio diagnostics to the study of the solar drivers of space weather. *Springer Lecture Notes in Physics*, 656:49–70, 2005.

[121] K.-P. Wenzel, R. G. Marsden, D. E. Page, and E. J. Smith. Ulysses: The first high-latitude heliospheric mission. *Adv. Space Res.*, 9:25–29, 1989.

[122] K. P. Wenzel, R. G. Marsden, D. E. Page, and E. J. Smith. The ULYSSES Mission. *A&AS*, 92:207–219, January 1992.

[123] J. P. Wild and L. L. McCready. Observations of the Spectrum of High-Intensity Solar Radiation at Metre Wavelengths. I. The Apparatus and Spectral Types of Solar Burst Observed. *Australian Journal of Scientific Research A Physical Sciences*, 3:387–398, September 1950.

[124] T. Yokoyama and K. Shibata. Numerical Simulation of Reconnection Between Emerging Flux and Coronal Field. In *Proc. Kofu Symp.*, pages 367–370, July 1994.

[125] T. Yokoyama and K. Shibata. Magnetic Reconnection as the Origin of X-Ray Jets and Hα Surges on the Sun. *Nature*, 375:42–44, May 1995.

[126] P. Zlobec, M. Messerotti, M. Karlicky, and H. Urbarz. Fine structures in time profiles of type II bursts at frequencies above 200 MHz. *Sol. Phys.*, 144:373–384, April 1993.

Index

List of Figures

List of Tables

Acknowledgments

I acknowledge the whole Solar Radio Group at the Astrophysical Institute Potsdam (AIP), for the good working atmosphere during my time there.

For the financial aspect of my stay in Germany, I appreciate the 32-month scholarship from DAAD (Deutscher Akademisher Austausch Dienst) Ref: A/03/10336, the 3-month internal grant from AIP, and the 7-month support from a DLR (Deutsches Zentrum für Luft- und Raumfahrt) project No. 50 QL 0001.

To the secretary of the group, Mrs. Doris Lehmann, I'm obliged for her assistance at the administrative part of my research stay at AIP.

To all my colleagues in the Solar Radio Group of the AIP, I am thankful for their aid in different aspects during my research work and especially:
to Dipl.-Phys. Germar Rausche for introducing the *Mathematica* software package to me;
to Dipl.-Phys. Hakan Önel, for his help while working with the *Mathematica* software package and for his assistance during my one-semester teaching at the Potsdam University;
to Dr. Alexander Warmuth for pointing out some useful radio results to me;
to Dr. Christian Vocks for adapting his numerical code to the need of my research interest;
and to Dr. Henry Aurass for introducing the radio data process to me.

To my supervisor Prof. Dr. Gottfried Mann, I express my deepest appreciation for his kind and attentive guidance during my Ph.D. time in the Solar Radio Group. I am much beholden to his great support and endless patience throughout my research stay at AIP.

I am grateful to Jasmina Magdalenić and Gabriela Marcano for their precious friendship.

Finally, I dedicate this work to my family: my parents, my sister Janeta and my niece Elena, who will be always the light of my life. Even in my darkest times and far away, my heart will be always by them.

March, 2007

Rossitsa Miteva